Silesian University in Opava
Faculty of Philosophy and Science
Department of Physics

Optical phenomena in curved spacetimes

Thesis submitted for the degree of Doctor Philosophiae

Jan Schee

Supervisor: prof. RNDr. Zdeněk Stuchlík CSc.

Opava, February 2009

Referees:

doc. RNDr. Vladimír Karas, DrSc.
Astronomical Institute, Academy of Sciences,
Prague,
Czech Republic

doc. RNDr. Oldřich Semerák, PhD.
Institute of Theoretical Physics, Charles University,
Prague,
Czech Republic

Acknowledgements

At first I'd like to thank my supervisor, professor Zdeněk Stuchlík, for his helpfull advice, comments and useful ideas on this thesis and my research work. I also wish to thank my wife Kateřina and my daughter Magdaléna for their patience and support during my PhD studies. My thanks also belong to my parents who have always supported me in all my studies.

Contents

Introduction

The Electromagnetic Radiation (photon) - so far the only witness of the events taking place in deep universe. Delivering information about spacetime fabric it passes throught. Without understanding how a particular spacetime geometry influences the basic properties of radiation (frequency, polarisation, flux) the information it caries cannot be succesfully decoded.

Albert Einstein, in 1916, published his great discovery - The General relativity. For almost hundred years it plays important role in the study of strong gravitational phenomena in the universe. The Einstein's field equations

$$G_{\mu\nu} = \frac{8\pi\kappa}{c^4} T_{\mu\nu} + \Lambda g_{\mu\nu} \tag{1}$$

tell us how matter distribution $T_{\mu\nu}$ and energy of vacuum Λ warp the spacetime geometry encoded into Einstein's gravitational tensor $G_{\mu\nu}$. Many solutions have been found of those equations. Among the first of them the Schwarzchild geometry describing spherically symmetric and static spacetime. It showed up that this solution describes static spherically symmetric black-hole and soon the geometry of charged static black hole was found indepedently by Reissner and Nordström. Almost fifty years later the exact solution of stationary axially symmetric spacetime was found by Roy Kerr. This solution describes the geometry of rotating black hole. A few years later Newman found the metric of charged rotating black hole. When Einstein's equations (1) are applied to The Universe as a whole one recovers Friedman equations which tell us that the universe is expanding. The photon travelling through such spacetime suffers from cosmological redshift due to the expansion. The universe is not perfectly homogenous and isotropic. This feature is imprinted in temperature fluctuations of cosmic microwave background radiation (CMBR). There are many effects that influence these fluctuations such as Sunyaev-Zeldovich effect (scattering of CMB photons on charged particles), Sachs-Wolfe effect (additional redshift(blueshift) due to passage of CMB photon through local potentional well at the last scattering surface), Rees-Sciama effect (additional frequency shift due to vakuola inhomogenity at redshifts $z \lesssim 10$). The last mentioned effect will be discussed in details in Application section of this thesis.

General relativity is a very strong tool which is used to understand the structure of the universe and the events in the vicinity of black hole horizons, but this theory fails in the regimes of super strong gravity on Planck scale $l_{pl} \sim 10^{-35}$ m. There are now several attempts that seem to lead to theory which works on scales of Planck lenght and which contain, as weak field approximation, Einstein's general relativity - The String Theories. It

is a multidimensional theory with one temporal dimension and nine spatial dimensions (or ten dimensions in M-theory). Three of them are our familiar width, height and depth and the remaining six (seven) are curled into orbitfolds of size less than scale of nucleus. Recently, another approach of dealing with additional dimensions was discovered - The Randall - Sundrum braneworld scenario. In this model all matter fields are restricted on the three dimensional space called brane while gravitation can propagate in additional dimension which need not be curled into finite dimension but can have infinite scale. On the brane, matter can collapse and form a black hole, static or rotating. It was shown that the induced metric on the brane has, in static spherically symmetric case, the form of Reissner - Nordström metric or in the stationary axially symmetric case the form of the Kerr-Newman geometry. In both cases the square of electric charge e^2 is replaced by a braneworld parameter called *tidal charge* delivering information about the effect of bulk gravity on the brane.

The motion of the test particles and photons (or fluids) in 4D black-hole spacetimes on the brane can thus be given in a simple form using the standard black-hole solutions with an additional tidal charge parameter replacing the squared charge parameter; however, negative values of the tidal charge are possible and more realistic, leading to some new, unusual, phenomena. The study of motion of photons in such spacetime is presented in the application section of this thesis.

The presented thesis is devoted to some studies of the optical phenomena in curved spacetimes and is concentrated in discussions of the influence of the two most interesting new phenomena of recent cosmology, namely, *the tidal charge* in the optical effects in strong gravitational field near black hole horizon and *the cosmological constant* in the Rees-Sciama effect on the CMBR. In all these studies, the optical effects are given by the geodesic motion of photons.

The thesis is organised in the following way. In Part I - Preliminaries, equations of the (geodetical) motion are given in the relevant spacetimes (SdS, Friedman Universe, Einstein-Strauss-de Sitter vakuola model, and in Kerr-Newman spacetimes that could be used to describe braneworld rotating black holes) and then the basical optical effects are briefly summarized.

In Part II - Applications, we present in Chapter 2 a detailed discussion of the braneworld Kerr black holes and the related optical phenomena, namely escape cones structure, silhuette of the black hole, accretion disc images and profilled lines of radiating rings. In Chapter 3 we present discussion of the influence of the relict cosmological constant, indicated by a large variety of cosmological tests, on the temperature fluctuations of the CMBR due to the large galaxies (or their cluster) represented by the standard vakuola model.

Part I

Preliminaries

Chapter 1

Equations of motion and optical effects

1.1 Geodesic equations

The equations of motion of test particles (photons) in Schwarzchild-de Sitter spacetime and in Friedman expanding spacetime are discussed in the framework of classical Einstein theory. The results are then used in discussion of the influence of the positive cosmological constant Λ on the Rees-Sciama effect in Chapter 3. Further we give the equations of motion of test particles (photons) in the Kerr-Newman spacetime that can be used to describe the spacetime of a rotating black hole formed on the 3-brane in the framework of the braneworld scenario. The results are then used in Chapter 2 to discuss the influence of *tidal charge* b which carries the information of bulk effects on the brane.

The geodesic equation takes the form

$$\frac{\mathrm{D}k^{\mu}}{\mathrm{d}w} = \frac{\mathrm{d}k^{\mu}}{\mathrm{d}w} + \Gamma^{\mu}{}_{\alpha\beta} k^{\alpha} k^{\beta} = 0 \tag{1.1}$$

with the normalization condition

$$g_{\mu\nu} k^{\mu} k^{\nu} = -m^2 \tag{1.2}$$

where k^{μ} is 4-momentum of a particle (photon), w is affine parameter of the geodesic, $\Gamma^{\mu}{}_{\alpha\beta}$ are componets of the affine connection, and m is the rest energy of the particle. For photons $m = 0$.

The equations of motion in the particular spacetimes of interest are presented in the following subsections.

1.1.1 Schwarzchild - de Sitter geometry

The Schwarzchild - de Sitter geometry is static and spherically symmetric solution of Einstein equations (1) with zero momentumm energy tenzor $T_{\mu\nu}$ and positive cosmological constant Λ. The line element in Schwarzchild coordinates (t, r, θ, φ) has form

$$\mathrm{d}s^2 = -\mathcal{A}^2(r)\mathrm{d}t^2 + \mathcal{A}^{-2}(r)\mathrm{d}r^2 + r^2(\mathrm{d}\theta^2 + \sin^2\theta\mathrm{d}\varphi^2) \tag{1.3}$$

where is

$$\mathcal{A}^2(r) = 1 - \frac{2M}{r} - \frac{\Lambda}{3}r^2. \tag{1.4}$$

By introducing transformations $r/M \to r$ and $\Lambda M^2/3 = y$ we rewrite the metric function (1.4) to form

$$\mathcal{A}^2(r) = 1 - \frac{2}{r} - yr^2. \tag{1.5}$$

The loci of horizons of Schwarzchild-de Sitter geometry are at radii which satisfy equation $A(r)^2 = 0$. For $y < 1/27$ there are two horizons, the black hole horizon given by formula

$$r_h = \frac{2}{\sqrt{3y}}\cos\frac{\pi + \alpha}{3} \tag{1.6}$$

and cosmological horizon at

$$r_c = \frac{2}{\sqrt{3y}}\cos\frac{\pi - \alpha}{3} \tag{1.7}$$

where

$$\alpha = \cos^{-1}(\sqrt{27y}). \tag{1.8}$$

In case of $y = 0$ there is only one horizon at $r = 3M$ and in case of $y > 1/27$ there are no horizons.

The geometry represented here by line element (1.3) does not depend on time coordinate t and azimuthal coordinate φ. This imply that there exist two killing vector fields; the timelike killing field $\xi^\mu = \delta^\mu{}_t$ and the spacelike killing field $\zeta^\mu = \delta^\mu{}_\varphi$. Two constants of motion are tightly connected with those killing fields. They are energy E of test particle relative to distant observer given by expression

$$p_\mu\xi^\mu = p_t \equiv -E \tag{1.9}$$

and the azimuthal angular momentum L_z relative to distant observer given by formula

$$p_\mu \zeta^\mu = p_\varphi \equiv L_z. \tag{1.10}$$

From Lagrangian of freely falling particle

$$\mathcal{L} = \frac{1}{2} g_{\mu\nu} \frac{\mathrm{d}x^\mu}{\mathrm{d}w} \frac{\mathrm{d}x^\nu}{\mathrm{d}w} \tag{1.11}$$

together with constants of motion (1.9) and (1.10) one arrives to equations of motion of test particle, which read

$$p^t = \frac{\mathrm{d}t}{\mathrm{d}w} = E\mathcal{A}^{-2}(r), \tag{1.12}$$

$$p^r = \frac{\mathrm{d}r}{\mathrm{d}w} = \pm \left(E^2 - V_{\mathrm{eff}}^2\right)^{1/2}, \tag{1.13}$$

$$p^\theta = \frac{\mathrm{d}\theta}{\mathrm{d}w} = \pm \frac{1}{r^2} \left(L^2 - \frac{L_z}{\sin^2\theta}\right)^{1/2}, \tag{1.14}$$

$$p^\varphi = \frac{\mathrm{d}\varphi}{\mathrm{d}w} = \frac{L_z}{r^2 \sin^2\theta}, \tag{1.15}$$

where is

$$V_{\mathrm{eff}}^2 = \mathcal{A}^2(r) \left(m^2 + \frac{L^2}{r^2}\right) \tag{1.16}$$

the effective potential and L is the third constant of motion the total angular momentum. In case of null geodesics there is $m = 0$. There exist the third importan radius in Schwarzchild-de Sitter spacetime, it is *static radius* r_s. It follows from the requirement that $L = 0$ and $\partial V_{\mathrm{eff}}^2 = 0$. Its value then reads

$$r_s = \left(\frac{\Lambda}{3M^2}\right)^{-1/3}. \tag{1.17}$$

At this radius the effect of cosmological repulsion, determined by positive cosmological constant Λ, is balanced by gravity.

From the central symmetry of the geometry (1.3) it follows that the motion of test particles is restricted to central plane. Therefore the effective potential (1.16) can be written as

$$V_{\mathrm{eff}}^2 = \mathcal{A}^2(r) \left(m^2 + \frac{L_z^2}{r^2}\right). \tag{1.18}$$

The motion of test particles is now fully determined by the behaviour of the effective potential (1.18) and equation (1.13) with this effective potential.

In case of photons we see from (1.13) that the affine parameter w can be rescaled to affine parameter $w' = Ew$. By introducing the *impact parameter* b by relation

$$b = \frac{L_z}{E}, \tag{1.19}$$

the equation (1.13) read

$$(p^r)^2 = 1 - \mathcal{A}^2(r)\frac{b^2}{r^2}. \tag{1.20}$$

From the reality condition $\left(\frac{\mathrm{d}r}{\mathrm{d}w'}\right)^2 \geq 0$ we see that the photon motion is possible only in the regions where $V_{\mathrm{eff}} \leq 1$. There is the critical value of impact parameter $b = b_{\mathrm{crit}}$ which separates photon geodesics with one turning point $b < b_{\mathrm{crit}}$ from those without a turning point $b > b_{\mathrm{crit}}$. Its value comes from conditions $\partial V_{\mathrm{eff}}^2/\partial r = 0$ and $p^r = 0$ and reads

$$b_{\mathrm{crit}} = \sqrt{\frac{27}{1-27y}}. \tag{1.21}$$

The test particle motion has been studied in series of papers [8, 10, 11, 12], while the photon motion is discussed in [13, 76, 16, 78].

1.1.2 Friedman cosmological spacetimes

The homogenity and isotropy of spacetime at every point lead to Robertson - Walker geometry which, in form of line element, reads

$$\mathrm{d}s^2 = -\mathrm{d}T^2 + R^2(T)\left[\mathrm{d}\chi^2 + \Sigma_k^2(\chi)(\mathrm{d}\theta^2 + \sin^2\theta\mathrm{d}\varphi^2)\right]. \tag{1.22}$$

T is the time coordinate as measured on the clock of comoving observer, $R(T)$ is the expansion parameter which is the function of time T only, and

$$\Sigma_k = \begin{cases} \sin\chi & \text{for} \quad k = +1 \\ \chi & \text{for} \quad k = 0 \\ \sinh\chi & \text{for} \quad k = -1 \end{cases} \tag{1.23}$$

Metric represented by line element (1.22) does not depend only on azimuthal coordinate φ, therefore there is only one motion constant, the azimuthal angular momentum $L_z = p_\varphi$. Equations of motion of a test particle then read

$$p^T = \frac{\mathrm{d}T}{\mathrm{d}w} = \left(m^2 + \frac{p^2}{R^2}\right)^{1/2}, \tag{1.24}$$

$$p^\chi = \frac{\mathrm{d}\chi}{\mathrm{d}w} = \pm\frac{1}{R^2}\left(p^2 + \frac{L^2}{\Sigma_k^2}\right)^{1/2}, \tag{1.25}$$

$$p^\theta = \frac{\mathrm{d}\theta}{\mathrm{d}w} \pm \frac{1}{R^2\Sigma_k^2}\left(L^2 - \frac{L_z^2}{\sin^2\theta}\right)^{1/2}, \tag{1.26}$$

$$p^\varphi = \frac{\mathrm{d}\varphi}{\mathrm{d}w} = \frac{L_z}{R^2\Sigma_k^2\sin^2\theta}. \tag{1.27}$$

where three motion constants are given by relations

$$L_z = p_\varphi, \tag{1.28}$$

$$L^2 = p_\theta^2 + p_\varphi^2\sin^{-2}\theta, \tag{1.29}$$

$$p^2 = p_\chi^2 + L^2\Sigma_k^{-2} \tag{1.30}$$

where $L_z(L)$ represent azimuthal(total) angular momentum.

1.1.3 Einstein–Strauss–de Sitter vakuola model

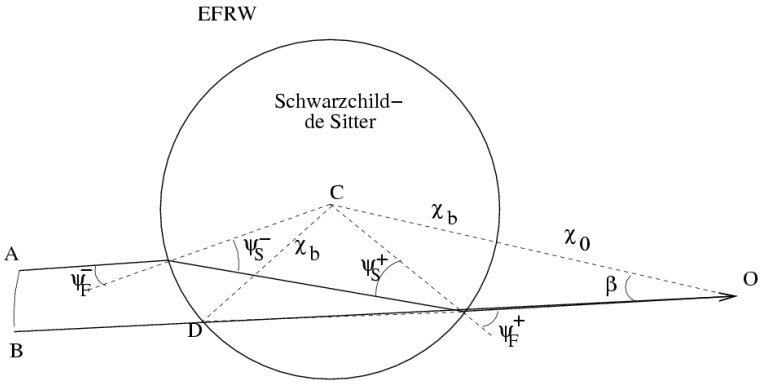

Figure 1.1: ESdS vakuola model. A schematic picture of a cluster represented as a sphericaly symmetric inhomogeneity immersed in the dust filled Friedman universe. The observer O receives two photons coming through the vakuola, and third one coming directly.

In the construction of the ESdS model with a $\Lambda > 0$, we remove a spherical ball of dust of the mass M from the dust-filled universe and replace it

by the Schwarzschild–de Sitter spacetime of the same mass M. Its expanding boundary surface coincides at a fixed value of the comoving Robertson-Walker (RW) coordinate $\chi_E = \chi_{\rm b}$ with expanding surface $\chi = \chi_{\rm b} = {\rm const}$ of the Friedman universe (see Fig.1.1). The Schwarzschild–de Sitter (SdS) spacetime can be completely vacuum, i.e., a black-hole spacetime or it has a spherical source represented by a part of an internal dusty Friedman universe with parameters different than those of the external Friedman universe outside of the vacuum SdS spacetime, and characterized by $\chi_I < \chi_E$. For simplicity, we shall not consider influence of the source of the internal part of the ESdS vakuola model on the CMBR fluctuations.

In the standard Schwarzschild coordinates, the vacuum SdS spacetime of mass M is described by the line element (1.3) and the Friedman universe is described by the FRW geometry which in the comoving coordinates is given by equation (1.22).

The RW metric describes the external Friedman universe at $\chi \geq \chi_E = \chi_{\rm b}$, while at $\chi < \chi_{\rm b}$ it is replaced by the expanding part of the SdS spacetime. The particles with $\chi = \chi_{\rm b}$ follow radial geodesics of the SdS spacetime.

The evolution of the Friedman universe is given by the evolution of the scale factor R and the energy density ρ in dependence on the cosmic time T. The scale factor fulfils the Friedman equation

$$\left(\frac{{\rm d}R}{{\rm d}T}\right)^2 = \frac{8\pi\rho}{3R} + \frac{\Lambda}{3}R^2 - k \tag{1.31}$$

and the energy density ρ satisfies the energy conservation equation in the form

$$\frac{8\pi\rho}{3}R^3 = {\rm const} = R_0. \tag{1.32}$$

In order to match the matching hypersurface on the Friedman side and the Schwarzschild-de Sitter side it is necessary to synchronize the proper time of a dust particle on the matching hypersurface (MH hereinafter) $\chi = \chi_{\rm b}$ as measured from the both sides of the MH. Therefore, the proper time τ of a test particle following the radial geodesic, as measured in the SdS spacetime, must be equal to the cosmic time T, as measured in the FRW spacetime. The junction conditions have the following form [8]

$$r_{\rm b} = R(T)\,\Sigma_k(\chi_{\rm b}), \quad \tilde{R} = R_0\Sigma_k(\chi_{\rm b}), \quad \tilde{R}\sqrt{\tilde{R}/2M} = R_0, \tag{1.33}$$

where the parameter $\tilde{R}$ is related to the covariant energy $\mathcal{E}_{\rm b}$ of the test particles along the radial geodesic, representing the MH, by the relation

$$\mathcal{E}_{\rm b} = \sqrt{1 - \frac{2kM}{\tilde{R}}}. \tag{1.34}$$

The internal 3-geometry of the MH as measured from the FRW universe side is given by the line element

$$\mathrm{d}s_+^2 = -\mathrm{d}T^2 + R^2(T)\,\Sigma_k^2(\chi_\mathrm{b})\left(\mathrm{d}\theta^2 + \sin^2\theta\,\mathrm{d}\phi^2\right). \tag{1.35}$$

From the side of the SdS spacetime it is given by the line element

$$\mathrm{d}s_-^2 = -\mathrm{d}T^2 + r_\mathrm{b}^2(T)\left(\mathrm{d}\theta^2 + \sin^2\theta\,\mathrm{d}\phi^2\right). \tag{1.36}$$

Both geometries are identical due to the junction conditions. To show that the construction of the Einstein–Strauss–de Sitter model is correct one has to check whether the Einstein's equations are satisfied at the matching hypersurface [9].

1.1.4 Kerr-Newman geometry

The geometry generated by rotating black hole (naked singularity) with electric charge e is the Kerr-Newman geometry. The line element of this geometry in Boyer-Linquist coordinates read

$$\begin{aligned}\mathrm{d}s^2 &= -\left(1-\frac{2Mr-e^2}{\Sigma}\right)\mathrm{d}t^2 + \frac{\Sigma}{\Delta}\mathrm{d}r^2 + \Sigma\mathrm{d}\theta^2 + \frac{A}{\Sigma}\mathrm{d}\varphi^2 \\ &\quad -2\frac{2Mr-e^2}{\Sigma}\sin^2\theta\mathrm{d}t\mathrm{d}\varphi,\end{aligned} \tag{1.37}$$

where

$$\Sigma = r^2 + a^2\cos^2\theta, \tag{1.38}$$
$$\Delta = r^2 - 2Mr + a^2 + e^2, \tag{1.39}$$
$$A = (r^2+a^2)^2 - a^2\Delta\sin^2\theta. \tag{1.40}$$

M is the mass parameter, $a = J/M$ is the specific angular momentum and e^2 is the square if electric charge parameter.

In order to study the optical effects in Kerr-Newman spacetime, we have to solve equations of motion of photons. In 1968 Brandon Carter derived, using Hamilton-Jacobi formalism, differential equations of motion of test particles in Kerr-Newman spacetime in terms of the first integrals.

The componets of metric tensor given by (1.37) do not depend on φ and t coordinates and therefore the conjugate momenta

$$k_\varphi = g_{\varphi\nu}k^\nu \equiv \Phi, \tag{1.41}$$
$$k_t = g_{t\nu}k^\nu \equiv -E, \tag{1.42}$$

are the integrals of motion. Brandon Carter found another integral of motion K as a separation constant when solving Hamilton-Jacobi equation

$$g^{\mu\nu}\frac{\partial S}{\partial x^\mu}\frac{\partial S}{\partial x^\nu} = 0, \tag{1.43}$$

where he assumed the action S in separated form

$$S = -Et + \Phi\varphi + S_r(r) + S_\theta(\theta). \tag{1.44}$$

The equations of motion can be integrated and written separatelly in the form

$$\Sigma\frac{\mathrm{d}r}{\mathrm{d}w} = \pm\sqrt{R(r)}, \tag{1.45}$$
$$\Sigma\frac{\mathrm{d}\theta}{\mathrm{d}w} = \pm\sqrt{W(\theta)}, \tag{1.46}$$
$$\Sigma\frac{\mathrm{d}\varphi}{\mathrm{d}w} = -\frac{P_W}{\sin^2\theta} + \frac{aP_R}{\Delta}, \tag{1.47}$$
$$\Sigma\frac{\mathrm{d}t}{\mathrm{d}w} = -aP_W + \frac{(r^2+a^2)P_R}{\Delta}, \tag{1.48}$$

where

$$R(r) = P_R^2 - \Delta K, \tag{1.49}$$
$$W(\theta) = K - \left(\frac{P_w}{\sin\theta}\right)^2, \tag{1.50}$$
$$P_R(r) = E(r^2+a^2) - a\Phi, \tag{1.51}$$
$$P_W(\theta) = aE\sin^2\theta - \Phi. \tag{1.52}$$

It is usefull to introduce integral of motion Q by the formula

$$Q = K - (E - a\phi)^2. \tag{1.53}$$

Its relevance comes from the fact that in the case of astrophysically most important motion in the equatorial plane ($\Theta = \pi/2$) there is $Q = 0$.

1.2 Optical Effects

We breefly present definitions of four optical phenomena astrophysically important in the study of the influence of spacetime geometry on radiation passing through it. They are frequency shift of the photon, focusing of the photon beam and silhuette of the black hole.

1.2.1 Escape cones

The optical phenomena related to accretion processes in the field of rotating black holes could be efficiently studied by using the notion of light escape cones of local observers (sources) that determine which portion of radiation emitted by a source could escape to infinity and, complementary, which portion is trapped by the black hole [52].

1.2.2 Frequency shift of a photon

The frequency shift g can be expressed as the ratio of observed photon energy E_o to emitted photon energy E_e that yields

$$g = \frac{E_o}{E_e} = \frac{(k_o)_\mu u_o^\mu}{(k_e)_\mu u_e^\mu}, \tag{1.54}$$

where $(k_o)_\mu((k_e)_\mu)$ are covariant components of photon 4-momentum taken at the event of observation (emission) and u_o^μ (u_e^μ) are contravariant components of the 4-velocity of the observer (emitter). The particular form of frequency shift g depends, of course, on the 4-velocity of observer (emitter) in spacetime of interest.

1.2.3 Focusing of the photon beam

In particular there are two ways of dealing with focusing of the photon beams. The first method is based on simultaneous solution of geodesic equation and geodesic deviation equation. Two initially orthonormal 4-vectors Y_1^μ and Y_2^μ are paralelly transported along geodesic from an observer at infinity to the point of emission. The ratio of proper area of the light tube at infinity to the area given by transported 4-vectors at point of emission give us the focusing of the photon beam. This method is very important in situations when photon beam passes through the material with nonzero opacity. In the application presented in this thesis the second method based on calculation of solid angle which the element of radiating surface subtends in the frame of distant observer is used. Let an observer be located at the distance d_0 from

the source. The solid angle $\mathrm{d}\Pi$ can be expressed in terms of observer's plane coordinates $[\bar{\alpha}, \bar{\beta}]$

$$\mathrm{d}\Pi = \frac{1}{d_o^2}\mathrm{d}\bar{\alpha}\mathrm{d}\bar{\beta}. \tag{1.55}$$

In particular spacetime, the coordinates $[\bar{\alpha}, \bar{\beta}]$ are functions of impact parameters λ and q. The solid angle element then reads

$$\mathrm{d}\Pi = \frac{1}{d_o^2}\left|\frac{\partial(\bar{\alpha}, \bar{\beta})}{\partial(\lambda, q)}\right|\mathrm{d}\lambda\mathrm{d}q.. \tag{1.56}$$

This enables computing of light curves and profiled spectral lines.

1.2.4 Silhuette of a black hole on bright background

In principle, it is of astrophysical importance to consider a black hole in front of a source of illumination whose angular size is large compared with the angular size of the black hole [22]. A distant observer will see a silhuette of the black hole, i.e., a black hole in the larger bright source. The rim of the black hole silhuette corresponds to photon trajectories spiralling around the black hole many times before they reach the observer. Of course, the shape of the silhuette enables, in principle, determination of the black hole parameters. But we have to be aware of the strong dependency of the silhuette shape on the observer viewing angle; clearly, the shape will be circular for observers on the black hole rotation axis, and its deformation grows with observer approaching the equatorial plane.

The silhuette can be treated as the complement of the light escape cone as shown later.

Part II

Applications

Chapter 2

Braneworld Kerr black holes

String theory and M-theory describing gravity as a truly higher-dimensional interaction becoming effectively 4D at low-enough energies inspired studies of the braneworld models, where the observable universe is a 3-brane (domain wall) to which the standard model (non-gravitational) matter fields are confined, while gravity field enters the extra spatial dimensions the size of which may be much larger than the Planck length scale $l_{\rm P} \sim 10^{-33}\,{\rm cm}$ [18]. Gravity can be localized near the brane at low energies even with a non-compact, infinite size extra dimension with the warped spacetime satisfying the 5D Einstein equations with negative cosmological constant [47].

Significant deviations from the Einstein gravity occur at very high energies in vicinity of compact objects (see e.g., [42, 34, 17]). The high-energy effects produced by the gravitational collapse are disconnected from the outside space by the horizon, but they could have a signature on the brane, influencing properties of black holes [42]. There are high-energy effects of local character influencing pressure in collapsing matter The non-local corrections of "back-reaction" character arise from the influence of the Weyl curvature of the bulk space on the brane - the matter on the brane induces Weyl curvature in the bulk which makes influence on the structures on the brane due to the bulk gravitation stresses [42, 28]. The combination of high-energy (local) and bulk stress (non-local) effects alters significantly the matching problem on the brane, as compared to the 4D Einstein gravity; for spherical objects, matching no longer leads to a Schwarzchild exterior in general [28, 34]. The Weyl stresses induced by bulk gravitons imply that the matching conditions do not have unique solution on the brane; in fact, knowledge of the 5D Weyl tensor is needed as a minimum condition for uniqueness [34]. However, recently no exact 5D solution is known. Assuming spherically symmetric metric induced on the 3-brane the effective gravitational fied equations of vacuum type in both the brane and bulk can be solved, giving a Reissner-Nordström

static black hole solutions endowed with a "tidal" charge parameter b [28], instead of the standard electric charge parameter e^2 [45]. The tidal charge reflects the effects of the Weyl curvature of the bulk space, i.e., from the 5D gravitation stresses [28, 42] with bulk gravitation tidal effects giving the name of the charge. Note that the tidal charge can be both positive and negative, and there are some indications that the negative tidal charge should properly represent the "back-reaction" effects of the bulk space Weyl tensor on the [42, 28, 66]

The stationary and axisymmetric solution of the constrained equations describing rotating black holes localized in the Randall-Sundrum braneworld were derived in [17]. The solutions are determined by metric tensor of the Kerr-Newman form with a tidal charge describing the 5D correction term generated by the 5D Weyl tensor stresses. The tidal charge has an "electric" character and arises due to the 5D gravitational coupling between the brane and the bulk, reflected on the brane through the "electric" part of the bulk Weyl tensor [17], in analogy with the spherically symmetric black-hole case [28]. When the electromagnetic field is introduced, the non-vacuum solutions of the effective Einstein equations on the brane are much more complex in comparison with the standard Kerr-Newman solutions [17].

Here we consider optical phenomena in the Kerr-Newman type of solutions describing the brany rotating (Kerr) black holes with no electric charge, since in astrophysically relevant situations the electric charge of the black hole must be exactly zero, or very small [45]. Then the results obtained in analysing the behaviour of test particles and photons or test fields around the Kerr-Newman black holes could be used assuming both positive and negative values of the brany tidal parameter b (used instead of the charge parameter e^2).

The information on the properties of strong gravitational fields in vicinity of compact objects, namely of black holes, is encoded into optical phenomena of different kind that enable us to make estimates of the black hole parameters, including its tidal charge, when predictions of the theoretical models are confronted with the observed data. From this point of view, the spectral profiles of accretion discs around the black holes in galactic binaries, e.g., in microquasars, are most promising [44], along with profiled spectral lines in the X-ray flux [21, 57, 41, 43, 67, 48, 33, 65, 68, 69]. Important information could also be obtained from the quasiperiodic oscillations observed in the X-ray flux of some low-mass black hole binaries of Galactic origin [70, 50], some expected intermediate black hole sources [71], or those observed in Galactic nuclei [19, 20]. The most promising orbital resonance model then enables relative exact measurement of the black hole parameters [63, 61, 62] that should be confronted with the predictions of the optical modelling [44]. In the case

of our Galaxy centre black hole Sgr A*, we could be able to measure the detailed optical phenomena, as compared with the other sources, since it is the nearest supermassive black hole with mass estimated to be $\sim 4\times 10^6 M_\odot$ [72], enabling us to measure the "silhuette" of the black hole and other subtle GR phenomena in both weak and strong field limits [26, 73, 52].

We present an introductory study on the role of the brany tidal charge parameter in the optical phenomena related to profiled spectral lines generated by thin radiating tori in the brany Kerr black-hole backgrounds. Of course, for $b > 0$, the results hold as well for standard Kerr-Newman spacetimes due to the correspondence $b \to e^2$ with e^2 being the squared charge parameter of the Kerr-Newman black hole. We use here the transfer function method [21] which seems to be the most appropriate in our problem. The line profiles are determined in dependence on the viewing angle θ_0 and the ring radius r_e, which is assumed to be located in the inner part of a thin accretion disc. Specially, it is assumed near marginally stable orbit r_{ms} and in the orbit corresponding to the resonance radius $r_{3:2}$ where the ratio of vertical and radial epicyclic frequencies is $\sim 3/2$, corresponding to the QPOs frequency ratios commonly observed in microquasars [63, 62].

2.1 The effective gravitational equations

The 5D Einstein equations in the bulk spacetime have the form [53, 28]

$$\begin{aligned} {}^{(5)}G_{AB} &= {}^{(5)}R_{AB} - \frac{1}{2} g_{AB}\ {}^{(5)}R \\ &= -\Lambda_5 g_{AB} + \kappa_5^2 \left({}^{(5)}T_{AB} + \sqrt{\frac{h}{g}}\tau_{AB}\delta Z \right), \end{aligned} \tag{2.1}$$

where $\kappa_5^2 = 8\pi G_5$ (G_5 being the bulk gravitational constant), Λ_5 is the bulk cosmological constant (assuming anti-de Sitter geometry), ${}^{(5)}T_{AB}$ is the energy-momentum tensor in the bulk, $\tau_{AB}$is the energy-momentum tensor on the brane, h and g being metric determinants of $h_{\alpha\beta}$ and g_{AB}, and the bulk spacetime is expressed in the form

$$g_{AB} = n_A n_B + h_{\alpha\beta} e^\alpha_A e^\beta_B. \tag{2.2}$$

Here, n_A is the unit vector orthogonal to the brane and e^α_A represents local frame of four-vectors; the induced metric on the brane

$$h_{\alpha\beta} = g_{AB} e^A_\alpha e^B_\beta. \tag{2.3}$$

The effective Einstein gravitational equations (EGE) on the brane could then be given by using the Israel junction method generalized to 5D situation. The gravitational field equations on the brane take the form [53]

$$G_{\alpha\beta} = -\Lambda h_{\alpha\beta}\kappa_4^2 T_{\alpha\beta} + \kappa_5^4 S_{\alpha\beta} - W_{\alpha\beta} - 3\kappa_5^2 U_{\alpha\beta}. \tag{2.4}$$

The traceless tensor

$$W_{\alpha\beta} = A_{\alpha\beta} - \frac{1}{4}h_{\alpha\beta}A \tag{2.5}$$

is constructed from the "electric" part of the bulk Riemann tensor

$$A_{\alpha\beta} = {}^{(5)}R_{ABCD}n^A n^C e^B_\alpha e^D_\beta, \quad A = h_{\alpha\beta}A^{\alpha\beta}. \tag{2.6}$$

The cosmological constant on the brane

$$\Lambda = \frac{1}{2}\left(\Lambda_5 + \frac{1}{6}\kappa_5^4\lambda^2 - \kappa_5^2 P\right), \tag{2.7}$$

where

$$P = {}^{(5)}T_{AB}n^A n^B \tag{2.8}$$

is the normal compressive pressure term in the 5D spacetime, and 4D gravitational constant is related to the brane tension λ by the relation

$$\kappa_4^2 = \frac{1}{6}\kappa_5^4\lambda. \tag{2.9}$$

The "squared energy-momentum" tensor is given by

$$S_{\alpha\beta} = -\frac{1}{4}\left[\left(T^\gamma_\alpha T_{\gamma\beta} - \frac{1}{3}TT_{\alpha\beta}\right) - \frac{1}{2}h_{\alpha\beta}\left(T_{\gamma\delta}T^{\gamma\delta} - \frac{1}{3}T^2\right)\right], \tag{2.10}$$

while the traceless brany part of the bulk energy-momentum tensor is

$$U_{\alpha\beta} = -\frac{1}{3}\left({}^{(5)}T_{\alpha\beta} - \frac{1}{4}h_{\alpha\beta}h^{\gamma\delta}\ {}^{(5)}T_{\gamma\delta}\right). \tag{2.11}$$

In the effective 4D EGE (2.4)-(2.11), $W_{\alpha\beta}$ describes non-local gravitational effects of the bulk space onto the brane and is sometimes called Weyl fluid, while the local bulk effects on the brane are given by $S_{\alpha\beta}$, $U_{\alpha\beta}$ and P.

It should be stressed that the self-consistent solutions of the effective 4D EGE (2.4)-(2.11) on the brane require the knowledge of the non-local gravitational and energy-momentum terms coming from the bulk spacetime. Therefore, the brany field equations are not closed in general and evolution

equations into the bulk have to be solved for the projected bulk curvature and energy-momentum tensors. However, in particular cases the brany-equations system could be made closed assuming a special ansatz for the induced metric. In this way, both spherically symmetric [28] and axially symmetric brany black hole spacetimes [17] have been found. Assuming vacuum bulk and brany spacetimes, the non-local gravitational effects of the bulk could be simply represented by the so called tidal charge entering the standard metric of the black hole spacetimes.

The rotating black holes localised on a 3-brane in the Randall-Sundrum braneworld model were derived under the assumption of stationary and axisymmetric Kerr-Schild metric on the brane and supposing empty bulk space and no matter fields on the brane ($T_{\alpha\beta} = 0$) [17]. The specialized solution of the constrained equations is thus assumed in the form

$$\mathrm{d}s^2 = \eta_{\mu\nu}\mathrm{d}x^\mu \mathrm{d}x^\nu + H(l_i \mathrm{d}x^i)^2. \tag{2.12}$$

The effective 4D Einstein equations then reduce to the form

$$R_{\alpha\beta} = -E_{\alpha\beta}, \tag{2.13}$$

where

$$E_{\alpha\beta} = {}^{(5)}C_{ABCD} n^A n^B e^C_\alpha e^D_\beta \tag{2.14}$$

is the *electric* part of the 5D Weyl tensor, used besides the $W_{\alpha\beta}$ tensor to describe the non-local gravitational effects of the bulk space onto the brane. Further, the relations

$$\Lambda_5 = -\frac{6}{l^2}, \quad G_4 = \frac{G_5}{l} \tag{2.15}$$

can be deduced from Eqs (2.7) and (2.9), assuming zero cosmological constant on the brane ($\Lambda_4 = 0$). Here,

$$l = \frac{6}{\lambda \kappa_5^2} \tag{2.16}$$

is the curvature radius of the anti-de Sitter spacetime. (Henceforth we set $G_4 = 1$.)

2.2 Photon motion in the braneworld Kerr spacetimes

The metric of rotating blackhole formed on the brane has analogical form as the Kerr-Newman metric (1.37), where the squared electric charge e^2 is replaced by tidal charge b [45].

The stress tensor on the brane $E_{\mu\nu}$ takes the form

$$E_t{}^t = -E_\varphi{}^\varphi = -\frac{b}{\Sigma^3}[\Sigma - 2(r^2+a^2)] \tag{2.17}$$

$$E_r{}^r = -E_\theta{}^\theta = -\frac{b}{\Sigma^2} \tag{2.18}$$

$$E_\varphi{}^t = -(r^2+a^2)\sin^2\theta E_t{}^\varphi = -\frac{2ba}{\Sigma^3}(r^2+a^2)\sin^2\theta \tag{2.19}$$

that is fully analogical ($b \to e^2$) to the components of electromagnetic energy-momentum tensor for the Kerr-Newman spacetimes in Einstein's general relativity [17]. For simplicity, we put $M = 1$ in the following, using thus dimensionless coordinates and parameters. The tidal charge can be both positive and negative; however, there are some indications favorizing negative values of b [28, 42]. Note that in the case of $b < 0$, some brany black holes have the ring singularity of spacelike character [28]. The geodetical motion in the braneworld Kerr spacetimes is given by the standard Carter equations (1.45) – (1.48).

Having particular geometry, which does not depend on azimuthal φ nor temporal t coordinates, the radial and latitudinal motion has to be discussed.

The photon motion (with fixed constants of motion E, Φ, Q) is allowed in regions where $R(r; E, \Phi, Q) \geq 0$ and $W(\theta; E, \Phi, Q) \geq 0$. The conditions $R(r; E, \Phi, Q) = 0$ and $W(\theta; E, \Phi, Q) = 0$ determine turning points of the radial and latitudinal motion, respectively, giving boundaries of the region allowed for the motion. Detailed analysis of the θ-motion can be found in [24, 29], while the radial motion was analysed (with restrictions implied by the θ-motion) in [56] and [55]. Here we extend this analysis to the case of $b < 0$.

The radial and latitudinal Carter equations read

$$\Sigma^2\left(\frac{\mathrm{d}r}{\mathrm{d}w'}\right)^2 = [r^2+a^2-a\lambda]^2 - \Delta[\mathcal{L} - 2a\lambda + a^2], \tag{2.20}$$

$$\Sigma^2\left(\frac{\mathrm{d}\theta}{\mathrm{d}w'}\right)^2 = \mathcal{L} + a^2\cos^2\theta - \frac{\lambda^2}{\sin^2\theta} \tag{2.21}$$

where we have introduced impact parameters

$$\lambda = \frac{\Phi}{E}, \tag{2.22}$$

$$\mathcal{L} = \frac{L}{E^2} = \frac{Q+\Phi^2}{E^2} = q + \lambda^2, \tag{2.23}$$

and rescaled the affine parameter by $w' = Ew$. We assume $a > 0$.

The reality conditions $(\mathrm{d}r/\mathrm{d}w')^2 \geq 0$ and $(\mathrm{d}\theta/\mathrm{d}w')^2 \geq 0$ lead to the restrictions on the impact parameter $\mathcal{L}$

$$\mathcal{L}_{min} \leq \mathcal{L} \leq \mathcal{L}_{max}, \tag{2.24}$$

where

$$\mathcal{L}_{max} \equiv \frac{(a\lambda - 2r + b)^2}{\Delta} + r^2 + 2r - b, \tag{2.25}$$

and

$$\mathcal{L}_{min} \equiv \begin{cases} \lambda^2 & \text{for} \quad |\lambda| \geq a, \\ 2a|\lambda| - a^2 & \text{for} \quad |\lambda| \leq a. \end{cases} \tag{2.26}$$

The upper(lower) constraint, $\mathcal{L}_{max}(\mathcal{L}_{min})$, comes from the radial-motion (latitudinal-motion) reality condition. The properties of the photon motion are determined by the behaviour of the surface $\mathcal{L}_{max}(r;\lambda,a,b)$, as given by (2.25). The extrema of the surface $\mathcal{L}_{max}$ (giving spherical photon orbits) are determined by

$$\lambda = \lambda_+ \equiv \frac{r^2+a^2}{a}, \tag{2.27}$$

$$\lambda = \lambda_- \equiv \frac{r^2 - br - a^2 - r\Delta}{a(r-1)}. \tag{2.28}$$

The values of $\mathcal{L}_{max}$ at these extreme points are given by

$$\mathcal{L}_{max}(\lambda_+) \equiv \mathcal{L}_+ = 2r^2 + a^2, \tag{2.29}$$

$$\mathcal{L}_{max}(\lambda_-) \equiv \mathcal{L}_- = \frac{2r(r^3 - 3r + 4b) + a^2(r+1)^2}{(r-1)^2}. \tag{2.30}$$

The character of the extrema follows from the sign of $\partial^2\mathcal{L}_{max}/\partial r^2$. One finds that

$$\frac{\partial^2 \mathcal{L}_{max}}{\partial r^2} = \frac{8r^2}{\Delta}, \quad \text{for} \quad \lambda = \lambda_+, \tag{2.31}$$

$$\frac{\partial^2 \mathcal{L}_{max}}{\partial r^2} = \frac{8r^2}{\Delta} - \frac{8r}{(r-1)^2}, \quad \text{for} \quad \lambda = \lambda_-. \tag{2.32}$$

Clearly, there are only minima of $\mathcal{L}_{max}$ along for $\lambda = \lambda_+$, corresponding to unstable spherical orbits.

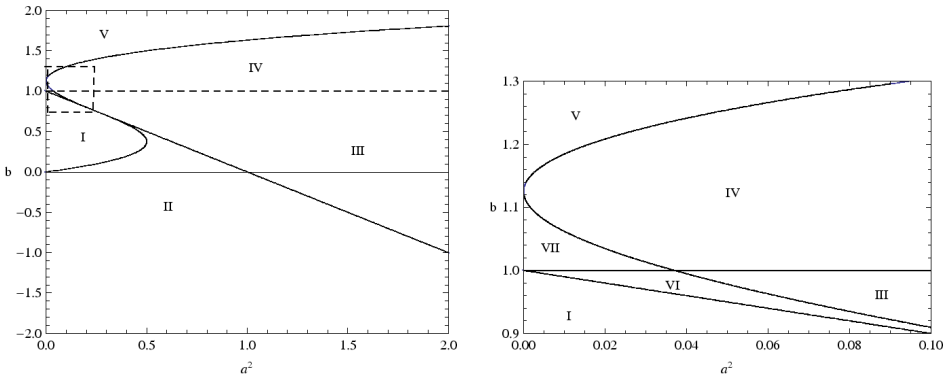

Figure 2.1: Left: classification of Kerr spacetime in braneworld universe according to the values of $a^2 + b$, b and n_{ext} (the number of local extrema of the curves $\tilde{\lambda}_\pm$, which is also the number of circular photon orbits in the equatorial plane). The classification regions are: I) for $a^2 + b \leq 1$ and $n_{ext} = 2$, II) for $a^2 + b \leq 1$ and $n_{ext} = 4$, III) $a^2 + b > 1$ and $b < 1$ and $n_{ext} = 2$, IV) for $a^2 + b > 1$ and $b > 1$ and $n_{ext} = 2$, V) for $a^2 + b > 1$ and $n_{ext} = 0$, VI) for $a^2 + b > 1$ and $b < 1$ and $n_{ext} = 4$, VII) for $a^2 + b > 1$ and $b > 1$ and $n_{ext} = 4$. Right: zoom of the area in the dashed rectangle of the left plot, to cover regions VI and VII.

Further, we have to determine where the restrictions given by the latitudinal motion $\mathcal{L}_{min}$ meet the restrictions on the radial motion $\mathcal{L}_{max}$. We find that $\mathcal{L}_{max} = \lambda^2$ (for $|\lambda| \geq a$) is fullfilled where

$$\lambda = \tilde{\lambda}_\pm \equiv \frac{a(b - 2r \pm r^2\sqrt{\Delta})}{r^2 - 2r + b}, \tag{2.33}$$

while $\mathcal{L}_{max} = 2a|\lambda| - a^2$ (for $|\lambda| < a$) is fullfilled where

$$\lambda = \bar{\lambda} \equiv \frac{1}{\Delta}[4r - r^2 - 2b - a^2 + 2\sqrt{\Delta(b - 2r)}]. \tag{2.34}$$

The extreme points of curves $\tilde{\lambda}_{\pm}$, which are also the intersection points of these curves with λ_{-}, are determined by the equation

$$f(r;a,b) \equiv r^4 - 6r^3 + (9+4b)r^2 - 4(3b+a^2)r + 4b(b+a^2) = 0. \quad (2.35)$$

The equation $f(r;a,b) = 0$ determines loci of the photon equatorial circular orbits; in an implicit form the radii are given by the condition

$$a^2 = a^2_{ph\pm}(r;b) = \frac{r^2(r-3)^2 + 4b(r^2-3r+b)}{4(r-b)}. \quad (2.36)$$

The maxima of the curve $\bar{\lambda}$, which also determine the intersections of curves $\bar{\lambda}$ and λ_{-} are located on r satisfying the equation

$$2r^3 - (3+b)r^2 + 2br + a^2 = 0. \quad (2.37)$$

The braneworld Kerr spacetimes can be classified due to the properties of the photon motion as determined by the behaviour of the functions $\lambda_{\pm}$, $\tilde{\lambda}_{\pm}$, $\bar{\lambda}$. The classification is governed by their divergences (i.e., by existence of the horizons) and the number of local extrema determining equatorial photon circular orbits n_{ex}. There exist seven classes of the braneworld Kerr spacetimes, with the criteria of separation being $a^2+b \lesseqgtr 1$, $b \lesseqgtr 1$ and n_{ex} . The classification is represented in Figure 2.1. There are two different classes of the black-hole spacetimes, differing by the presence of the photon circular orbits under the inner horizon. However, in the astrophysically relevant region outside the outer horizon, both the classes are of the same character, having two unstable equatorial photon circular orbits, one corotating (at r_{ph1}) and the other counter-rotating (at $r_{ph2} > r_{ph1}$). The tidal charge b introduces no qualitatively new feature into the behaviour of photon motion in the Kerr spacetimes, but the quantitative impact of $b < 0$ with high magnitude are quite relevant, as shown in next sections. All the braneworld Kerr black holes with tidal charge $b < 0$ belong to the class II discussed in the case of standard Kerr-Newman spacetimes [55]. We illustrate in Figures 2.2-2.4 functions $\lambda_{\pm}$, $\tilde{\lambda}_{\pm}$ and $\bar{\lambda}$ for such a black hole spacetime with parameters $a = 0.9$ and $b = -1.0$. In this case typical for braneworld Kerr black hole with $b < 0$ there exist ten significiant values of λ as given in Figures 2.2 - 2.4.

For each interval of λ as determined by the sequence of λ_A - λ_J introduced in Figure 2.2, there exists a characteristic type of behaviour of the restricting "radial" function $\mathcal{L}_{max}$ and its relation to the "latitudinal" restricting function $\mathcal{L}_{min}$. They can be found in [55] and will not be repeated here.

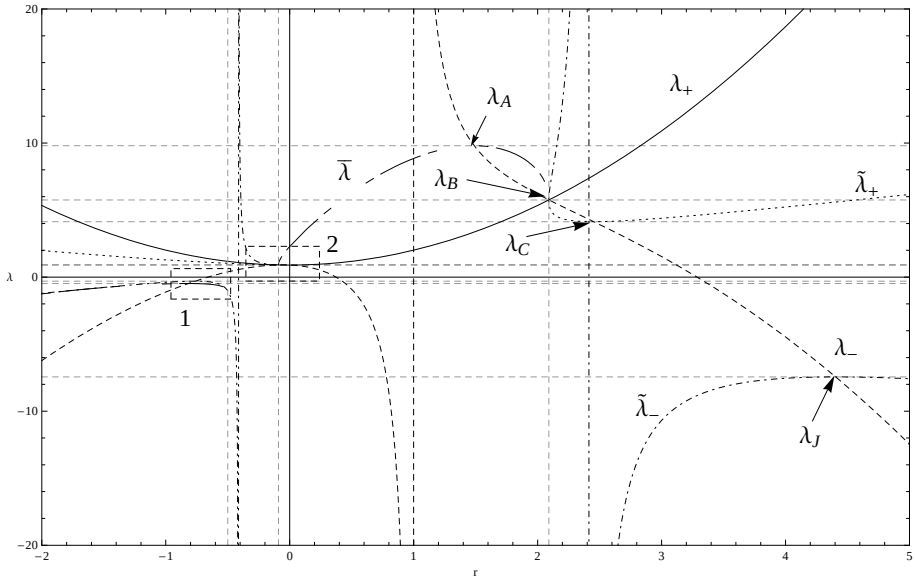

Figure 2.2: The graphs of the $\lambda_\pm$, $\tilde{\lambda}_\pm$ and $\bar{\lambda}$ functions are plotted for representative values of the parameters $a = 0.9$ and $b = -1.0$. The two dashed rectangle areas labeled with numbers 1 and 2 are zoomed in the following figures. The horizontal gray dashed lines represent special values of the impact parameter λ, denoted according to the text as $\lambda_A ... \lambda_J$.

The allowed values of the impact parameter $\mathcal{L}$ lie between the limiting functions $\mathcal{L}_{min}$ and $\mathcal{L}_{max}$. If the minimum $\mathcal{L}^{min}_{max} \equiv \mathcal{L}_{max}(r_{min}, \lambda_0)$ of the limiting function $\mathcal{L}_{max}$ is less than the value of the limiting function $\mathcal{L}_{min}$, an incoming photon ($k^r < 0$) travelling from infinity will return back for all values of $\mathcal{L}_0 \in [\mathcal{L}_{min}; \mathcal{L}_{max}]$. If $\mathcal{L}^{min}_{max} > \mathcal{L}_{min}$, the incoming photon ($k^r < 0$) travelling from infinity returns back if its impact parameter $\mathcal{L}_0$ satisfies the condition $\mathcal{L}_0 \geq \mathcal{L}^{min}_{max}$ and is captured by the black hole if $\mathcal{L}_0 < \mathcal{L}^{min}_{max}$. The minimum $\mathcal{L}^{min}_{max}$ determines (with the particular value of λ) a photon spherical orbit, i.e., a sphere where photons move with $r = const$ but with varying latitude θ (and, of course, varying φ). When the condition $\mathcal{L}_0 = \mathcal{L}_{min}$ is satisfied simultaneously, the spherical photon orbit is transformed to an equatorial photon circular orbit. Photons with $\mathcal{L}_0 = \mathcal{L}^{min}_{max}$ coming from distant regions or regions close to the black hole horizon will wind up around the photon sphere.

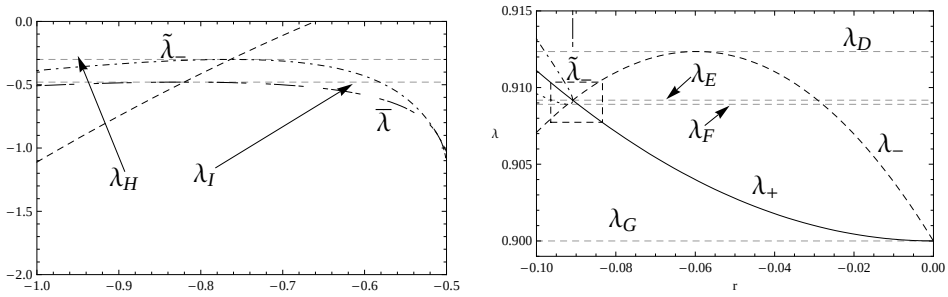

Figure 2.3: Left figure is the zoom of dashed area labelled 1 in previous figure. Right figure is the zoom of dashed area labelled 2 in previous figure. The dashed rectangle area here is zoomed in the next figure.

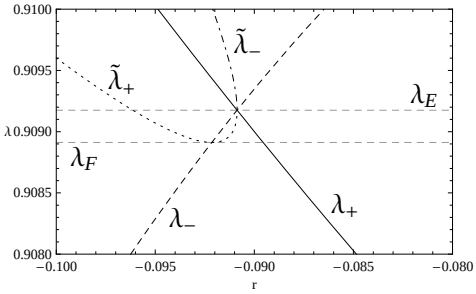

Figure 2.4: The zoom of the dashed rectangle area in previous figure.

2.3 Photon escape cones

From the knowledge of properties of radial and latitudinal motion of photon in braneworld geometry one may construct photon escape cone relative to particular observer (emitter).

2.3.1 Local frames of stationary and free-falling observers

We consider three families of stationary frames, namely $LNRF$ (Locally Nonrotatig Frame), SF (Static Frame) and $GF_{\pm}$(Circular Geodesic Frame) and one non-stationary frame, namely RFF (Radially Falling Frame). The $LNRF$ are of highest physical importance since the physical phenomena take the simplest form when expressed in such frames, because the rotational spacetime effects are maximally suppressed there [22, 45]. The $GF_{\pm}$ are directly related to Keplerian accretion discs in the equatorial plane of the

spacetime, both corotating and counterrotating, while RFF are related to free-falling spherical accretion. The SF are fixed relative to distant observers. The $GF_{\pm}$ and RFF are geodetical frames, while SF and $LNRF$ are generally accelerated frames.

The radial and latitudinal 1-forms of the three stationary frame tetrads are common for all three stationary cases and read

$$\omega^{(r)} = \left\{0, \sqrt{\Sigma/\Delta}, 0, 0\right\}, \tag{2.38}$$

$$\omega^{(\theta)} = \left\{0, 0, \sqrt{\Sigma}, 0\right\}. \tag{2.39}$$

$LNRF$ correspond to observers with $\Phi = 0$ (zero angular momentum observers). Their time and azimuthal 1-forms read

$$\omega^{(t)} = \left\{\sqrt{\frac{\Delta\Sigma}{A}}, 0, 0, 0\right\}, \tag{2.40}$$

$$\omega^{(\varphi)} = \left\{-\Omega_{LNRF}\sqrt{\frac{A}{\Sigma}}\sin\theta, 0, 0, \sqrt{\frac{A}{\Sigma}}\sin\theta\right\}. \tag{2.41}$$

where

$$\Omega_{LNRF} = \frac{a(2Mr - b)}{A} \tag{2.42}$$

is the angular velocity of $LNRF$ as seen by observers at infinity.

The tetrad of SF corresponding to observers with $\Omega = 0$,i.e. static relative to observers at infinity, is given by the formulae

$$\omega^{(t)} = \left\{\sqrt{1 - \frac{2r - b}{\Sigma}}, 0, 0, \frac{a(2r - b)\sin^2\theta}{\sqrt{\Sigma^2 - (2r - b)\Sigma)}}\right\}, \tag{2.43}$$

$$\omega^{(\varphi)} = \left\{0, 0, 0, \sqrt{\frac{\Delta\Sigma}{\Sigma - (2r - b)}}\sin\theta\right\}. \tag{2.44}$$

The $GF_{\pm}$ observers move along φ-direction in the equatorial plane with velocity $V_{GF\pm}$(+...corotating, -...counterrotating) relative to the $LNRF$ and with angular velocity Ω relative to the static observers at infinity given by [][SK]

$$\Omega_{\pm} = \pm\frac{\sqrt{r - b}}{r^2 \pm a\sqrt{r - b}}. \tag{2.45}$$

The velocity $V_{GF\pm}$ is given by

$$V_{GF\pm} = \pm\frac{(r^2+a^2)Y \mp a(2r-b)}{\sqrt{\Delta}(r^2 \pm aY)}. \tag{2.46}$$

where $Y = \sqrt{r-b}$. The standard Lorentz transformation of the $LNRF$ tetrad gives the tetrad of $GF_\pm$ in the form

$$\omega_\pm^{(t)} = \left\{\frac{r^2-2r+b\pm aY}{Z_\pm}, 0, 0, \mp\frac{(r^2+a^2)Y \mp a(2r-b)}{Z_\pm}\right\}, \tag{2.47}$$

$$\omega_\pm^{(\varphi)} = \left\{\mp\frac{\sqrt{\Delta}Y}{Z_\pm}, 0, 0, \frac{\sqrt{\Delta(r^2 \pm aY)}}{Z_\pm}, \right\} \tag{2.48}$$

where

$$Z_\pm = r\sqrt{r^2-3r+2b\pm 2aY}. \tag{2.49}$$

Note that the $GF_\pm$ family is restricted to the equatorial plane, while $LNRF$ are defined at any θ.

The RFF observers have velocity

$$V_{RFF} = \{V^{(r)}, V^{(\theta)}, V^{(\varphi)}\} \tag{2.50}$$

as measured in $LNRF$. The radially free-falling (or free-escaping) observers starting (finishing) at infinity move with $\theta = const$. Using the results of [58], we find the velocity components of the free-falling frames in the $LNRF$ frames

$$V^{(r)} = \pm\sqrt{1-\frac{\Sigma\Delta}{A}}, \tag{2.51}$$

$$V^{(\theta)} = 0, \tag{2.52}$$

$$V^{(\varphi)} = 0. \tag{2.53}$$

Clearly, the free-falling (free-escaping) observers move only radially in the $LNRF$, in analogy to particles radially moving in static frames of the Schwarzchild spacetimes. For the radially free-falling sources, the tetrad components $\omega^{(\theta)}$ and $\omega^{(\varphi)}$ coincide with those of the LNRF tetrad, while $\omega^{(t)}$ and $\omega^{(r)}$ are transformed. The local Lorentz transformation of the $LNRF$ to the $RFF_\pm$ tetrad yields

$$\omega_{\pm}^{(t)} = \left\{ \gamma \frac{\Delta\Sigma}{A}, \mp\sqrt{\frac{\Sigma}{\Delta}} V, 0, 0 \right\}, \tag{2.54}$$

$$\omega_{\pm}^{(r)} = \left\{ \mp\gamma\sqrt{\frac{\Delta\Sigma}{A}} V, \sqrt{\frac{\Sigma}{\Delta}}\gamma, 0, 0 \right\}, \tag{2.55}$$

$$\omega_{\pm}^{(\theta)} = \{0, 0, \sqrt{\Sigma}, 0\}, \tag{2.56}$$

$$\omega_{\pm}^{(\varphi)} = \left\{ -\Omega_{LNRF}\sqrt{\frac{A}{\Sigma}}\sin\theta, 0, 0, \sqrt{\frac{A}{\Sigma}}\sin\theta \right\}. \tag{2.57}$$

2.3.2 Construction of escape cones

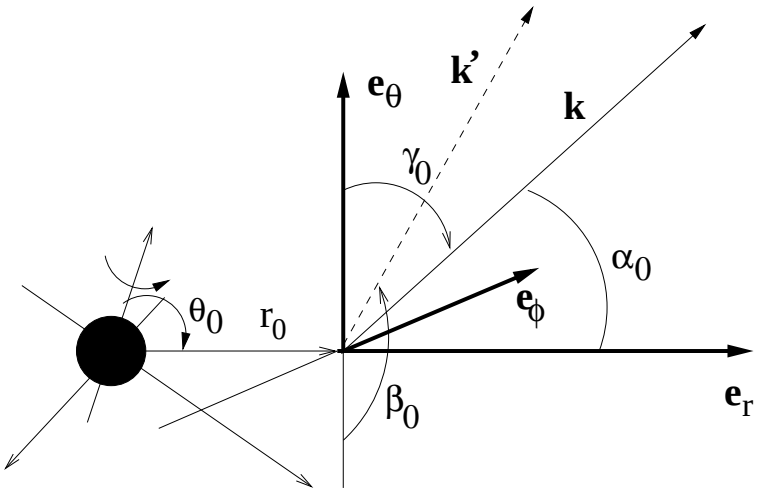

Figure 2.5: Definition of directional angles α_0, β_0 and γ_0 in a local frame. Vectors $\vec{e}_r$, $\vec{e}_\theta$, $\vec{e}_\varphi$ are the basic tetrad vectors. Position of the observer (source) is given by the coordinates (r_0, θ_0). Vector $\vec{k}$ represents a photon as observed by the observer in the given tetrad and vector $\vec{k}'$ is its projection into the plane ($\vec{e}_\theta$, $\vec{e}_\varphi$).

For each direction of emission in the local frame of a source, there is a corresponding pair of values of the impact parameters λ and $\mathcal{L}$ which can be related to the directional cosines of the photon trajectory in the local frame at the position of the source. Of course, the analysis of the turning points of the radial motion of photons, presented in the previous section, is crucial

in determining the local escape cones as the boundary of the escape cone is given by directional angles related to spherical photon orbits.

Projection of a photon 4-momentum $\vec{k}$ onto the local tetrad of an observer is given by the formulae

$$k^{(t)} = -k_{(t)} = 1, \tag{2.58}$$
$$k^{(r)} = k_{(r)} = \cos\alpha_0, \tag{2.59}$$
$$k^{(\theta)} = k_{(\theta)} = \sin\alpha_0\cos\beta_0, \tag{2.60}$$
$$k^{(\varphi)} = k_{(\varphi)} = \sin\alpha_0\sin\beta_0, \tag{2.61}$$

where α_0, β_0 are directional angles of the photon in the local frame (see Figure 2.5) and $\cos\gamma_0 = \sin\alpha_0\sin\beta_0$. In terms of the local tetrad components of the photon 4-momentum and the related directional angles, the conserved quantities, namely, the azimutal momentum Φ, energy E and K read

$$\Phi = k_\varphi = -\omega^{(t)}{}_\varphi k^{(t)} + \omega^{(r)}{}_\varphi k^{(r)} + \omega^{(\theta)}{}_\varphi k^{(\theta)} + \omega^{(\varphi)}{}_\varphi k^{(\varphi)}, \tag{2.62}$$
$$E = -k_t = \omega^{(t)}{}_t k^{(t)} - \omega^{(r)}{}_t k^{(r)} - \omega^{(\theta)}{}_t k^{(\theta)} - \omega^{(t)}{}_\varphi k^{(\varphi)}, \tag{2.63}$$
$$K = \frac{1}{\Delta}\left\{[E(r^2+a^2) - a\Phi]^2 - (\Sigma k^r)^2\right\}. \tag{2.64}$$

The impact parameters λ and $\mathcal{L}$ defined by relations (2.22) and (2.23) are thus fully determined by any double, D, of angles from the set $M = [\alpha_0, \beta_0, \gamma_0]$.

Having defined the source frame, we can construct light escape cones assuming fixed coordinates of the source r_0, θ_0. Their construction proceedes in the following steps:

- for given D, say $D = [\alpha_0, \beta_0]$, we calculate $\lambda = \lambda(\alpha_0, \beta_0)$,
- λ determines the behaviour of $\mathcal{L}_{max} = \mathcal{L}_{max}(r; \lambda)$,
- from the analysis presented in the previous section we calculate minimum of $\mathcal{L}_{max}$, which reads $\mathcal{L}^{min}_{max} = \mathcal{L}_{max}(r_{min}; \lambda)$,
- we search for such a double D which satisfies equation $\mathcal{L}_0(\alpha_0, \beta_0) = \mathcal{L}_{max}(r_{min}; \lambda)$.

Here, we present in detail the construction of light escape cones in particular case of the $LNRF$. The procedure is analogous for the other stationary frames and simply modified for the free-falling frames, being radius dependent.

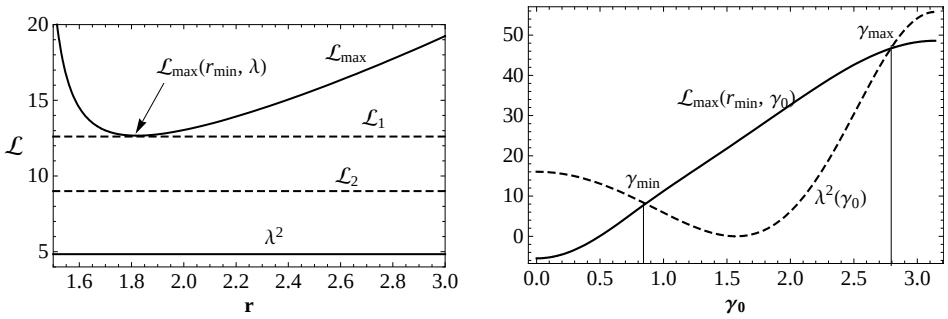

Figure 2.6: Left. The functions $\mathcal{L}_{max}$ and $\mathcal{L}_{min} = \lambda_0^2$ are plotted together with representative constant functions $\mathcal{L}_1$ and $\mathcal{L}_2$ to demonstrate the construction of the photon escape cone. Right. The intersections of $\mathcal{L}_{max}(\gamma_0)$ with $\lambda^2(\gamma_0)$ give the interval of relevant values of $\gamma_0 \in [\gamma_{min}; \gamma_{max}]$.

The impact parameter λ expressed in terms of the angle γ_0, related to the $LNRF$, reads

$$\lambda_0 = \frac{1}{\Omega_{LNRF0} + \frac{\Sigma_0\sqrt{\Delta_0}}{A_0 \sin\theta_0 \cos\gamma_0}}, \tag{2.65}$$

where index '0' refers to the frame with coordinates $[r_0, \theta_0]$. The minimum of $\mathcal{L}_{max}$ is located at

$$r_{min} = \begin{cases} \sqrt{a\lambda - a^2} & \text{for} \quad \lambda \geq \lambda_G = a \\ 1 - \frac{k_1}{k_2} + \frac{k_2}{3} & \text{for} \quad \lambda < \lambda_G = a \end{cases} \tag{2.66}$$

where

$$k_1 = a^2 + 2b + a\lambda - 3, \tag{2.67}$$

$$k_2 = \left\{27(1 - a^2 - b) + 2\sqrt{3}\sqrt{27(1 - a^2 - b)^2 + k_1^3}\right\}^{1/3}. \tag{2.68}$$

The relevant values of $\mathcal{L}$ lie between $\mathcal{L}_{max}$ and $\mathcal{L}_{min}$ determined by Eqs (2.25) and (2.26). The intersections of functions $\mathcal{L}_{max} = \mathcal{L}_{max}(\gamma_0)$ and $\mathcal{L}_{min}(\gamma_0)$ give the relevant interval of angles $\gamma \in [\gamma_{min}, \gamma_{max}]$ (see Figure 2.6). For each γ from $[\gamma_{min}, \gamma_{max}]$ we calculate minimal value of the photon impact parameter $\mathcal{L}$ for which the photon reaches the turning point r_{min} and escapes to infinity. This minimal value is the minimum of $\mathcal{L}_{max}$ which is located at r_{min}, eg. $\mathcal{L}_{max} = \mathcal{L}_{max}(r_{min}; \lambda_0(\gamma_0), a, b)$, where r_{min} is given by (2.66). Now we can calculate the value of α_0 using equation

$$\cos\alpha_0 = \frac{k^{(r)}}{k^{(t)}} = \frac{\omega^{(r)}_{LNRF\mu}k^\mu}{\omega^{(t)}_{LNRF\mu}k^\mu}. \tag{2.69}$$

We arrive to the formula

$$\cos\alpha_0 = \pm\sqrt{A_0}\frac{\sqrt{(r_0^2+a^2-a\lambda_0)^2-\Delta_0(\mathcal{L}^{min}_{max}-2a\lambda_0+a^2)}}{-a(a\sin^2\theta_0-\lambda_0)\Delta_0+(r_0^2+a^2)(r_0^2+a^2-a\lambda_0)}, \tag{2.70}$$

where $A_0 = A(r_0,\theta_0)$, $\Delta_0 = \Delta(r_0)$ and $\mathcal{L}^{min}_{max} = \mathcal{L}_{max}(r_{min};\lambda_0,a,b)$. The angle β_0 can be calculated from the formula (2.61). In this way we obtain angles from the arc $\beta_0 \in \langle -\pi/2;\pi/2\rangle$. The remaining arc $\beta_0 \in \langle \pi/2;3\pi/2\rangle$ can be obtained by turning the arc $\beta_0 \in \langle -\pi/2;\pi/2\rangle$ around the symmetry axis determined by angles $\beta_0 = -\pi/2$ and $\beta_0 = \pi/2$. This procedure can be done because photons released under angles β_0 and $\pi-\beta_0$ have the same constants of motion. Clearly, for sources under the radius corresponding to the corotating equatorial photon circular orbit, only outward directed photons with no turning point of the r-motion can escape. With radius of the source approaching the event horizon ($r_0 \to r_+$), the escape cone shrinks to infinitesimal extension, except the case of extreme black hole [22]. For the other frames considered here, the procedure of the related light escape cone construction can be directly repeated, but with the relevant tetrad 1-form components being used in the procedure.

2.3.3 Light escape cone - effect of tidal charge b

In order to reflect properly the effect of the tidal charge b on the escape cone structure, we shall give the cones for black hole sequences of two kind: first we keep the spin a fixed and change b, second we keep fixed "distance" to the extreme black hole states, i.e., a^2+b is fixed, and both a and b are changed. The positive tidal charges have tendency to slightly increase the asymmetry of the cones as compared with $b=0$ case, keeping its character similar to the case of Kerr black holes (see next section). Therefore, we focus our attention to the influence of negative tidal charges.

Behaviour of the $LNRF$ escape cones in dependence on the braneworld parameter b (and the spin a) is represented in Figures 2.7 and 2.8. The complementary trapped cones, corresponding to photons captured by the black hole, are shaded.

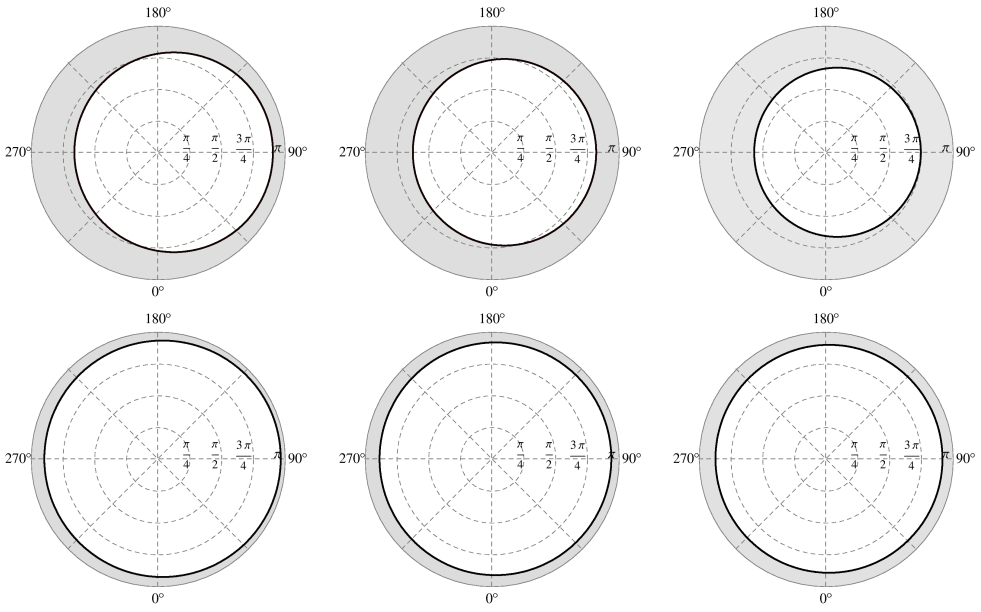

Figure 2.7: Light escape cones as seen by $LNRF$ in the vicinity of the braneworld kerr black hole. Top set of images is plotted for radial coordinate of emitter $r_e = 6M$ and bottom set for $r_e = 20M$. The rotational parameter $a = 0.9981$ is fixed and the representative values of the braneworld parameter b are 0 (left), -1 (middle) and -3 (right). The shaded area represents photons captured by black hole.

At a fixed radius expressed in units of M the extension of the trapped cone grows with descending of b to higher negative values and fixed spin a and mass M, demonstrating thus the growing gravitational pull of the black hole due to growing magnitude of the negative braneworld parameter.

The same statement holds also in the case of extreme Kerr black holes, when a grows and b descends, while M is fixed. Clearly, the positive braneworld parameters have tendency to increase the asymmetry of the cones, while the negative ones symmetrize the escape cones with growing of $|b|$. On the other hand, the asymmetry of the escape cone grows with descending of b for extreme black holes (Figure 2.8). Further, we represent the influence of the braneworld parameter on the escape cones for the circular (corotating) geodesic frames in Figure 2.9. Assuming astrophysically relevant sources in Keplerian accretion discs, their orbits must be located above the marginally stable orbit r_{ms}, determined implicitly by the condition [17, 60]

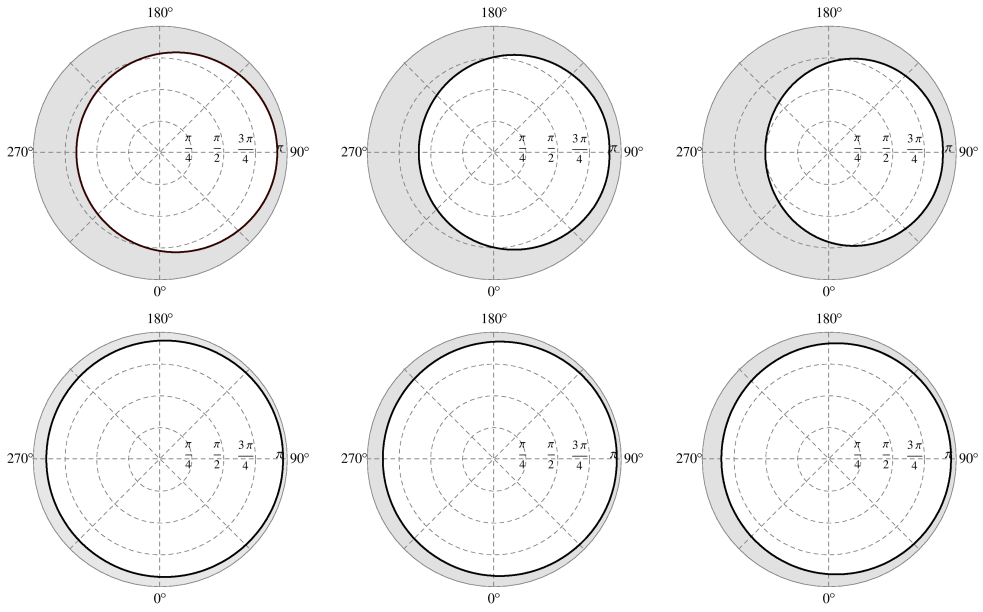

Figure 2.8: Light escape cones as seen by $LNRF$ in the vicinity of the extreme braneworld kerr black hole. Top set of images is plotted for radial coordinate of emitter $r_e = 6M$ and bottom set for $r_e = 20M$. The representative rotational and braneworld parameters $[a^2,b]$ are [1.0,0.0](left), [2.0,−1.0](middle) and [4.0,−3.0](right). The shaded area represents photons captured by black hole.

$$a = a_{ms}(r;b) \equiv \frac{4(r-b)^{3/2} \mp r\sqrt{3r^2 - 2r(1+2b) + 3b}}{3r - 4b}. \tag{2.71}$$

Therefore, we construct the escape cones for observers at $r = r_{ms}(a,b)$ and at fixed radii. In the sequence of black holes with fixed spin $a = 0.9981$ (Figure 2.9) we include also a subsequence of escape cones constructed at the same relative distance from the black hole horizon in order to better illustrate the role of the tidal charge b. In the sequence of near-extreme black holes with $a^2 + b = 0.9999$ (Figure 2.10) the third sequence is not necessary as the black hole horizon is fixed at $r_h = 1.01M$. Figures 2.9 and 2.10 demonstrate that the trapped cone expands as the tidal charge descends to lower negative values, both for black holes with fixed spin a and for near-extreme holes. On the other hand, considering the cones at r_{ms} we can conclude that the descending tidal charge ($b < 0$) symmetrizes their shape for fixed a, but makes them strongly asymmetric for near-extreme black holes

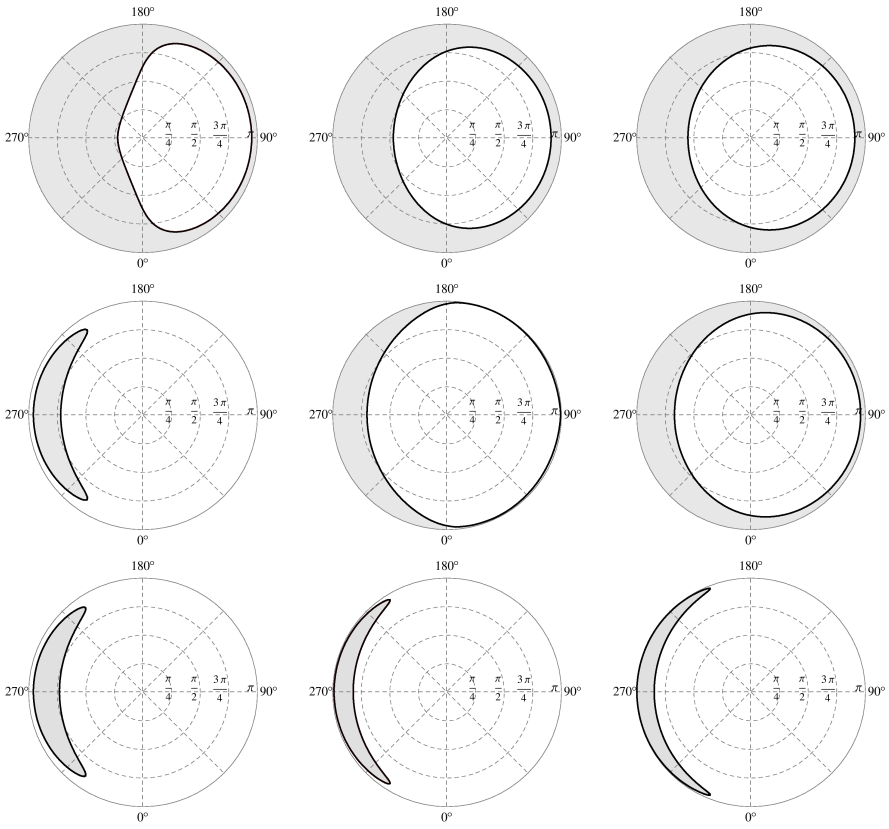

Figure 2.9: Escape cones of GF+ observers. Top images are plotted for observer (emitter) at $r = r_{ms}$, middle images $r = 10M$ and bottom images for $r = 10 \cdot r_h$. The value of $a = 0.9981$ is kept fixed. The representative values of b are (from left to right) 0.0, -1.0 and -3.

shrinking them strongly in the direction of the black hole rotation.

Finally we demonstrate the relevance of the tidal charge b in the character of escape cones of the free-falling frames (comparing them with those related to $LNRF$) in Figure 2.11. We construct the escape cones for two typical values of the tidal charge ($b = 0$, $b = -3$) in a sequence of radii where the free-falling source is radiating, demonstrating thus the combined growing influence of the black hole gravitational pull on the photon motion and the velocity of the free-falling source. In order to illustrate the phenomena in a clear way, we compare the free-falling frame escape cones to the corresponding $LNRF$ escape cones. Clearly, the tidal charge descending to higher negative values makes stronger squeezing of the free-falling cones relative to the $LNRF$ escape cones at any fixed radius. Notice, that the free-

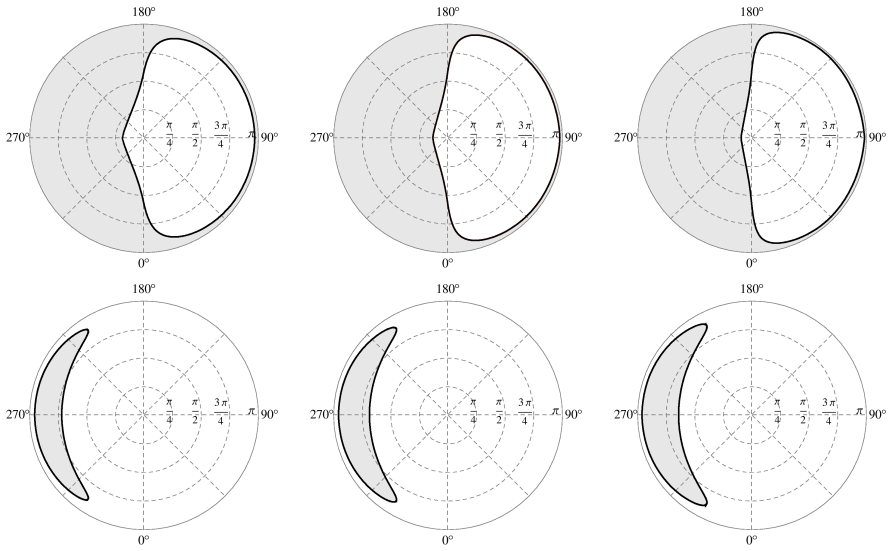

Figure 2.10: Escape cones of GF+ observers. Top images are plotted for observer (emitter) at $r = r_{ms}$ and bottom images for $r = 10M$. The value of $a^2 + b = 0.9999$ is kept fixed. The representative values of $(a^2; b)$ are (from left to right) $(0.9999; 0.0)$, $(1.9999; -1.0)$ and $(3.9999; -3)$.

falling frame and $LNRF$ cones are shifted due to the black hole rotational dragging.

Table 2.1: Table of relevant values of r_{ms} and r_h used in plots on Figs 2.9 and 2.10.

(a^2, b)	(0.9981,0.0)	(0.9981,-1.0)	(0.9981,-3.0)
r_{ms}	1.24M	3.91M	6.27M
r_h	1.062M	2.002M	2.73M

We again observe the tendency of negative brany parameters to symmetrize and squeze the escape cones. At a fixed r, the escape cones become smaller for growing $|b|$ due to stronger gravity. For completeness we present sequence of both the free-falling frames (RFF_{-}) and $LNRF$ escape cones at the three fixed radii for an extreme black hole with $b = -3$ and $a^2 = 4$. We observe that both the RFF_{-} and $LNRF$ cones are strongly shifted in the

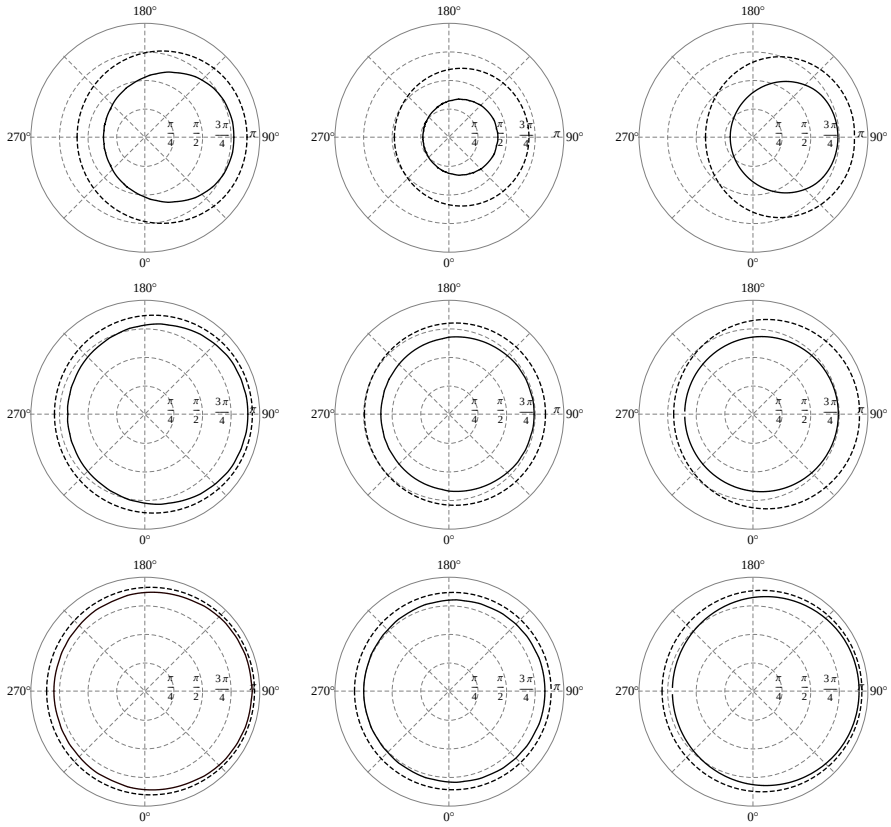

Figure 2.11: Comparison of the effect of the tidal charge b on the shape of light escape cones of locally nonrotating (dashed curves) frames and free falling (solid curves) frames. In the left column light escape cones are plotted for the tidal charge parameter $b = 0$ and in the middle one the light escape cones are plotted for $b = -3$. The spin $a = 0.9981$ is kept fixed in both columns. The right column gives the sequence of the escape cones for an extreme black hole with $[a^2 = 4; b = -3]$.

sense of the black hole rotation in vicinity of black hole horizon due to growing influence of the spin. The symmetrizing effect of descending values of negative tidal charge is canceled by strong influence of the rotational effects due to growing black hole spin.

2.4 Integration of photon trajectories

We express the integrals (2.113) and (2.115) in the form of the standard elliptic integrals of the first kind. Rauch and Blandford presented the tables

of reductions of u-integrals and μ-integrals for the case of photons in Kerr geometry [48]. Here we extended those reductions for the case of nonzero braneworld parameter b. Because the integration of the μ-integral does not depend on braneworld parameter b, the transformations are the same as in the case of Kerr metric [48], but we include them for completeness.

There are two cases we distinguish in latitudinal integral (see table 2.2). In the first case there is one positive, $M_+ > 0$, and one negative, $M_- < 0$ root of $M(m^2)$ it implies that there are two turning points located symmetrically about the equatorial plane given by $\pm\sqrt{M_+}$ (so called orbital motion [24, 29]. In the second case there are two positive roots, $0 < M_- < M_+$ of $M(m^2)$, which implies that the latitudinal motion is constrained to the region above or below of the equatorial plane (so called vortical motion). The relevant reductions of the integral $\int_{m_1}^{m} \mathrm{d}m'/\sqrt{M(m')} = I_M$ are stored in the table 2.2.

For distant observers we distinguish five relevant cases of the radial integral. These cases depend on the character of roots of the quartic equation $U(u) = 0$, i.e., on the number of turning points ($n_u = 0$ or $n_u = 1$) in the radial motion and the value of parameter $\tilde{q} = q(a^2 + b) + b(a - \lambda)^2$. We have arranged those transformations into table 2.3.

Denoting roots of the quartic equation $U(u) = 0$ by β_1, β_2, β_3 and β_4, the meaning of each of the five cases is the following:

- The **case I**: four distinct real roots of $U(u) = 0$ forming the sequence $\beta_1 > \beta_2 > \beta_2 > 0$ and $\beta_4 < 0$. The value of modified constant of motion $\tilde{q} > 0$.

- The **case II**: four real roots as in the case I but their values form the following order: $\beta_1 > \beta_2 > 0$ and $\beta_4 < \beta_3 < 0$. The value of modified constant of motion $\tilde{q} < 0$.

- The **case III**: two real and two complex roots of $U(u) = 0$: β_1 being a complex root, $\beta_2 = \bar{\beta_1}$ and $\beta_4 < \beta_3 < 0$. The value of modified constant of motion $\tilde{q} < 0$.

- The **case IV**: only complex roots: $\beta_2 = \bar{\beta_1}$ and $\beta_4 = \bar{\beta_3}$. The value of modified constant of motion $\tilde{q} < 0$.

- The **case V**: two real and two complex roots of $U(u) = 0$: $\beta_1 > 0$, $\beta_4 < 0$, β_2 being a complex root and $\beta_3 = \bar{\beta_2}$.

Using presented transformations we can write the integrals (2.113) and (2.115) in the form

Table 2.2: The reductions of $\int_{m_1}^{m} \mathrm{d}m'/\sqrt{M(m')} = I_M$

Case	$\tan\Psi$	m	c_1	m_1
$M_- < 0$	$\sqrt{\frac{M_+}{m^2}-1}$	$\frac{M_+}{M_+-M_-}$	$\frac{1}{\sqrt{a^2(M_+-M_-)}}$	$\sqrt{M_+}$
$M_- > 0$	$\sqrt{\frac{M_+-m^2}{m^2-M_-}}$	$\frac{M_+-M_-}{M_+}$	$\frac{1}{a^2}$	$\sqrt{M_+}$

Table 2.3: The reductions of $\int_{u_1}^{u} \mathrm{d}u'/\sqrt{U(u')} = I_U$

Case	$\tan\Psi$	m	c_1	u_1
I	$\sqrt{\frac{(\beta_1-\beta_3)(u-\beta_4)}{(\beta_1-\beta_4)(\beta_3-u)}}$	$\frac{(\beta_1-\beta_2)(\beta_3-\beta_4)}{(\beta_1-\beta_3)(\beta_2-\beta_4)}$	$\frac{2}{\sqrt{\tilde{q}(b1-b3)(b2-b4)}}$	β_4
II	$\sqrt{\frac{(\beta_1-\beta_2)(u-\beta_3)}{(\beta_1-\beta_3)(\beta_2-u)}}$	$\frac{(\beta_2-\beta_3)(\beta_1-\beta_4)}{(\beta_1-\beta_2)(\beta_4-\beta_3)}$	$\frac{2}{\sqrt{-\tilde{q}(b1-b2)(b3-b4)]}}$	β_3
III	$\frac{2c_2(u)}{\lvert 1-c_2^2(u)\rvert}$	$\frac{4c_4c_5-(\beta_3-\beta_4)^2-c_4c_5}{4c_4c_5}$	$\frac{1}{\sqrt{-\tilde{q}c_4c_5}}$	β_3
IV	$\frac{u-c_3}{\Im(\beta_1)(1+c_2^2)+c_2(u-c_3)}$	$1-\left(\frac{c_4-c_5}{c_4+c_5}\right)^2$	$\frac{2}{(c_4+c_5)\sqrt{-\tilde{q}}}$	c_3
V	$\frac{2c_2(u)}{\lvert 1-c_2^2(u)\rvert}$	$1-\frac{(c_4+c_5)^2-(\beta_1-\beta_4)^2}{4c_4c_5}$	$\frac{1}{\sqrt{\tilde{q}c_4c_5}}$	β_4

Table 2.4: Definitions for Table 2.3.

Case	${}^1c_2$	${}^1c_3$
III	$\left[\frac{c5(u-\beta_3)}{c_4(u-\beta_4)}\right]^{1/2}$	-
IV	$\left\{\frac{4[\Im(\beta_1)]^2-(c_4-c_5)^2}{(c_4+c_5)^2-4[\Im(\beta_1)]^2}\right\}^{1/2}$	$\Re(\beta_1)+c_2\Im(\beta_1)$
V	$\left[\frac{c4(u-\beta_4)}{c_5(\beta_1-u)}\right]^{1/2}$	-

Table 2.5: Definitions for Table 2.3 and Table 2.4.

Case	[1]c_4	[1]c_5
III	$\left\{[\Re(\beta_1)-\beta_3]^2+[\Im(\beta_1)]^2\right\}^{1/2}$	$\left\{[\Re(\beta_1)-\beta_4]^2+[\Im(\beta_1)]^2\right\}^{1/2}$
IV	$\left\{[\Re(\beta_1)-\Re(\beta_3)]^2+[\Im(\beta_1)+\Im(\beta_3)]^2\right\}^{1/2}$	$\left\{[\Re(\beta_1)-\Re(\beta_3)]^2+[\Im(\beta_1)-\Im(\beta_3)]^2\right\}^{1/2}$
V	$\left\{[\Re(\beta_2)-\beta_1]^2+[\Im(\beta_2)]^2\right\}^{1/2}$	$\left\{[\Re(\beta_2)-\beta_4]^2+[\Im(\beta_2)]^2\right\}^{1/2}$

[1] *The symbols $\Re(x)$ and $\Im(x)$ refer to real and imaginary part of x here.*

$$\int_{u_1}^{u}\frac{1}{\sqrt{U(\tilde{u})}}\mathrm{d}\tilde{u}=c_1\mathcal{F}(\Psi;m) \tag{2.72}$$

and

$$\int_{\mu_1}^{\mu}\frac{1}{\sqrt{M(\tilde{\mu})}}\mathrm{d}\tilde{\mu}=c_1\mathcal{F}(\Psi;m) \tag{2.73}$$

where $\mathcal{F}$ is the elliptic integral of the first kind and u_1(resp μ_1) depends on the case of root distribution of quartic equation $U(u)=0$ (resp. $M(\mu)=0$) as given in Table 2.3 (resp 2.2). If, in the cases III and V, the value of $1-c_2^2(u)<0$, we have to take instead of (2.72) the form

$$\int_{u_1}^{u}\frac{1}{\sqrt{U(\tilde{u})}}\mathrm{d}\tilde{u}=c_1(2\mathcal{K}(m)-\mathcal{F}(\Psi;m)), \tag{2.74}$$

where $\mathcal{K}$ is the complete elliptic integral of the first kind. In the case that $\mathrm{sign}(\mu 1\cdot\mu)<0$ we have to take instead of (2.73) the form

$$\int_{\mu_1}^{\mu}\frac{1}{\sqrt{M(\tilde{\mu})}}\mathrm{d}\tilde{\mu}=c_1(2\mathcal{K}(m)-\mathcal{F}(\Psi;m)), \tag{2.75}$$

where Ψ, m and c_1 are taken from table 2.2. We consider two basic possibilities of trajectories, namely those corresponding to direct and indirect images (Figures 2.22 and 2.23).

2.5 Optical effects in braneworld Kerr geometry

2.5.1 Silhuette of braneworld black hole

The silhuette of the black hole is quite naturally related to their trapped (escape) light cones. The marginal values of impact parameters λ_0 and $\mathcal{L}_0$(resp q_0) are obtained from the light escape cone. Using the stationarity of the braneworld Kerr spacetime we "shoot out" virtual photons from observer (static frame at very large distance r_0) and we are looking for the light escape cone of this virtual source (using the results of the previous section). The trapped light cone of this virtual source is constructed from the light escape cone of the virtual source by transformations of directional angle α_0 to $\bar{\alpha}_0 = \pi - \alpha_0$ and directional angle β_0 to $\bar{\beta}_0 = \beta_0$. In this way we get marginal directions for received photons from bright background behind the black hole. Then we can use the formulas (2.62), (2.63) and (2.64) to calculate the marginal values of λ_0 and $q_0(\mathcal{L}_0)$ in order to obtain the silhuette of the braneworld Kerr black hole in the plane $(\tilde{\alpha} - \tilde{\beta})$, i.e., the set of doubles $(\tilde{\alpha}_0, \tilde{\beta}_0)$ from equations (2.76) and (2.77). Here we plotted the silhuette directly from the trapped light cone $(\bar{\alpha}_0, \bar{\beta}_0)$ on the observer's sky $(\bar{\alpha}_0 \sin\bar{\beta}_0, \bar{\alpha}_0 \cos\bar{\beta}_0)$. Note that the angle $\bar{\alpha}_0$ is the radial coordinate and the angle $\bar{\beta}_0$ is the polar coordinate in the polar graph of the silhuette.

Assuming that distant observers measure photon directions relative to the symmetry center of the gravitational field, the component of the angular displacement perpendicular to the symmetry axis is given by $-p^{(\varphi)}/p^{(t)}$ (for black hole rotating anticlockwise relative to distant observers), while for angular displacement parallel to the axis it is given by $p^{(\theta)}/p^{(t)}$. These angles are proportional to $1/r_0$, therefore, it is convenient to use the impact parameters in the form independent of r_0 [22]

$$\tilde{\alpha} = -r_0 \frac{p^{(\varphi)}}{p^{(t)}} = -\frac{\lambda}{\sin\theta_0}, \tag{2.76}$$

and

$$\begin{aligned} \tilde{\beta} &= r_0 \frac{p^{(\theta)}}{p^{(t)}} = \left[q + a^2\cos^2\theta_0 - \lambda^2\cot^2\theta_0\right]^{1/2} \\ &= \left[\mathcal{L} + a^2\cos^2\theta - \frac{\lambda^2}{\sin^2\theta_0}\right]^{1/2}. \end{aligned} \tag{2.77}$$

Photon trajectories reaching the observer are represented by points in the

$(\tilde{\alpha} - \tilde{\beta})$ plane representing a small portion of the celestial sphere of the observer.

The shape of the black hole silhuette is the boundary of the no-turning-point region, i.e., it is the curve $\mathcal{L} = \mathcal{L}^{min}_{max}(\lambda)$ expressed in the $(\tilde{\alpha} - \tilde{\beta})$ plane of the impact parameters. For observers in the equatorial plane ($\theta_0 = \pi/2$), $\tilde{\alpha} = -\lambda$, $\tilde{\beta} = (\mathcal{L} - \lambda^2)^{1/2} = q^{1/2}$.

We consider that the black hole is observed by static distant observers. Therefore, we shall use the static frames introduced above. The silhuette of the black hole is quite naturally related to their trapped (escape) light cones.

The marginal values of impact parameters λ_0 and $\mathcal{L}_0$(resp q_0) are obtained from the light escape cone. Using the stationarity of the braneworld Kerr spacetime we "shoot out" virtual photons from observer (static frame at very large distance r_0) and we are looking for the light escape cone of this virtual source (using the results of the previous section). The trapped light cone of this virtual source is constructed from the light escape cone of the virtual source by transformations of directional angle α_0 to $\bar{\alpha}_0 = \pi - \alpha_0$ and directional angle β_0 to $\bar{\beta}_0 = \beta_0$. In this way we get marginal directions for received photons from bright background behind the black hole. Then we can use the formulas (2.62), (2.63) and (2.64) to calculate the marginal values of λ_0 and $q_0(\mathcal{L}_0)$ in order to obtain the silhuette of the braneworld Kerr black hole in the plane $(\tilde{\alpha} - \tilde{\beta})$, i.e., the set of doubles $(\tilde{\alpha}_0, \tilde{\beta}_0)$ from equations (2.76) and (2.77). Here we plotted the silhuette directly from the trapped light cone $(\bar{\alpha}_0, \bar{\beta}_0)$ on the observer's sky $(\bar{\alpha}_0 \sin\bar{\beta}_0, \bar{\alpha}_0 \cos\bar{\beta}_0)$. Note that the angle $\bar{\alpha}_0$ is the radial coordinate and the angle $\bar{\beta}_0$ is the polar coordinate in the polar graph of the silhuette.

2.5.2 Frequency shift

Radiation from Keplerian ring

In the case of static distant observer the 4-velocity reads $\mathbf{u}_o = (1, 0, 0, 0)$. In the case of emitter following a circular geodesic at $r = r_e$ in the equatorial plane of the brany Kerr black hole, the 4-velocity reads $\mathbf{u}_e = (u^t_e, 0, 0, u^\varphi_e)$ with components being given by

$$u^t_e = \left[1 - \frac{2}{r_e}(1 - a\Omega)^2 - (r_e^2 + a^2)\Omega^2 + \frac{b}{r_e^2}(1 - 2a\Omega)\right]^{-1/2}, \quad (2.78)$$

$$u^\varphi_e = \Omega u^t_e, \quad (2.79)$$

where Ω is the angular velocity of the emitter as seen by distant observer and is given by Eq.(2.45). The total frequency shift, including both the

gravitational and Doppler shifts, is given by

$$g = \frac{\left[1 - \frac{2}{r_e}(1 - a\Omega)^2 - (r_e^2 + a^2)\Omega^2 + \frac{b}{r_e^2}(1 - 2a\Omega)\right]^{1/2}}{1 - \lambda\Omega}, \tag{2.80}$$

where $\lambda = -k_\varphi/k_t$ is the impact parameter of the photon being a constant of the photon motion; notice that in our case of equatorial sources g is explicitly independent of the second motion constant q. Of course, depending on the position of the emitter along the circular orbit, the motion constant of photons reaching a fixed distant observer will change periodically (see, e.g., [21]).

Radiation from bright background

Here the LNRF at fixed radial and latitudinal coordinate in the vicinity of braneworld Kerr black hole is assumed. The radiation is emitted by distant, static isotropic and monochromatic sources forming bright background. The 4-velocity of the source is $\mathbf{u}_e = (1, 0, 0, 0)$ and $\mathbf{u}_o = (u_e^t, 0, 0, u_e^\varphi)$. From normalization condition for 4-velocity $\mathbf{u}\cdot\mathbf{u} = -1$ one determines the temporal component of LNRF 4-velocity, which reads

$$(u_o^t)^2 = \frac{1}{(\Sigma - 2r + b)\Omega^2 - 2(b - 2r)\sin^2\theta_o\Omega - A} \tag{2.81}$$

where the angular velocity Ω is given by (2.42). From the formula (1.54) the redshift parameter reads

$$g = u_o^t(1 + \Omega\lambda) \tag{2.82}$$

where impact parameter λ is given by formula (2.65). We finally arrive to formula

$$\begin{aligned} g &= \frac{1}{\sqrt{(\Sigma - 2r + b)\Omega^2 - 2(b - 2r)\sin^2\theta_o\Omega - A}} \\ &\times \left[1 + \frac{\Omega}{\Omega + (\Sigma\sqrt{\Delta})/(A\sin\theta\cos\gamma)}\right]. \end{aligned} \tag{2.83}$$

2.5.3 Focusing of the photon beam

For a distant observer located at the distance d_0 from the source the solid angle $\mathrm{d}\Pi$ can be expressed in terms of observer's plane coordinates $[\bar{\alpha}, \bar{\beta}]$ by formula (1.55).

The observer's plane coordinates are in relation with photon's impact parameters λ and q given by formulae [26, 22]

$$\alpha = -\frac{p^{(\phi)}}{p^{(t)}} = -\frac{\lambda}{\sin\theta_o}, \tag{2.84}$$

and

$$\beta = \frac{p^{(\theta)}}{p^{(t)}} = \pm\sqrt{q^2 + a^2\cos^2\theta_o - \lambda^2\cot^2\theta_o}; \tag{2.85}$$

therefore, we can switch the integration over λ and q. The solid angle $\mathrm{d}\Pi$ is then given by expression (1.56) with Jacobian $|\partial(\alpha,\beta)/\partial(\lambda,q)|$ of the transformation $(\bar{\alpha},\bar{\beta}) \to (\lambda, q)$ in the form

$$\left|\frac{\partial(\alpha,\beta)}{\partial(\lambda,q)}\right| = \frac{q}{\sin\theta_o\sqrt{q^2 + a^2\cos^2\theta_o - \lambda^2\cot^2\theta_o}}. \tag{2.86}$$

The impact parameters λ and q can be expressed in terms of the azimuthal, ϕ_e , and radial , r_e , position of the emitter.

We calculate derivatives $\partial r_e/\partial\lambda$ and $\partial r_e/\partial q$ from the condition

$$\begin{aligned} H(r_e,\lambda,q) &\equiv u_{sgn}\left[\int_{1/r_e}^{u_t}\frac{\mathrm{d}u}{\sqrt{U}} + (-1)^{n_u-1}\int_{u_o}^{u_t}\frac{\mathrm{d}u}{\sqrt{U}}\right] \\ &- \mu_{sgn}\left[\int_{\mu_e}^{\mu_\pm}\frac{\mathrm{d}\mu}{\sqrt{M}} + (-1)^{n_\mu-1}\int_{\mu_o}^{\mu_\pm}\frac{\mathrm{d}u}{\sqrt{U}} + p\int_{\mu_\mp}^{\mu_\pm}\frac{\mathrm{d}\mu}{\sqrt{M}}\right] \\ &= 0, \end{aligned} \tag{2.87}$$

where the turning points u_t and μ_t are functions of the impact parameters λ and q as well as the radial and latitudinal motion functions $U = U(u,\lambda,q)$ and $M = M(\mu,\lambda,q)$. The functions U and M give the radial and latitudinal photon motion in terms of the variables $u \equiv 1/r$ and $\mu \equiv \cos\theta$ (see [48]) by the relations

$$\begin{aligned} U(u;\lambda,q) &\equiv 1 + (a^2 - \lambda^2 - q^2)u^2 + 2[(\lambda - a)^2 + q^2]u^3 \\ &\quad -[b(a-\lambda)^2 + (a^2+b)q^2]u^4, \end{aligned} \tag{2.88}$$

$$M(\mu;\lambda,q) \equiv q^2 + (a^2 - \lambda^2 - q^2)\mu^2 - a^2\mu^4. \tag{2.89}$$

H is an implicit function of r_e, λ and q. From the implicit function theorem we find the derivatives to be

$$\frac{\partial r_e}{\partial\lambda} = -\frac{\partial H/\partial\lambda}{\partial H/\partial r_e}; \quad \frac{\partial r_e}{\partial q} = -\frac{\partial H/\partial q}{\partial H/\partial r_e}, \tag{2.90}$$

and after introducing the parameter

$$p = [n_\mu(1 - \mathrm{mod}(n_\mu, 2)) + (n_\mu - 1)\mathrm{mod}(n_\mu, 2)] \tag{2.91}$$

where $n_u(n_\mu)$ determines the number of turning points of the photon radial (latitudinal) motion, we arrive to the relation

$$\begin{aligned}
\frac{\partial H}{\partial s} &= u_{sgn}\left[\int_{1/r_e}^{u_t} -\frac{\partial U/\partial s}{2U^{3/2}}\mathrm{d}u + (-1)^{n_u-1}\int_{u_o}^{u_t} -\frac{\partial U/\partial s}{2U^{3/2}}\mathrm{d}u\right] \\
&+ u_{sgn}\frac{\partial u_t}{\partial s}\frac{1}{\sqrt{U(u_t)}}(1 + (-1)^{n_u-1}) \\
&- \mu_{sgn}\left[\int_{\mu_e}^{\mu_\pm} -\frac{\partial M/\partial s}{2M^{3/2}} + (-1)^{n_\mu-1}\int_{\mu_o}^{\mu_\pm} -\frac{\partial M/\partial s}{2M^{3/2}} + p\int_{\mu_\mp}^{\mu_\pm} -\frac{\partial M/\partial s}{2M^{3/2}}\right] \\
&- \mu_{sgn}\left[\frac{\partial \mu_\pm}{\partial s}\frac{1}{\sqrt{M(\mu_\pm)}}(1 + (-1)^{n_\mu-1} + p) - \frac{p}{\sqrt{M(\mu_\mp)}}\frac{\partial \mu_\mp}{\partial s}\right]
\end{aligned} \tag{2.92}$$

with s being replaced for λ or q, and

$$\frac{\partial H}{\partial r_e} = \frac{1}{\sqrt{U(1/r_e)}r_e^2}. \tag{2.93}$$

If $n_u = 0$ and $n_\mu = 0$ this formulas are easily enumerable, but in other cases there is a problem with integration in turning points (the integrals diverge) and there are some other terms which also diverge. Expressing the effective potentials in the form (see [67])

$$U(u, \lambda, q) \equiv (u_t - u)P(u, \lambda, q); \quad M(\mu, \lambda, q) \equiv (\mu_\pm - \mu)W(\mu, \lambda, q) \tag{2.94}$$

we can avoid this problem. As an example let's take $n_u = 1$ and transform the term

$$T = \int_{1/r_e}^{u_t} -\frac{\partial U/\partial s}{2U^{3/2}}\mathrm{d}u + \frac{\partial u_t}{\partial s}\frac{1}{\sqrt{U(u_t)}} \tag{2.95}$$

using (2.94). After some algebra one arrives to formula

$$T = \int_{1/r_e}^{u_t} -\frac{(\partial P/\partial s) + (\partial P/\partial u)(\partial u_t/\partial s)}{2P\sqrt{U}} + \frac{\partial u_t}{\partial s}\left(\frac{1}{\sqrt{u_e}} + \frac{1}{\sqrt{u_o}}\right), \tag{2.96}$$

which is now enumerable. The terms in μ part of (2.92) are transformed in the same way. The partial derivatives of the turning points can be also found from the implicit formula

$$U(u_t, \lambda, q) = 0 \quad \Rightarrow \quad \frac{\partial u_t}{\partial s} = -\frac{\partial U/\partial s}{\partial U/\partial u_t}, \tag{2.97}$$

where, again, s is replaced with λ and q.

From the Carter equation for the azimuthal coordinate

$$\phi_e = -u_{sgn}\left[\int_{1/r_e}^{u_t} \frac{f_U}{\sqrt{U}}\mathrm{d}u + (-1)^{n_u-1}\int_{u_o}^{u_t}\frac{f_U}{\sqrt{U}}\mathrm{d}u\right] \tag{2.98}$$

$$- \mu_{sgn}\left[\int_{\mu_e}^{\mu_\pm}\frac{f_M}{\sqrt{M}}\mathrm{d}\mu + (-1)^{n_\mu-1}\int_{\mu_o}^{\mu_\pm}\frac{f_M}{\sqrt{M}} + p\int_{\mu_\mp}^{\mu_\pm}\frac{f_M}{\sqrt{M}}\mathrm{d}\mu\right] \tag{2.99}$$

with

$$f_U = [2(a-l)u + l]/(1 - 2u + a^2u^2) \tag{2.100}$$

and

$$f_M = l\mu^2/(1-\mu^2), \tag{2.101}$$

we calculate the derivatives $\partial\phi_e/\partial\lambda$ and $\partial\phi_e/\partial q$ having in mind that $r_e = r_e(\lambda, q)$. From the above calculations we can form the Jacobian of transformation $(\lambda, q) \to (r_e, \phi_e)$ in the form

$$\left|\frac{\partial(\lambda,q)}{\partial(r_e,\phi_e)}\right| = \left|\frac{\partial(r_e,\phi_e)}{\partial(\lambda,q)}\right|^{-1} = \left|\frac{\partial r_e}{\partial\lambda}\frac{\partial\phi_e}{\partial q} - \frac{\partial r_e}{\partial q}\frac{\partial\phi_e}{\partial\lambda}\right|^{-1}. \tag{2.102}$$

The formula for the solid angle $\mathrm{d}\Pi$ then reads

$$\mathrm{d}\Pi = \frac{q}{\sin\theta_o\sqrt{q^2 + a^2\cos^2\theta_o - \lambda^2\cot^2\theta_o}}\left|\frac{\partial r_e}{\partial\lambda}\frac{\partial\phi_e}{\partial q} - \frac{\partial r_e}{\partial q}\frac{\partial\phi_e}{\partial\lambda}\right|^{-1}\mathrm{d}r_e\mathrm{d}\phi_e. \tag{2.103}$$

2.5.4 Light curve of a hot spot on a circular keplerian orbit

We model following situation. A monochromatic isotropically radiating hot spot follows the circular geodesic with radius r_e in the equatorial plane. The flux that observer at infinity measures is

$$\mathrm{d}F_o = I_o \mathrm{d}\Pi, \tag{2.104}$$

where $I_o = g^4 I_e$ [45]. I_e is a function of radial position of the emitter. Since we study here the light curve of a single hot spot on the circular geodesic, we normalize $I_e = 1$. Putting (2.103) into (2.104), the differential of the observed flux then reads

$$\mathrm{d}F_o = \frac{1}{d_o^2} \frac{q g^4(\phi_e, r_e)}{\sin\theta_o \sqrt{q^2 + a^2\cos^2\theta_o - \lambda^2 \cot^2\theta_o}} \left| \frac{\partial r_e}{\partial \lambda}\frac{\partial \phi_e}{\partial q} - \frac{\partial r_e}{\partial q}\frac{\partial \phi_e}{\partial \lambda} \right|^{-1} \mathrm{d}r_e \mathrm{d}\phi_e. \tag{2.105}$$

The light curve of such a radiating spot could be obtained by introducing the time dependence of the radiation received by the distant observer, including the time-delay effects related to the relativistic motion [21]. Here we consider another situation, namely the stationary line profile generated by a ring of orbiting hot spots, postponing the light curves of isolated hot spots to future studies.

These results could be directly applied to calculate line profile generated by some part of the internal region of the accretion disc, assuming some reasonable emissivity law, since such a part of the disc can be represented as being composed from radiating rings. Such a study will be presented in the future study, now being under preparation.

2.5.5 Spectral line profile of radiating keplerian ring

We directly apply the results of the previous section to determine the spectral line profile of the bright ring in the equatorial plane of brany Kerr black hole.

Let the source radiates isotropically at a fixed frequency ν_e. The specific intensity I_e of the source is then given by

$$I_e(\nu_e) = \epsilon(r)\delta(\nu_e - \nu_0), \tag{2.106}$$

where $\epsilon(r)$ is the local emissivity given as a function of the radial coordinate of the black hole spacetime, ν_0 is the rest frequency. Using (2.106) and (2.105) we arrive to the formula for the specific flux in the form

$$F_o(\nu_o) = \int \epsilon(r) g^4 \delta(\nu_o - g\nu_0)\mathrm{d}\Pi. \tag{2.107}$$

Here, since we calculate the profiled spectral line of a single radiating ring, the emissivity function can be normalized by $\epsilon(r) = 1$. We rearrange the solid angle formula (2.103) for the calculation of the specific flux to the form

$$\mathrm{d}\Pi = \frac{q}{\sin\theta_o\sqrt{q^2+a^2\cos^2\theta_o-\lambda^2\cot^2\theta_o}}\left|\frac{\partial r_e}{\partial\lambda}\frac{\partial g}{\partial q}-\frac{\partial r_e}{\partial q}\frac{\partial g}{\partial\lambda}\right|^{-1}\mathrm{d}g\mathrm{d}r_e. \quad (2.108)$$

Using Eqs. (2.108) and (2.107) we finally arrive to

$$F_o(g) = \int \frac{q}{d_o^2\sin^2\theta_o\sqrt{q^2+a^2\cos^2\theta_o-\lambda^2\cot^2\theta_o}}\left|\frac{\partial r_e}{\partial\lambda}\frac{\partial g}{\partial q}-\frac{\partial r_e}{\partial q}\frac{\partial g}{\partial\lambda}\right|^{-1}\mathrm{d}r_e. \quad (2.109)$$

2.5.6 Images of isoradial geodesics

Calculating images of an accretion disc (ring) in the equatorial plane of a braneworld Kerr black hole is the first step to calculate the optical phenomena. Generally one could obtain a direct and an indirect image (see Figures 2.22 and 2.23), but in special cases the situation can be much more complicated due to complex character of the latitudinal and azimuthal photon motion. Here we focus our attention to the direct and indirect images of isoradial geodesics.

In order to find all relevant positions of points forming the rotating ring on observer's sky, we have to find photon trajectories between the ring particles and the observer, i.e., we seek for such doubles of local observational angles $[\alpha_0, \beta_0]$ that satisfy the condition

$$I_U(\alpha_0,\beta_0;n_u,u_{sgn}) - I_M(\alpha_0,\beta_0;n,p,s) = 0. \quad (2.110)$$

Here we introduced the modified radial coordinate $u = 1/r$ and cosine of latitudinal coordinate $\mu = \cos\theta$ [48]. In the condition (2.110) n_u is the number of turning points in u coordinate, n is the number of turning points passed in μ coordinate, $p = mod(n, 2)$, $s = (1 - \mu_{sgn})/2$. In terms of u and μ we define the functions I_U and I_M by

$$I_U(\alpha_0,\beta_0;n_u,u_{sgn}) \equiv \begin{cases} -u_{sgn}\left(\int_{u_t}^{u_0}+\int_{u_t}^{u_e}\right) & \text{for} \quad n_u = 1 \\ u_{sgn}\int_{u_0}^{u_e} & \text{for} \quad n_u = 0 \end{cases} \quad (2.111)$$

and

$$\begin{aligned} I_M(\alpha_0,\beta_0;n,p,s) &\equiv \mu_{sgn}\left[\int_{\mu_0}^{\mu_+} + (-1)^{n+1}\int_{\mu_e}^{\mu_+} + \right. \quad (2.112)\\ &+ \left. (-1)^s[(1-p)n + p[(1-s)(n-1)+s(n+1)]]\int_{\mu_-}^{\mu_+}\right] \end{aligned}$$

with

$$\int_{u_1}^{u_2} \equiv \int_{u_1}^{u_2} \frac{\mathrm{d}u}{\sqrt{U(u)}}, \tag{2.113}$$

$$\begin{aligned} U(u) &= 1 + (a^2 - \lambda^2 - q)u^2 + 2[(\lambda^2 - a^2)^2 + q]u^3 - \\ &- [q(a^2 + b) + b(a - \lambda)^2]u^4 \end{aligned} \tag{2.114}$$

and

$$\int_{\mu_1}^{\mu_2} \equiv \int_{\mu_1}^{\mu_2} \frac{\mathrm{d}\mu}{\sqrt{M(\mu)}}, \tag{2.115}$$

$$M(\mu) = q + (a^2 - \lambda^2 - q)\mu^2 - a^2\mu^4. \tag{2.116}$$

2.5.7 Time delay

For optical effects in vicinity of a black hole, the time delay in case of systems varying with time and observed along two different directions due to the light deflection in strong gravity can be important [77]. The coordinate time that elapses from the instant of photon emission, t_e, to the instant of its reception, t_o, is integrated from the Carter equations and reads

$$\begin{aligned} t_o &= t_e + \mu_{sgn} \int_{\mu_e}^{\mu_o} a^2\mu^2 \frac{\mathrm{d}\mu}{\sqrt{M}} \\ &\quad + u_{sgn} \int_{u_e}^{u_o} \frac{2a(a - \lambda)u^3 + a^2u^2 + 1 + ab(\lambda - a)u^4}{(u/u_+ - 1)(u/u_- - 1)\sqrt{U}} \mathrm{d}u \end{aligned} \tag{2.117}$$

In order to succesfully integrate this formula, one must map all the turning points in μ and u motion to correctly set up the signs u_{sgn} and μ_{sgn}.

Suppose that the two light beams, direct and indirect, are emitted at the same coordinate time t_e. They generally reach the observer at different coordinate times t_o^{dir}(t_o^{indir} resp.). By time delay we define here the difference $\Delta t \equiv t_o^{\mathrm{indir}} - t_o^{\mathrm{dir}}$.

2.6 Effect of tidal charge on optical phenomena - results of the numerical code

In this section the influence of tidal charge parameter b on the shape of escape cone, the silhuette of braneworld Kerr black hole, frequency shift and the spectral line profile of radiating keplerian ring and time delays.

2.6.1 Silhuette

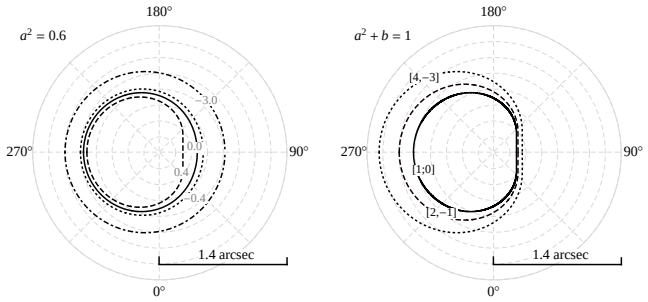

Figure 2.12: *Left figure. The* $(\bar{\alpha}_0, \bar{\beta}_0)$ *plots of the silhuettes of braneworld Kerr black hole on a bright background for rotational parameter* $a^2 = 0.6$ *and four representative values of tidal charge parameter* $b = -3.0$, $b = -0.4$, $b = 0.0$ *and* $b = 0.4$. *The observer is located at* $r_0 = 10^4 M$ *and* $\theta_0 = 90°$. *Right figure. The silhuettes of extreme black holes for three representative values of braneworld parameter* $b = 0$ *(solid),* $b = -1$ *(dashed) and* $b = -3$ *(dotted). Static observer is in equatorial plane at radial distance from the centre* $r_0 = 10^4 M$.

We shall give the silhuette of the black hole for observers located at fixed radius $r_0 = 10^4$M that corresponds to the angular size of $\alpha \sim 1.4$arcsec; for higher distances the angular size falls accordingly to the $1/r_0$ dependence.

First, we give an illustrative picture of the tidal charge influence on the silhuette's properties for maximal inclination angle $\theta_0 = 90°$ when the black hole rotational effects are strongest (Figure 2.12). We present a sequence of silhuettes for fixed black hole spin and varying b (left) and for extreme black holes with $a^2 + b = 1$ and both a, b varying (right). We clearly see that the positive tidal charge squeezes magnitude of the silhuette making its shape more asymmetric, while negative tidal charge enlarges silhuette's diameter symmetrizing its shape when a is fixed. For extreme black holes the silhuette asymmetry is kept but its extension grows with b descending to higher negative values.

Second, there is a crucial effect of the viewing angle θ_0 onto the shape of the black hole silhuette, demonstrated in Figure 2.13 for representative values of b and fixed spin a, and in Figure 2.14 for extreme black holes with parameters $[a^2 = 1; b = 0]$ and $[a^2 = 4; b = -3]$.

The rotational effect on the shape of the silhuette grows with inclination angle growing and becomes strongest when $\theta_0 = \pi/2$; then the suppressing effect of the braneworld parameter is given in the most explicit form as demonstrated in Figure 2.12.

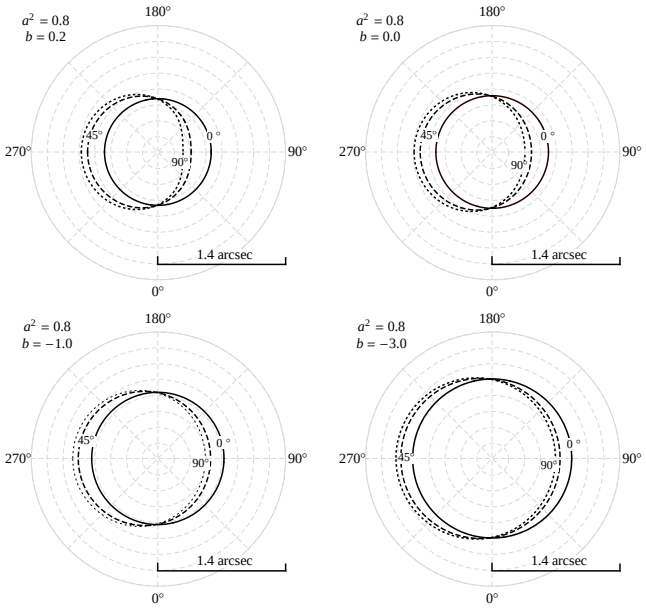

Figure 2.13: *The silhuettes of rotating braneworld black hole on a bright background. Each image contains three black hole shapes for three representative values of observer's inclination angle* $\theta_0 = \{0°(solid), 45°(dashed), 90°(dotted)\}$*, observer's radial coordinate* $r_0 = 10^4 M$ *and the rotational parameter* $a^2 = 0.8$*. Top left image:* $b = 0.2$*. Top right image:* $b = 0.0$*. Bottom left image:* $b = -1.0$*. Bottom right image:* $b = -3.0$*.*

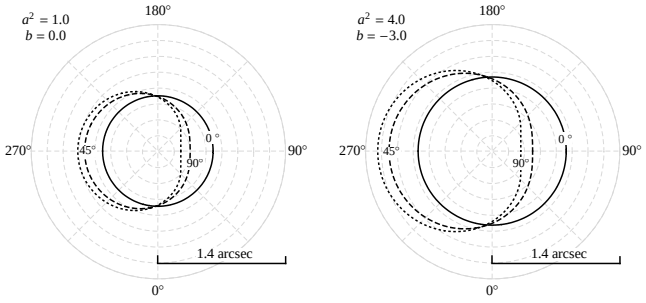

Figure 2.14: *The silhuettes of rotating braneworld black hole on a bright background. Each image contains three black hole shapes for three representative values of observer's inclination angle* $\theta_0 = \{0°(solid), 45°(dashed), 90°(dotted)\}$*, observer's radial coordinate* $r_0 = 10^4 M$*. Silhuettes on the left figure are plotted for extreme black hole with* $a^2 = 1$ *abd* $b = 0$ *and on the right side for the black hole with* $a^2 = 4$ *and* $b = -3$*.*

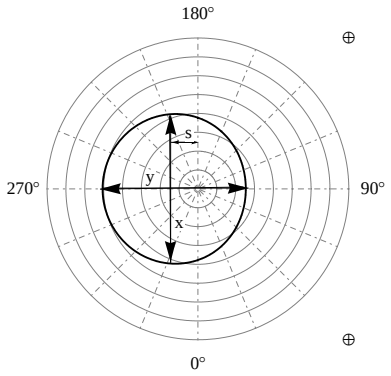

Figure 2.15: *We define shift s and ellipticity $\epsilon = x/y$ as parameters enabling us to characterize the magnitude of distorsion of Kerr black hole silhuette in braneworld universe.*

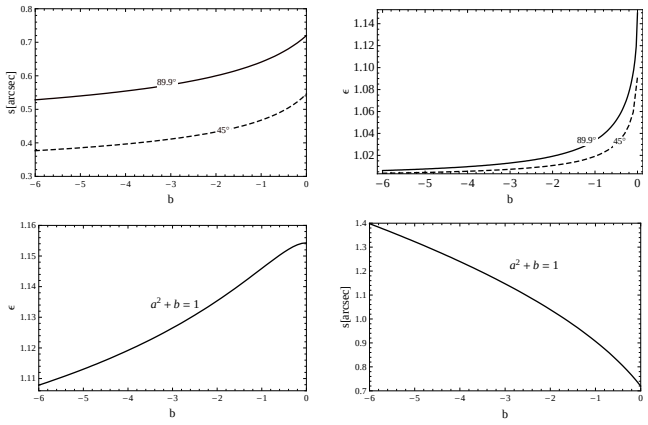

Figure 2.16: *Top row. Left figure: the plot of shift $s = s(b)$ as a function of braneworld parameter b. Right figure: the plot of ellipticity $\epsilon = \epsilon(b)$ as a function of b. There are two curves on each image, one for observer inclination angle $\theta_0 = 45°$ and second for $\theta_0 = 89.9°$. The rotational parameter of black hole is fixed to value $a = 0.9995$ and the radial coordinate of observer if $r_0 = 10^4 M$. Bottom row. The ellipticity ϵ (left) and shift s (right) of the silhuette of the extreme black hole as functions of braneworld parameter b. Observer's coordinates are $\theta_0 = \pi/2$ and $r_0 = 10^4 M$.*

The negative values of the braneworld parameter have the tendency to make the silhuette of a Kerr black hole (with a^2 fixed and for r_0, θ_0 fixed) spherical, suppressing thus the rotational effects. However the symmetrizing effect of the tidal charge could be masked by symmetrizing effect of the

viewing angle θ_0. Therefore it is very important for black hole parameter estimates to have observational limits on the value of θ_0. In order to characterize the influence of the tidal charge on the silhuette of a Kerr black hole we define two quantities in principle measurable by distant observers. The *shift* s of the silhuette

$$s = \tilde{\alpha}(\beta_m)\sin(\beta_m - \pi), \tag{2.118}$$

and its *ellipticity* ϵ

$$\epsilon = \frac{\tilde{\alpha}(\beta = 90^\circ) + \tilde{\alpha}(\beta = 270^\circ)}{2\tilde{\alpha}(\beta_m)\cos(\beta_m - \pi)}, \tag{2.119}$$

where β_m is defined by $\tilde{\alpha}(\beta_m)\sin(\beta_m - \pi) \geq \tilde{\alpha}(\beta)\sin(\beta - \pi), \quad \forall \beta \in [\pi/2, 3/2\pi]$ i.e., it defines maximal extension of the silhuette in the x-direction. The definition of *shift* s and *elipticity* ϵ is illustrated in Figure 2.15.

We calculated shift s and ellipticity ϵ as functions of tidal parameter b for the Kerr black hole with rotational parameter $a^2 = 0.9995$ (see Figure 2.16). Clearly, these are quantities that could be measured and used for a black hole parameters estimates, if observational techniques could be developed to the level enabling the silhuette detailed measuring. We shall discuss such a possibility for the case of the supermassive black hole predicted in the Galaxy Centre (Sgr A^*).

2.6.2 Frequency shift - observer in LNRF

To ilustrate the influence of braneworld parameter on redshift of radiation which is emitted by bright background and detected by observer in LNRF the following set of plots is presented.

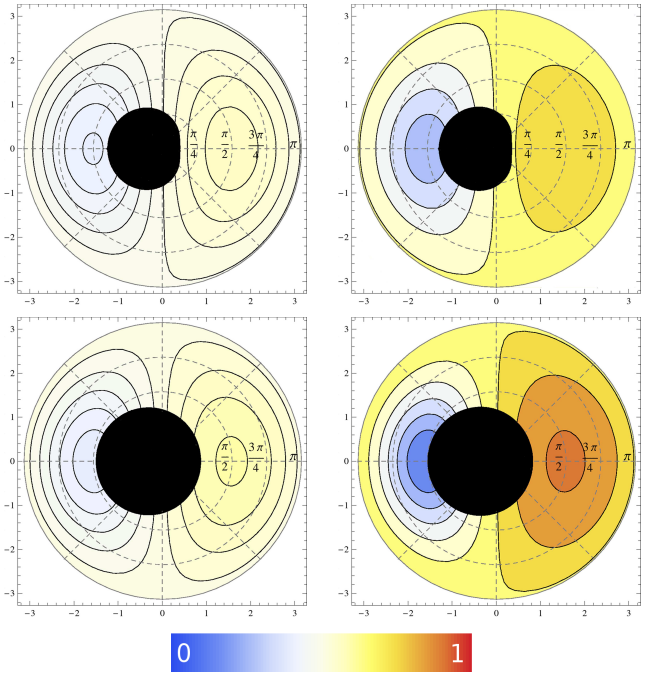

Figure 2.17: *The frequency shift of bright background as seen by observer in LNRF at radial distance* $r_o = 5M$ *from black hole with spin parameter* $a = 0.9981$. *Images in top row are plotted for the braneworld parameter* $b = 0$ *while bottom row images for* $b = -2$. *Left column images have latitude fixed to* $\theta_o = 60°$ *while right column images to* $\theta_o = 90°$. *In order to use one palette of colours for all images, modified frequency shift, given by formula (2.120) is plotted.*

The frequency shift on plots in figure Fig.2.17 is encoded into colors using, of course, one palette for all four images. Therefore modified frequency shift must be defined

$$\tilde{g} = \frac{g_{max} - g}{g_{max} - g_{min}} \tag{2.120}$$

where is $g_{max}(_{min})$ maximal(minimal) value of redshift g from all four images. The darkest blue color refers to $\tilde{g} = 0$ while red color refers to $\tilde{g} = 1$. The result is expectable since with increasing negative value of braneworld parameter b the velocity of LNRF increases.

2.6.3 Spectral line profiles

We have demonstrated the influence of the brany tidal charge on the profilled lines using a computional code developed under all the phenomena discussed above. Both the direct and indirect photons were considered. The profilled lines depend on the black hole parameters a and b, on the radius r_e of the radiating ring and on the inclination angle θ_0 of the observer. We separate the results into two groups according to the sign of the tidal charge; we would like to stress that the results obtained for $b > 0$ are relevant also for radiating rings of uncharged matter orbiting Kerr-Newman black holes with $b \to Q^2$ where Q is the black hole charge parameter.

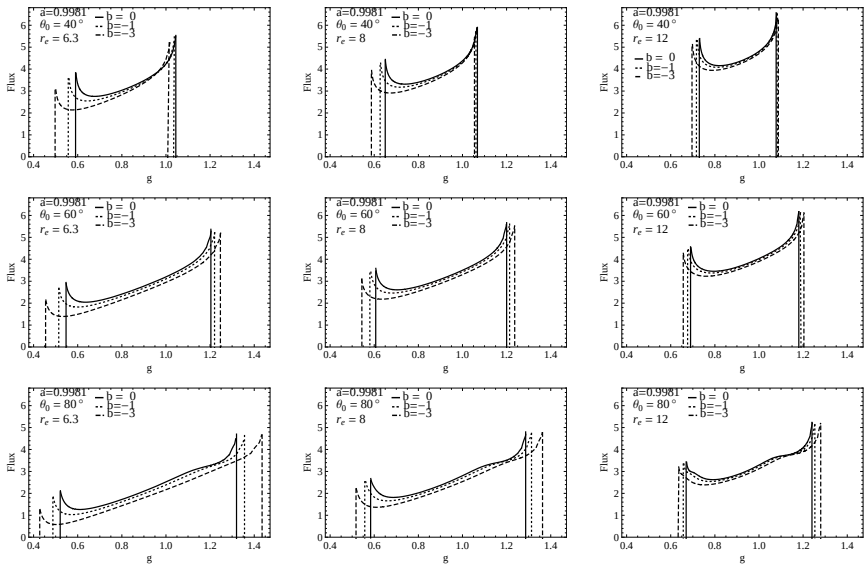

Figure 2.18: *Line profiles for brany black holes with $b < 0$. We demonstrate the influence of inclination angle of observer θ_0, radial distance of emitter r_e and brany parameter b on the profile of spectral line of radiation emitter from radiating keplerian ring. With rotation parameter fixed to $a = 0.9981$ each figure contains three plots for three representative values of brany parameter $b = -3$, -1 and 0. The inclination angle θ_0 and the ring (Boyer - Lindquist) radius r_e are given in the figure.*

- $b < 0$ For negative tidal charges we have fixed the value of the spin parameter to value $a = 0.9981$ close to extreme black hole state ($a = 1$) for Kerr spacetimes ($b = 0$). We then illustrate the influence of the tidal charge $b < 0$ for a relatively large range of its values that all correspond

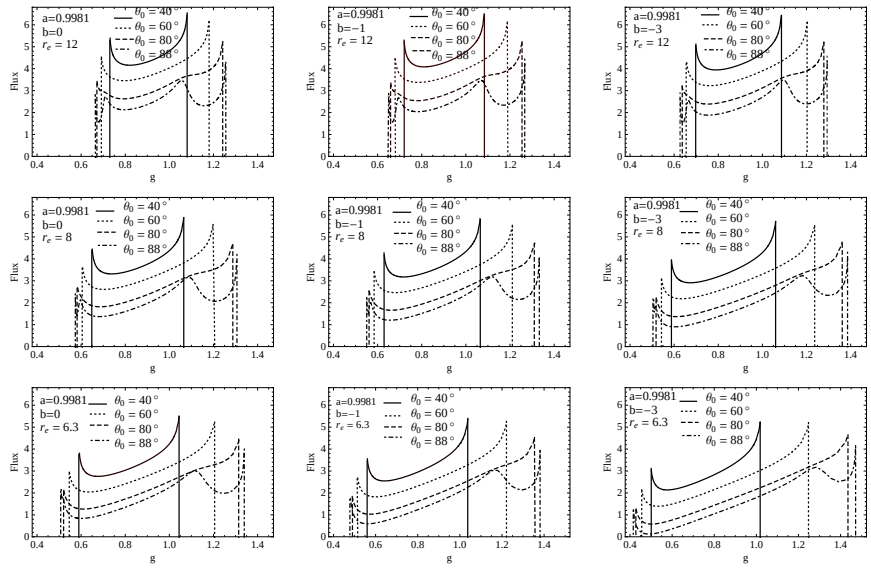

Figure 2.19: *Line profilles for brany black holes with* $b < 0$. *Each figure contain three plots for three representative values of* $\theta_0 = 40°$, $60°$, $80°$ *and* $88°$. *Figures in each row are plotted for fixed value of* $r_e = 12$*(top),* 8*(middle) and* 6.3*(bottom) and brany parameter varying from left figure to right one with values* $b = 0$, -1 *and* -3.

to the black hole spacetimes. The values of the observers inclination angle θ_0 are chosen to represent the cases of small , mediate, extreme and very extreme inclination in order to fully exhibit the strong effect of θ_0 on the line profile. The radius of radiating ring is restricted to the inner part of Keplerian discs. Again, the three values of r_e reflect the optical effects in the innermost part of the disc, the mediate inner part and those where the effects of the tidal charge become to be effectively suppressed. First, the radii are fixed to be the same in all the spacetimes under consideration ($b = 0$, -1, -3), we have chosen $r_e = 6.3M$, $8M$ and $12M$ where the first value ($r_e = 6.3M$) correspond to stable circular of spacetime with brany parameter value being $b = -3$. The results are presented in Fig.2.18. We can see that the influence of the tidal charge is suppressed with growing radius, r_e, as can be intuitively expected because the contributions of b fall with r growing faster than those of the mass and spin parameters of the spacetime and this effect is for each inclination angle θ_0. With r approaching the innermost part of the disc, the profilled lines become to be wider and flatter. These effects are strenghtened for inclination angle growing, as demonstrated

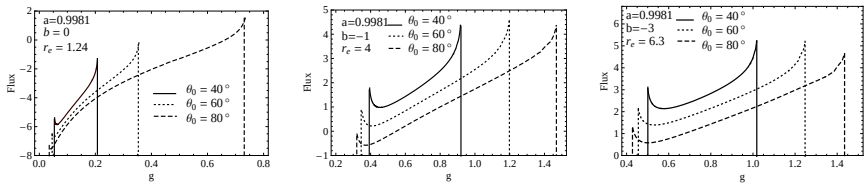

Figure 2.20: *Line profiles for brany black holes with $b < 0$. Each figure contains three plots of profiles of spectral line for three representative values of $\theta_0 = 40°$, $60°$ and $80°$ and fixed(different for each figure) values of ($b = 0$, $r_e = 1.24$)(left), ($b = -1$, $r_e = 4$)(middle) and ($b = -3$, $r_e = 6.3$)(right). The emitters are on orbits close to marginally stable, which is function of brany parameter b, $r_{ms} = r_{ms}(b)$.*

in Fig.2.19. Generally, the profilled lines has two peaks at the red-end and blue-end with the blue-end peak being always higher in comparison with the red one. For fixed $b < 0$, the extension, Δg, of the profilled line grows with θ_0 growoing and r_e falling, while the difference of the profile height at the blue and red end grows with inclination growing. The tidal charge strenghtens these effects while going to higher negative values; for example the frequency shift difference Δg at the radius $r_e = 6.3M$ and the inclination angle $\theta_0 = 80°$ grows with descending b such that $\Delta g(b = 0) = 1.3 - 0.5 = 0.8$, $\Delta g(b = -1) = 1.38 - 0.5 = 0.88$ and $\Delta g(b = -3) = 1.4 - 0.4 = 1.0$.

When the inclination angle reaches extreme values of $\theta_0 > 85°$, the profilled lines in the innermost part of the stable Keplerian orbits are enriched by humps reflecting strong lensing effects caused by traversing the region in close vicinity of the black hole horizon. The two humps appearing in the profile are caused by the fact that we consider both direct and indirect photons as generating the profilled line.

The innermost radius $r_e = 6.3M$ is chosen to correspond to the marginally stable orbit of K-N spacetime with $a = 0.9981$ and $b = -3$. However, for fixed a, but $b = -1(0)$, such a radius is far above the related marginally stable orbit at these spacetimes, since r_{ms}(a=0.9981, b=-1)=4M while $r_{ms}(a = 0.9981, b = 0) = 1.23M$. Therefore, in order to compare the radiating rings orbiting in close vicinity of the marginally stable orbit assumed to be the edge of a Keplerian disc, we give the profilled lines at $r_e = r_{ms}$ in Fig.2.20, for the same inclination angles. Now the effects of the tidal charge are represented in more precise form. Again, the extension of the line Δg grows more strongly with descending b. Of course, we can see that for $b = 0$, the profilled lines

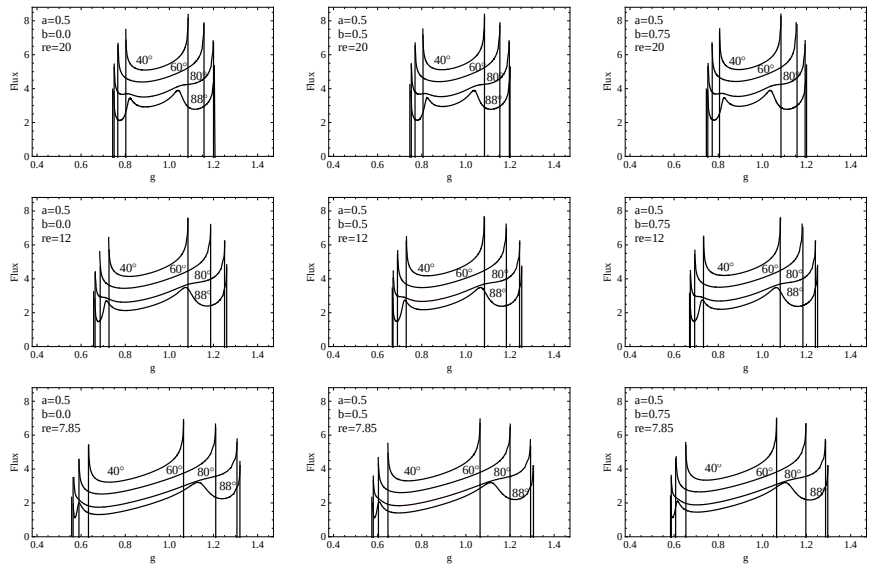

Figure 2.21: *Line profiles for brany black holes with $b > 0$. Each figure contain four plots for four representative values of $\theta_0 = 40°$, $60°$, $80°$ and $88°$. Figures in each row are plotted for fixed value of $r_e = 20$(top), 12(middle) and 7.85(bottom) and brany parameter varying from left figure to right one with values $b = 0$, 0.5 and 0.75.*

are strongly redshifted and suppressed in magnitude, since for $b = 0$ we are dealing with a near extreme spacetime, when the radiating ring is orbiting in extremely deep gravitational potential in close vicinity of the black hole horizon. On the other hand, for $b = -1$ ($b = -3$) the radiating ring is in much higher distance of the horizon and the gravitational field there is not so strong since these black holes (with $a = 0.9981$) are far from the extreme black holes.

The lines profilled by relativistic effects in the innermost part of the accretion disc clearly demonstrate the influence of the tidal charge as shown in Fig.2.20. The lines become flatter, but again the influence of the inclination angle is quite strong, but brings some characteristic features indepedently on the value of b.

- $b >= 0$. Now we discuss the case that could correspond also to modelling of profilled lines in the standard Kerr-Newman spacetimes assuming no electromagnetic interaction of the matter of the radiating ring and the black hole electric charge Q.

  While focusing our attention to the black hole spacetimes, we have to

shift the spin parameter a with changes of the tidal charge b (electric charge Q^2). The results are shown in Fig.2.21 for situations studied for the case of $b < 0$, i.e., in the close vicinity of r_{ms}, in the middle of the innermost part of the disc and in the region where infuence of b starts to be highly suppressed. We can see that for large inclination angles ($\theta_0 \geq 80°$) two humps appear in the line profile, one near the red end of the line, the other close to its blue end.

2.6.4 Images of isoradial geodesics

The influence of tidal charge b on the shape of isoradial geodesics as seen by distant observer are presented on figures Fig.2.22 where direct images of isoradial geodesics are plotted and Fig.2.23 where indirect ones are presented.

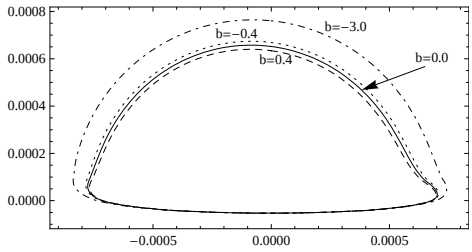

Figure 2.22: Direct *image of the rotating ring in the equatorial plane at* $r_e = 6M$ *around braneworld Kerr black hole with rotational parameter* $a^2 = 0.5$ *for four representative values of tidal charge parameter* $b = -3.0$, $b = -0.4$, $b = 0.0$ *and* $b = 0.4$. *The observer is located at* $r_0 = 10^4 M$ *and* $\theta_0 = 85°$.

One immediatelly see that the scale of images for more negative value of braneworld parameter b is bigger than in the case of less negative values of b. It is expected result since it has been shown in previous sections that the scales of characteristic radii (photon orbit radii, horizon) with more negative values of b are bigger.

2.6.5 Disc images

It is very important to demostrate the influence of the braneworld parameter on the shape of images of rings in the equatorial plane representing parts of Keplerian accretion discs. Of course, as well known from the Kerr (and even Schwarzchild) black holes, the images strongly depend on the latitude of the observer. We calculate the direct and indirect images of flat discs and

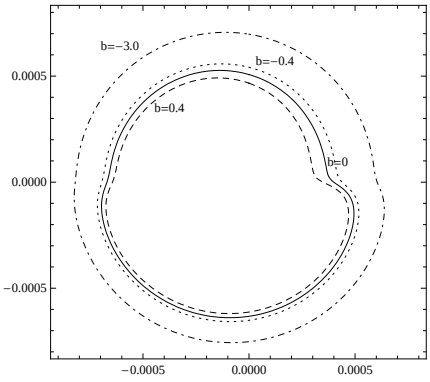

Figure 2.23: Indirect *image of the rotating ring in the equatorial plane at* $r_e = 6M$ *around braneworld Kerr black hole with rotational parameter* $a^2 = 0.5$ *for four representative values of tidal charge parameter* $b = -3.0$, $b = -0.4$, $b = 0.0$ *and* $b = 0.4$. *The observer is located at* $r_0 = 10^4 M$ *and* $\theta_0 = 85°$.

combined, full image of the disc for two representative values of viewing angle θ_0 and appropriatelly chosen extension of radiating disc area.

We include the effect of frequency shift into the calculated images of part of the Keplerian discs assumed to be radiating at a given fixed frequency.

The frequency shift of radiation emitted from Keplerian ring including all relativistic effects is given by equation (2.80). Quantitu g depends on impact parameter λ and is independent of the second photon motion constant (impact parameter) q. Of course, depending on the position of the emitter along the circular orbit, the impact parameters λ, q of photons reaching a fixed distant observer will vary periodically (see eg., [21]). For each position of the emitter the impact parameters are determined by the procedure of integration of photon trajectories.

The influence of the frequency shift in the disc images is demonstrated in Figures 2.24 and 2.25. The role of the braneworld parameter is illustrated both for small ($\theta_0 = 30°$) and high ($\theta_0 = 80°$) inclination angles. We consider two cases of the radiating disc extension: first one with fixed inner and outer radii, independent of the black hole parameters, and the second one when the inner radius is identified with the marginally stable orbits, depending on the black hole parameters.

In order to map the frequency shift g into color palete we define modified frequency shift $\bar{g} = (g - g_{min})/(g_{max} - g_{min})$ where g_{min} (g_{max}) is the minimal (maximal) value of frequency shift, which is fixed in a particular set of images.

We can see from Figs. 2.24 and 2.25 that the negative tidal charge has the tendency to enlarge and symmetrize the disc images.

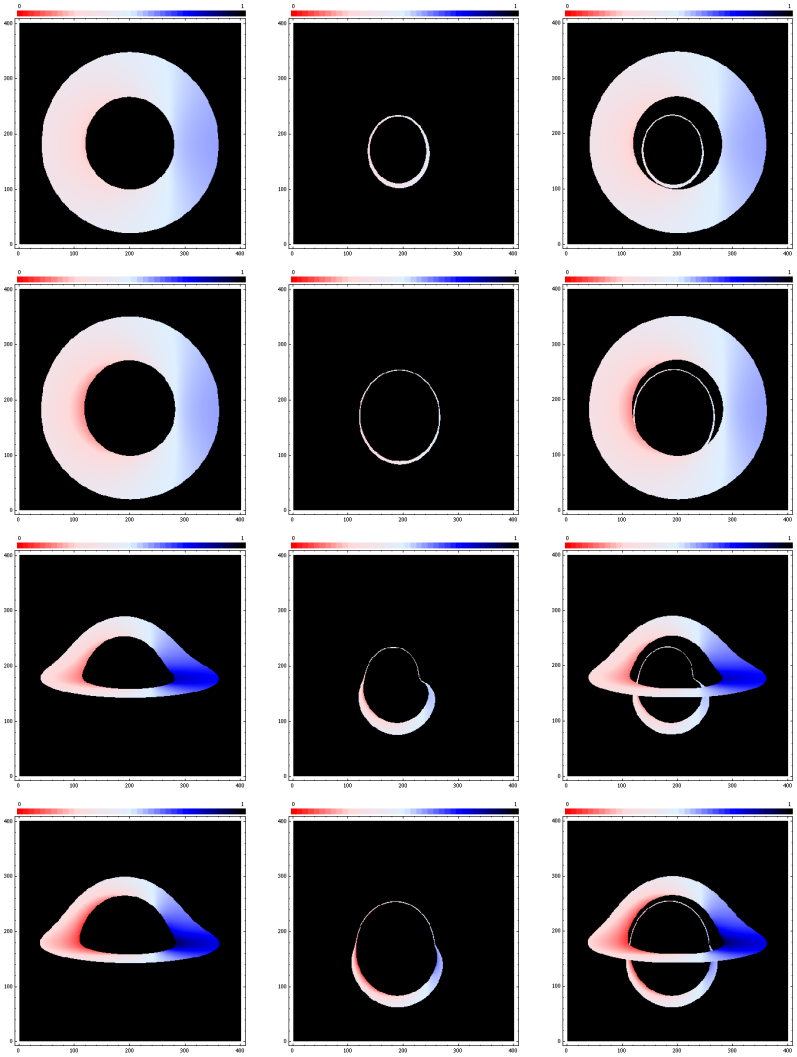

Figure 2.24: *Radiating Keplerian disc images with fixed inner and outer radii. The modified frequency shift* $\bar{g} = (g - g_{min})/(g_{max} - g_{min})$*, with* $g_{min} = 0.4$ *and* $g_{max} = 1.5$*, of the radiation emitted from the thin disk with inner radius* $r_{in} = 7M$ *and outer radius* $r_{out} = 15M$*, encoded into colors is plotted for representative values of tidal charge parameter* $b = -3.0, 0.0$ *and inclination of observer* $\theta_0 = 30°$*,* $80°$*. In the left column direct images are ploted, the indirect images are ploted in the central column and the composition of direct and indirect images is plotted in the right column. The first two rows of images are plotted for the observer inclination* $\theta_0 = 30°$ *and the second two rows of images are plotted for the observer inclination* $\theta_0 = 80°$*. Top row images are plotted for* $b = 0.0$*, the second row images are plotted for* $b = -3.0$*, the third row images are plotted for* $b = 0.0$ *and bottom row images are plotted for* $b = -3.0$*.*

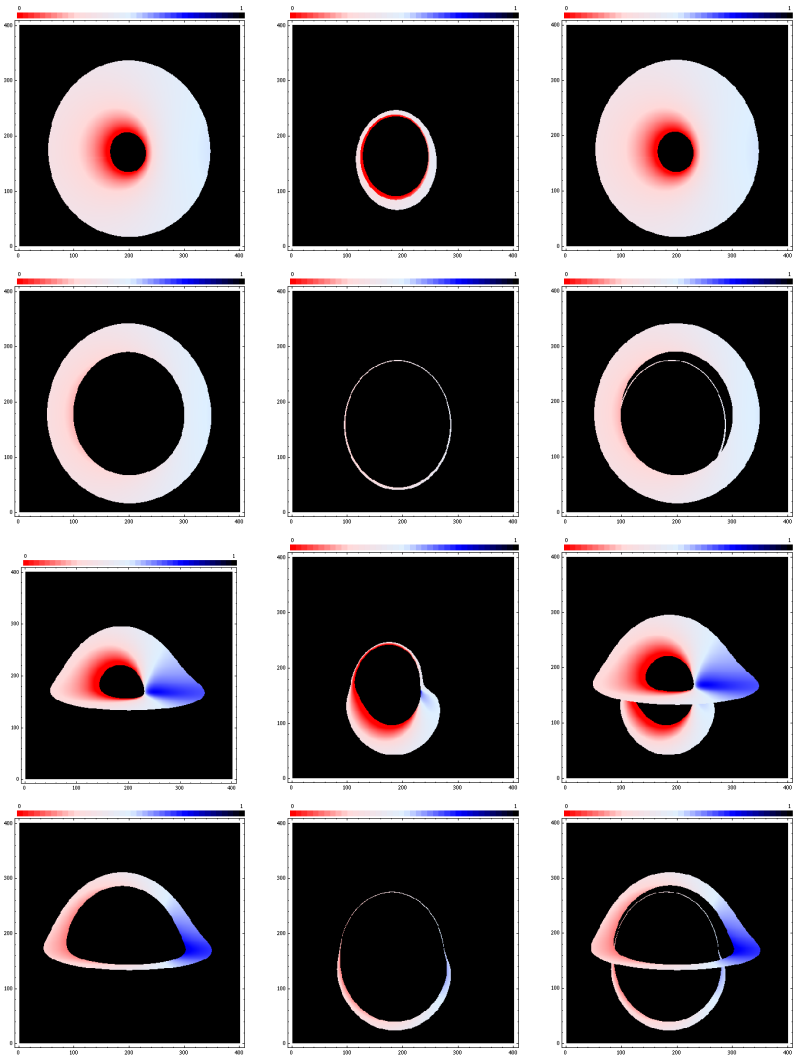

Figure 2.25: *Radiating Keplerian disc images with* $r_{in} = r_{ms}$. *The modified frequency shift* $\bar{g} = (g - g_{min})/(g_{max} - g_{min})$, *with* $g_{min} = 0.2$ *and* $g_{max} = 1.8$, *of the radiation emitted from the thin disk with inner radius* $r_{in} = r_{ms}$ *(with* $r_{ms}(b = 0; a = 0.9981) = 1.3$ *and* $r_{ms}(b = -3; a = 0.9981) = 6.3$*) and outer radius* $r_{out} = 10$, *encoded into colors is plotted for representative values of tidal charge parameter* $b = -3.0,\ 0.0$ *and inclination of observer* $\theta_0 = 30°,\ 80°$. *In the left column direct images are ploted, the indirect images are ploted in the central column and the composition of direct and indirect images is plotted in the right column. The first two rows of images are plotted for the observer inclination* $\theta_0 = 30°$ *and the second two rows of images are plotted for the observer inclination* $\theta_0 = 80°$. *Top row images are plotted for* $b = 0.0$, *the second row images are plotted for* $b = -3.0$, *the third row images are plotted for* $b = 0.0$ *and bottom row images are plotted for* $b = -3.0$.

2.6.6 Time delay

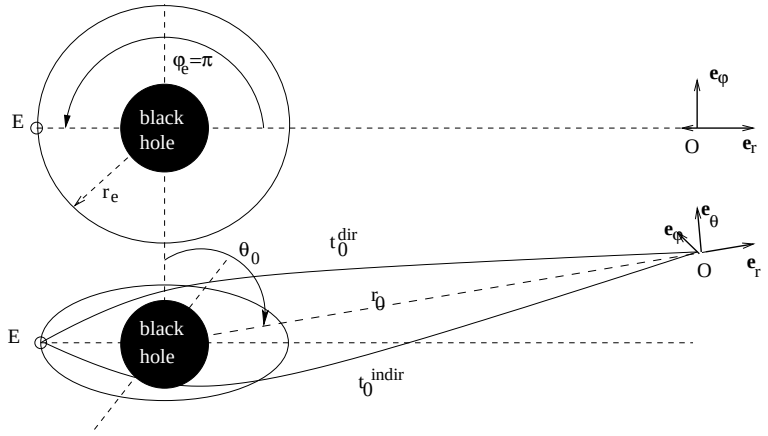

Figure 2.26: *The illustration of the impact of tidal charge parameter on the time delay Δt in case of direct and indirect photons emitted from emitter E at coordinate time t_e and azimuthal position $\varphi_e = \pi$. They are received at observer O at coordinate times $t_o^{\rm dir}$ ($t_o^{\rm indir}$ resp.). The emittor is on circular geodesic in equatorial plane of braneworld Kerr black hole at radial coordinate $r = r_e$. The observer is far from the center of the black hole at $r = r_o$. Its inclination is $\theta = \theta_o$.*

To demonstrate the impact of the tidal charge b on the time delay we consider the following situation (see Figure 2.26). Let the isotropicaly radiating monochromatic source orbits in the equatorial plane of the braneworld Kerr black hole at radial distance r_e. It can be switched on and off. When it reaches the azimuthal coordinate $\varphi = \pi$ it is switched on and we compare the coordinate times $t_o^{\rm dir}$ and $t_o^{\rm indir}$ of reception of the photons from the direct and indirect images of the source.

The results are demonstrated in the Figure 2.27. We can directly see that time delay Δt between times of reception of the direct and indirect photons emitted at the same instant from the azimuthal position $\varphi = \pi$ increases as the value of the tidal charge parameter b goes to higher negative values. When b is fixed, the time delay Δt increases as the value of the inclination decreases. The same effects appear for other positions of the radiating spot ($\varphi \neq \pi$). We can see that the time delay Δt depends strongly on the viewing angle θ_0. Therefore, it is extremely important to have a system with precisely determined viewing angle.

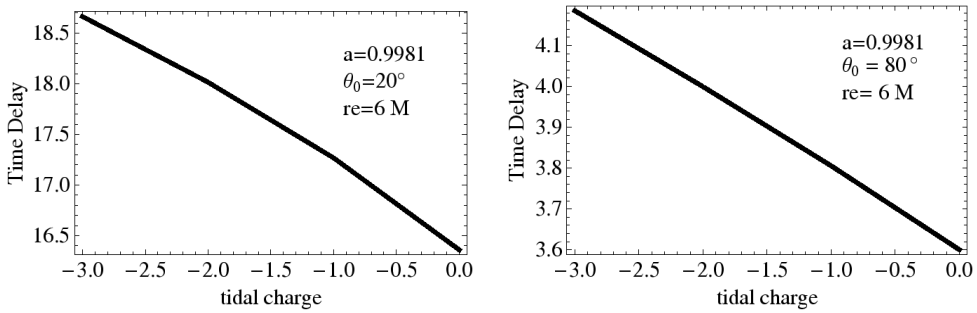

Figure 2.27: *The difference ("Time Delay"), $\Delta t = t_o^{\rm indir} - t_o^{\rm dir}$, between coordinate times of reception of direct and indirect geodesics of photons emmited at the same coordinate time t_e from the azimuthal coordinate $\varphi = \pi$ is plotted as a function of tidal charge b. Left figure: the inclination of the observer is $\theta_0 = 20°$. Right figure: the inclination of the observer is $\theta_0 = 80°$.*

2.6.7 Optical phenomena related to Sgr A^*

There is an enormously growing evidence that the center of our Galaxy harbors a supermassive black hole whose position could be almost surely identified with the extremely compact radio source Sgr A^*. The chain of arguments seems to be very convincing; stars orbiting an unseen mass concentration on elliptical orbits with a common focal position, the unseen mass centered on Sgr A^* that seems to be motionless at the dynamical center of the Galaxy, extremely compact emission of the center [49]. Recent measurements of Ghez and collaborators [36] from the W.M. Keck 10 - meter telescopes of a fully unconstrained Keplerian orbit of the short period star SO-2 provide the distance $R_0 = 8.0 \pm 0.6$ kpc and black hole mass $M = (4.1 \pm 0.6) \times 10^6 M_\odot$. If the black hole is assumed to be at rest with respect to the Milky Way Galaxy (i.e., has no massive companion to induce its motion) as argued by Reid [49], the fit can be further constrained to $R_0 = 8.4 \pm 0.4$kpc and $M = (4.5 \pm 0.4) \times 10^6 M_\odot$ [36].

Such a close and huge supermassive black hole could be clearly a very convenient object, probably the best one, for testing a wide variety of optical phenomena in strong gravity in its vicinity. The time delay of accidents happening behind the black hole and observed along two directions could be in principle easily measured. We could even expect possibility of black hole silhuette measurements. In this way the influence of the tidal charge could be properly tested and its value estimated, because for the Galaxy supermassive black hole we can determine relatively precisely the inclination angle of the observer (Solar system), although it is of course very close to $\theta_0 \simeq 90°$.

For non-rotating , Schwarzchild black holes, the silhuette diameter is given by the impact parameter of the photon circular orbit

$$D = 2\lambda_{ph} = 6\sqrt{3}M. \tag{2.121}$$

Using the Sgr A^* mass estimate $M \sim 4.5 \times 10^6 M_\odot$, we find $D \simeq 55\mu$arcsec while interferometer finges were reported at wavelength of 1.3 mm and fringe spacing of 0.00005, comparable with the expected value of D. Shorter wavelengths should enable detailed measurements of the black hole silhuette and relatively precise estimates of the black hole parameters due to very precise knowledge of the inclination angle. The angle can be given by the measurement of the Solar system position relative to Galaxy plane $z_\odot \sim 14pc$[64]. Then $\theta_0 \sim 89.9°$ or more precisely, θ_0 lies between the values of $89.8772°$ ($z_\odot = 18pc$) and $89.9318°$($z_\odot = 10pc$). Of course, considering the silhuette shape, it is quite enough to take $\theta_0 = 90°$.

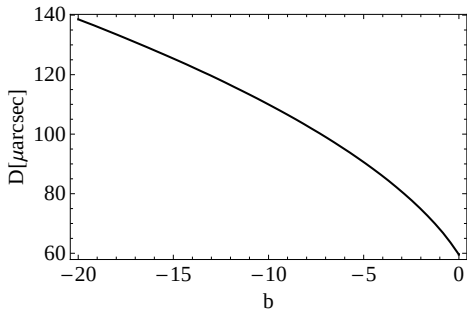

Figure 2.28: *Diameter D as a function of braneworld parameter b is plotted for Schwarzchild black hole of mass $M = 4.5 \times 10^6 M_\odot$. Observer is at $r_0 = 8.4kpc$ lying in the equatorial plane.*

In the case of spherically symmetric black holes, the influence of the tidal charge parameter b on the silhuette diameter can be given by the simple formula for impact parameter of photon circular orbits that reads [59]

$$\lambda_{ph}(b) = \frac{r_{ph}^2}{\sqrt{r_{ph} - b}} M, \tag{2.122}$$

where

$$r_{ph}(b) = \frac{3}{2}\left(1 + \sqrt{1 - \frac{8b}{9}}\right). \tag{2.123}$$

The resulting dependence of the diameter $D(b)$ is illustrated in Figure 2.28. The diameter grows slowly with the descending of b; notice that its magnitude is twice the pure Schwarzchild value for $b = -12.8428$. Of course, for rotating black holes the silhuette is maximally deformed due to the influence of rotation since the viewing angle $\theta_0 \sim 90°$ and is given by calculations and results presented above. Testing of the combined spin and tidal charge influence would be possible with measurement precision enlarged for 1 order relative to the recently expected state mentioned above. Clearly, we can expect that the observational accuracy in near future will be high enough to measure the Sgr A^* black hole silhuette implying relevant estimates of the black hole parameters.

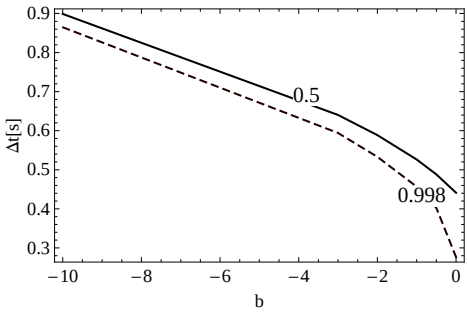

Figure 2.29: *Comparizon of time delay effect as a function of braneworld parameter b between two rotating black holes with rotational parametes* $a = 0.5$ *and* $a = 0.998$. *For each b the emitter is radiating from marginally stable orbit. The relevant values of radii* r_{ms} *of marginally stable orbits are arranged in the Table 2.6.*

Table 2.6: *Table of relevant values of* r_{ms} *used in plots oin Fig 2.29*

b	0.0	-0.5	-1.0	-2.0	-3.0	-10.0
$r_{ms}(a = 0.5)$	4.24M	5.05M	5.73M	6.88M	7.85M	12.88M
$r_{ms}(a = 0.998)$	1.24M	3.03M	3.91M	5.22M	6.28M	11.44M

Considering the time delay effects, the exact value of θ_0 is crucial since it plays a fundamental role in determining the time delay effect whose scale is given by the value of $t \sim 1sec$. We illustrate the influence of the tidal charge on the time delay effects at the astrophysically important radii corresponding

to marginally stable circular geodesics, i.e. in the strong gravity regime, for two representative fixed values of black hole spin (see Figure 2.29 and Table 2.6). We can expect importance of the regions close to r_{ms} for relevant optical effects due to the idea of the low angular momentum accretion in Sgr A^* advocated by B. Czerny [27]. Clearly, we can see in Figure 2.29 that the time delay effects could be well measurable and the tidal charge influence could be well tested, if the black hole spin is properly estimated.

Conclusions

One of the most promising ways of estimating influence of hypothetical hidden external dimensions, considered in the framework of the braneworld model with infinite external dimension as developed by [47], seems to be investigation of the optical phenomena caused by the black hole backgrounds. It is so because black holes represent the only case when the non-local influence of the bulk space on the braneworld spacetime structure can be fully described by a single, braneworld parameter called tidal charge, the sign of which can be both positive and negative, with the second possibility beeing more realistic one [17, 28].

Here, we focused our attention to developing a theoretical background for treating the optical phenomena in vicinity of braneworld rotating black holes and bringing general tendencies of the tidal charge effect in some basical optical phenomena.

We have shown qualitatively how the braneworld tidal charge affects the basical optical phenomena, especially the black-hole silhuette, the accretion disc image with the frequency shift of area of the disc radiating at a specific frequency, and the time delay between the direct and indirect images of the hot spot orbiting the black hole. We have shown that these phenomena could be measured and used to put limits on the tidal charge in case of Galaxy Center Sgr A^* supermassive black hole.

We generalized the approaches based on the transfer-function method as introduced and developed in Schwarzchild and Kerr backgrounds [32, 43, 21, 57, 41, 30, 33, 48] where equations of photon motion are solved in terms of the elliptic integrals (see [48, 39, 40]). For purposes of the present work, the transfer-function method seems to be most efficient. Nevertheless, we prepared the ray-tracing method too, since that could be usefull in treating other optical phenomena.

Generally, rising negative value of the tidal charge strenghtens the black hole field and suppresses the rotational phenomena, when the black-hole rotation parameter is fixed. The magnitude of the optical phenomena grows

with decreasing of the negatively-valued tidal charge, but the rotation induced asymmetry of the phenomena like the black-hole silhuette, or the accretion disc image, decreases. The black-hole silhuette is characterized by two parameters, namely the shift of the center and ellipticity, that could be in principle measurable in the Galactic Center black-hole system Sgr A^*, after expected development of observational techniques that at present enable measurement of the black hole diameter, not details of the shape. The Galaxy center (Sgr A^*) seems to be also a promising candidate for testing the time delay effects both for phenomena related to the accretion disc and flares observed there , and for some expected lensing phenomena connected to the observed stars orbiting the Sgr A^* central black hole.

We have found that observable phenomena could be expected for the time-delay effects. Of special interest is comparison of time delays generated for sources in vicinity of the Sgr A^* black hole (both stars and disc hot spots) and those related to weak lensing of some distant sources [65].

Similarly, keeping rotational parameter fixed, the negative tidal charge has tendency to make the isoradial curve images (both direct and indirect) larger and less deformed while the positive tidal charge influence is of opposite character. On the other hand, for fixed rotational parameter of the black hole and disc radiating at the innermost part above the innermost stable orbit at $r = r_{ms}$, the negative tidal charge restricts the radiating ring image simply because the radius r_{ms} grows with decreasing value of braneworld parameter b. Suppresion of the relativistic effects can be measurable also in the spectral line profiles generated by the inner hot part of the disc radiating at special X-ray line [51].

The optical tests have to be confronted with the data obtained from quasiperiodic oscillations observed in some black-hole systems (microquasars [50]). The orbital resonance model gives good estimates of the black-hole parameters [63, 61, 62]; this model has been recently generalized to the case of braneworld Kerr black holes [60]. It is shown that in the case of microquasar GRS 1915+105 and Galactic Center Sgr A^* black holes with the negative braneworld parameter b are allowed by the observational data [60]. If the rotating black hole is near-extreme, the extended resonance model could give some other relevant restrictions [74, 75]. Detailed modelling of optical phenomena connected to the oscillating discs or orbiting (oscillating) hot spots and related resonant phenomena between the oscillation modes could be very promising in putting limits on allowed values of the tidal charge of the black hole. We plan to elaborate such modelling in future.

Chapter 3

Rees-Sciama effect

Temperature fluctuations of the Cosmic Microwave Background Radiation (CMBR), recently measured by COBE, WMAP, etc., are observed on the level of $\Delta T/T \sim 10^{-5}$ [1]. These fluctuations can be explained in two ways. First, by the Sachs–Wolfe effect [2], i.e., as an imprint of energy density fluctuations related to the CMBR temperature fluctuations at the cosmological redshift $z \sim 1300$ during the era of recombination, when effective interaction of matter and CMBR is ceased [3]. Second, by the Rees–Sciama effect [4], i.e., as a result of influence of large-scale inhomogeneities (large galaxies or their clusters, and large voids) evolved in the expanding universe due to the gravitational instability of matter at the era characterised by $z \sim 10$. In the case of spherically symmetric clusters and voids, the Rees–Sciama effect was considered in detail by Mészáros and Molnár [6, 5]. They describe the clusters by the standard Einstein–Strauss vakuola model, while the voids they model in an approximative way that does not meet the full general-relativistic junction conditions. Further, they do not consider the effect of refraction of light at the boundary surface matching the cluster (void) with the expanding universe. However, this effect could be of great importance in an accelerating universe, indicated by many of recent cosmological tests predicting present value of the vacuum energy density $\rho_{\rm vac} \sim 0.7\rho_{\rm crit}$ ($\rho_{\rm crit} \equiv 3H/8\pi G$ is the critical energy density corresponding to the flat universe predicted by the inflationary paradigm [7, 1]). The vacuum energy density (or energy of a quintessence field) is related to the (effective) cosmological constant by

$$\Lambda = \frac{8\pi G}{c^2}\rho_{\rm vac}. \tag{3.1}$$

Here, we present a study of the influence of the relict repulsive cosmological constant, indicated by observations to be equal $\Lambda \approx 10^{-56}\,{\rm cm}^{-2}$, on the Rees–Sciama effect. We use the Einstein–Strauss–de Sitter (ESdS) vakuola

model in which the inhomogeneity is represented by a spherically symmetric cluster immersed into the Friedmanian dust-filled universe (see Fig. 3.1). We determine temperature fluctuations of the CMBR passing the vakuola described by the ESdS model and give estimations of the relevance of the effect of refraction at the matching surface.

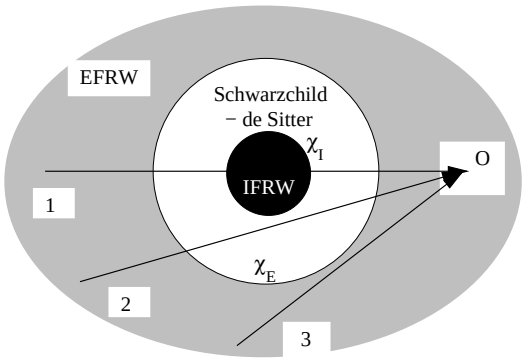

Figure 3.1: ESdS vakuola model. A schematic picture of a cluster represented as a sphericaly symmetric inhomogeneity immersed in the dust filled Friedman universe. The observer O receives two photons coming through the vakuola, and third one coming directly.

We use the geometric units with $c = G = 1$.

3.1 Geodesics intersecting the matching hypersurface

In the framework of the Einstein–Strauss–de Sitter model the behaviour of geodesics crossing the MH is crucial. At the MH the relation between the directional angle as measured by the comoving Friedman observers, ψ_{F}, and the directional angle as measured by the Schwarzchild–de Sitter static observers,ψ_{S}, must be determined. The segments of the geodesics in the FRW and the SdS geometry must be smoothly connected on the MH. One must look for the Lorentz transformation relating the comoving Friedman and the static SdS observers on the MH.

In the RW metric, the geodesic equations are given by expressions (1.24) – (1.27) [9] and geodesic equations in the SdS spacetime are given by the formulae (1.12) – (1.15) .

Let us consider coordinate systems with coincidentally oriented coordinate axes, moving mutually in the direction of the radial axis. The orthonor-

mal base vectors are related by the standard Lorentz transformation

$$\mathbf{e}_{(\mu')} = \Lambda_{\mu'}{}^{\nu}\mathbf{e}_{(\nu)} \tag{3.2}$$

with the Lorentz matrix

$$\Lambda_{\mu'}{}^{\nu} = \begin{pmatrix} \cosh\alpha & \sinh\alpha & 0 & 0 \\ \sinh\alpha & \cosh\alpha & 0 & 0 \\ 0 & 0 & 1 & 0 \\ 0 & 0 & 0 & 1 \end{pmatrix}. \tag{3.3}$$

The orthonormal basis of the static SdS observers is given by the relations

$$\mathbf{e}_{(t)} = \mathcal{A}^{-1}(r)\frac{\partial}{\partial t}, \quad \mathbf{e}_{(r)} = \mathcal{A}(r)\frac{\partial}{\partial r}, \tag{3.4}$$

$$\mathbf{e}_{(\theta)} = r^{-1}\frac{\partial}{\partial\theta}, \quad \mathbf{e}_{(\phi)} = (r\sin\theta)^{-1}\frac{\partial}{\partial\phi}, \tag{3.5}$$

while in the case of the comoving FRW observers it is given by

$$\mathbf{e}_{(T)} = \frac{\partial}{\partial T}, \quad \mathbf{e}_{(\chi)} = R^{-1}\frac{\partial}{\partial\chi}, \tag{3.6}$$

$$\mathbf{e}_{(\theta)} = (R\Sigma_k)^{-1}\frac{\partial}{\partial\theta}, \quad \mathbf{e}_{(\phi)} = (R\Sigma_k\sin\theta)^{-1}\frac{\partial}{\partial\phi}. \tag{3.7}$$

We obtain the parameter of the Lorentz transformation from the fact that the 4-velocity of the test particles comoving with the MH can be expressed in the FRW and SdS spacetimes by the relation

$$\mathbf{u}_{(\mathrm{b})} = \frac{\partial}{\partial T} = \mathbf{e}_T = \mathcal{A}^{-1}(r_\mathrm{b})\mathcal{E}_\mathrm{b}\mathbf{e}_t + \left[\mathcal{E}_\mathrm{b}^2 - \mathcal{A}^2(r_\mathrm{b})\right]^{1/2}\mathcal{A}^{-1}(r_\mathrm{b})\mathbf{e}_r. \tag{3.8}$$

Therefore, we arrive at the Lorentz transformation parameter in the form

$$\cosh\alpha = \Lambda_T{}^t = \Lambda_\chi{}^r = \mathcal{E}_\mathrm{b}\mathcal{A}^{-1}(r_\mathrm{b}) = \sqrt{1-\frac{2kM}{\tilde{R}}}\left(1-\frac{2M}{r_\mathrm{b}}-\frac{\Lambda r_\mathrm{b}^2}{3}\right)^{-1/2}. \tag{3.9}$$

The velocity parameter of the Lorentz shift, giving the speed of the expansion of the MH as measured by the static SdS observers, and the Lorentz factor are then given by the relations

$$V(r_\mathrm{b}) = \sqrt{1-\frac{\mathcal{A}^2(r_\mathrm{b})}{\mathcal{E}_\mathrm{b}^2}}, \quad \gamma = \cosh\alpha = \left[1-V(r_\mathrm{b})^2\right]^{-1/2}. \tag{3.10}$$

3.1.1 Refraction of light at the matching hypersurface

Denoting the directional angles (related to the outward radial direction defined for observers at the radius, where the MH is located momentarily) of a photon entering (leaving) the FRW universe from (into) the SdS vakuola as $\psi_{\rm F}^{+}$, $\psi_{\rm S}^{+}$ ($\psi_{\rm F}^{-}$, $\psi_{\rm S}^{-}$), we arrive at the formulae

$$\cos\psi_{\rm F}^{\pm}=\frac{\cos\psi_{\rm S}^{\pm}\mp V_r}{1\mp V_r\cos\psi_{\rm S}^{\pm}},\qquad \sin\psi_{\rm F}^{\pm}=\frac{\sin\psi_{\rm S}^{\pm}\sqrt{1-V_r^2}}{1\mp V_r\cos\psi_{\rm S}^{\pm}}. \tag{3.11}$$

For photons entering the FRW universe from the SdS spacetime, the detailed analysis [15] shows that

$$\psi_{\rm F}^{+}>\psi_{\rm S}^{+}\quad\text{for}\quad\psi_{\rm S}^{+}\in[0,\pi/2], \tag{3.12}$$

i.e., for such photons the refraction angle is always larger than the impact angle. The total reflection occurs for angles

$$\psi_{\rm S}^{+}>\psi_{\rm S(T)}^{+}\equiv\arccos V_r. \tag{3.13}$$

In Table 3.1, we give the critical angles of the total refraction $\psi_{\rm S(T)}^{+}$ for some values of the MH expansion velocity. In Fig. 3.2a, we present the dependence $\psi_{\rm F}^{+}=\psi_{\rm F}^{+}(\psi_{\rm S}^{+};V_r)$ for some appropriately chosen values of the expansion velocity.

Table 3.1: Total reflection angle $\psi_{\rm S(T)}^{+}$, calculated for four different values of the speed parameter V_r.

V_r	0.1	0.3	0.7	0.9
$\psi_{\rm S(T)}^{+}$	$84°15'$	$72°32'$	$45°34'$	$25°50'$

Considering photons entering the SdS region from FRW universe, we can conclude that $\psi_{\rm S}^{-}>\psi_{\rm F}^{-}$ for $\psi_{\rm F}^{-}\in[0,\pi/2]$, i.e., the refraction angle is again always larger then the impact angle, and the total reflection occurs for

$$\psi_{\rm F}^{-}>\psi_{\rm F(T)}^{-}\equiv\arccos V_r. \tag{3.14}$$

3.1.2 Expansion velocity of the matching hypersurface

We shall consider the simplest case of the MH expansion velocity for the spatially flat universe ($k=0$):

$$V_r=\sqrt{\frac{2M}{r_{\rm b}}+\frac{\Lambda r_{\rm b}^2}{3}}. \tag{3.15}$$

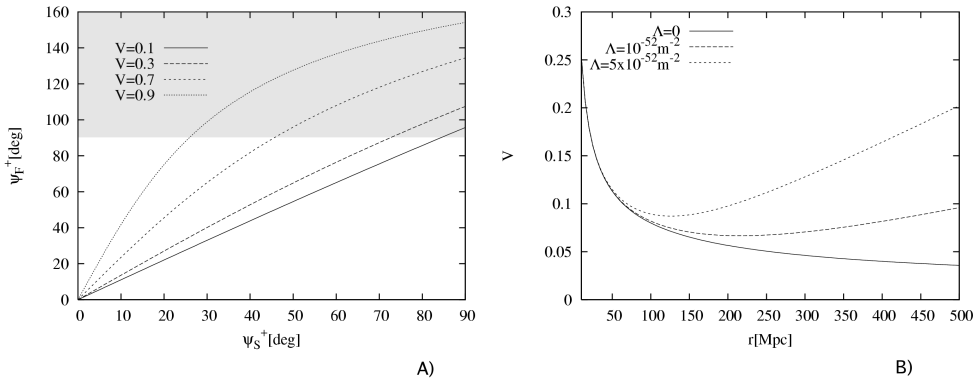

Figure 3.2: Plot A: The refraction angle ψ_F^+ for fixed speed parameter V, as a function of the impact angle ψ_S^+ from the interval $[0, \pi/2]$. The shaded area corresponds to the total reflection of the light. Plot B: The dependence $V_r = V_r(r_\mathrm{b})$ for fixed mass $M = 7{\cdot}10^{18} M_\odot$ of vakuola and three representative values of $\Lambda = 0$, $10^{-52}m^{-2}$ and $5 \cdot 10^{-52}m^{-2}$ and vakuola radius r_b from the interval $[10Mpc, 500Mpc]$. The function $V(r_\mathrm{b})$ reaches its local minimum as it approaches the static radius r_s.

Introducing a dimensionless cosmological parameter $y \equiv \frac{1}{3}\Lambda M^2$, we find the local extremum of $V_r(r_\mathrm{b})$ ($\mathrm{d}V_r/\mathrm{d}r_\mathrm{b} = 0$) located at so called static radius of the SdS spacetime

$$\frac{r_\mathrm{s}}{M} \equiv y^{-1/3}, \tag{3.16}$$

where the gravitational attraction of the central mass condensation (or a black hole) is just balanced by the cosmic repulsion [12, 10, 11]. We can see that with r_b growing $V_r(r_\mathrm{b})$ falls down for $r_\mathrm{b} < r_\mathrm{s}$, it reaches its minimum at the static radius ($r_\mathrm{b} = r_\mathrm{s}$), where

$$V_{\mathrm{r(min)}} = V_r(r_\mathrm{b} = r_\mathrm{s}) = \frac{3M}{r_\mathrm{s}} = 3y^{1/3}, \tag{3.17}$$

while the expansion speed is accelerated at $r_\mathrm{b} > r_\mathrm{s}$, approaching velocity of light ($V_r \to 1$) when r_b approaches the cosmological horizon of the SdS region ($r_\mathrm{b} \to r_\mathrm{c}$) (see Fig.3.2b). Notice that for $y \ll 1$, the cosmological horizon is approximately given by

$$\frac{r_\mathrm{c}}{M} \sim y^{1/2}. \tag{3.18}$$

For the exact formulae giving loci of the event horizons r_c and r_h in the SdS spacetimes see [12].

3.2 Influence of the refraction effect on temperature fluctuations of the CMBR

We shall study the influence of the refraction effect on the CMBR in the framework of the ESdS model using the simplified approach developed by Mészáros and Molnár (for more detailed model, considering also deflection of light by the mass condensation, see [14]). We do not consider the model of void used in [6], since it is not self-consistent from the point of view of general relativity. It was shown in [6] that the temperature fluctuations are fully determined by the length of the photon ray spanned in the vakuola region, i.e., it is determined by the angle $\psi_{\rm S}$ giving the impact angle of photon on the MH. The effect of refraction can be incorporated into the model by substituting the angle $\psi_{\rm S}^{+}$ influenced by the refraction effect directly into the formula determining the temperature fluctuation. For simplicity, we shall consider here photon trajectories which do not enter the internal Friedman region, and, as usual in the model, we abandon deflection of light in the SdS spacetime. The impact angle $\psi_{\rm S}^{+}$ then has to be related to the view angle β of observer through the angle of refraction $\psi_{\rm F}^{+}$ (see Fig. 3.3).

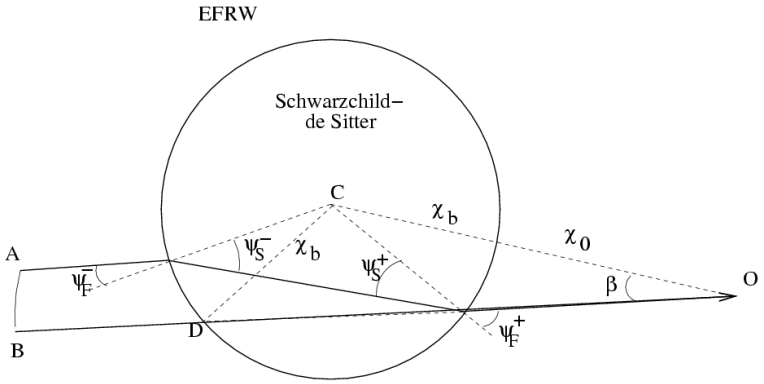

Figure 3.3: Refraction of a photon ray going through the vakuola. $\chi_{\rm b}$ is the comoving coordinate of the vakuola boundary, χ_0 is the comoving 'radial' distance of the observer from vakuola, $\chi = \chi_{\rm b} + \chi_0$. The ray BO, with no refraction effect considered in accord with [6], is included for comparison with previous results in order to clear up the relevance of the refraction on the Rees–Sciama effect.

The temperature fluctuation (frequency shift) of a CMBR photon due to

transversing the vakuola is given by the relation [6]

$$\Delta T = \frac{2H^3Y^3}{c^3}\left\{\frac{\Omega}{2}\sin^2\psi\cos\psi + \frac{1+2\Omega}{3}\cos^3\psi\right\}, \tag{3.19}$$

where $\psi = \psi_{\rm S}^+$ determines the length of the ray in the vakuola; $Y = R(\eta)\chi$ is the actual physical extension of the vakuola and $H = \dot{R}/R$ is the actual value of the Hubble parameter; $R(\eta)$ is the scale factor, $\dot{R} \equiv {\rm d}R/{\rm d}T$, η is the conformal time defined by $d\eta = dT/R$.

Refraction effect will change the length of light ray spanning the vakuola region (see Fig. 3.3). Of course, for vanishing refraction effect, there is $\psi_{\rm S}^+ = \psi_{\rm F}^+$ in agreement with [6]. Using formula (3.19) we find the temperature fluctuation with the refraction effect included to be given by the relation

$$\begin{aligned}\Delta T_r &= \frac{2H^3Y^3}{c^3}\left[\frac{\cos\psi_F^+ + V(r_{\rm b})}{1+V(r_{\rm b})\cos\psi_F^+}\right] \\ &\times \left\{\frac{\Omega}{2}\left[\frac{\sin\psi_F^+}{\gamma\left(1+V(r_{\rm b})\cos\psi_F^+\right)}\right]^2\right. \\ &+ \left.\frac{1+2\Omega}{3}\left[\frac{\cos\psi_F^+ + V(r_{\rm b})}{1+V(r_{\rm b})\cos\psi_F^+}\right]^2\right\}. \end{aligned} \tag{3.20}$$

The relevance of the refraction effect is given by the difference of the temperature fluctuations ΔT_r and ΔT:

$$\begin{aligned}\Delta \equiv \Delta T_r - \Delta T &= \frac{2H^3Y^3}{c^3}\left\{\frac{\Omega}{2}\left[\frac{\cos\psi_{\rm F}^+ + V_r}{1+V_r\cos\psi_{\rm F}^+}\left(\frac{\sin\psi_{\rm F}^+}{\gamma[1+V_r\cos\psi_{\rm F}^+]}\right)^2\right]\right. \\ &- \frac{\Omega}{2}\cos\psi_{\rm F}^+\sin^2\psi_{\rm F}^+ \\ &+ \left.\frac{1+2\Omega}{3}\left[\left(\frac{\cos\psi_{\rm F}^+ + V_r}{1+V_r\cos\psi_{\rm F}^+}\right)^3 - \cos^3\psi_{\rm F}^+\right]\right\}. \end{aligned} \tag{3.21}$$

In the limit of non-relativistic velocities, $V_r \ll 1$, the relations (3.11) imply

$$\cos\psi_{\rm S}^+ \sim \cos\psi_{\rm F}^+ + V_r\sin^2\psi_{\rm F}^+, \qquad \sin\psi_{\rm S}^+ \sim \sin\psi_{\rm F}^+(1 - V_r\cos\psi_{\rm F}^+), \tag{3.22}$$

so that up to the first order of V_r, the temperature difference is given by the formula

$$\Delta \equiv \Delta T_r - \Delta T \sim \frac{2H^3Y^3}{c^3}V_r\cos^2\psi_{\rm F}^+\sin^2\psi_{\rm F}^+\left(1+\Omega+\frac{\Omega}{2}\tan^2\psi_{\rm F}^+\right). \tag{3.23}$$

Clearly, as we expected intuitively, the influence of the refraction effect vanishes linearly with $V_r \to 0$.

The relevance of the refraction effect in terms of the viewing angle β follows directly from the sine rule (see Fig. 3.3)

$$\sin\psi_{\rm F}^{+} = \frac{\chi_0 + \chi_{\rm b}}{\chi_{\rm b}} \sin\beta \tag{3.24}$$

and from the relation between the Schwarzschild coordinate $r_{\rm b}$, and the Robertson–Walker comoving coordinate $\chi_{\rm b}$ given by

$$r_{\rm b} = R(t_{\rm b})\chi_{\rm b} = \frac{R_0}{1+z}\chi_{\rm b}, \tag{3.25}$$

where R_0 is recent value of R, and z is the cosmological redshift, being the measure of the cosmic time. Introducing new variables

$$A(\beta) = \frac{\sqrt{1-\left(\frac{\chi_0+\chi_{\rm b}}{\chi_{\rm b}}\sin\beta\right)^2} + V_r}{1 + V_r\sqrt{1-\left(\frac{\chi_0+\chi_{\rm b}}{\chi_{\rm b}}\sin\beta\right)^2}}, \tag{3.26}$$

$$B(\beta) = \frac{\frac{\chi_0+\chi_{\rm b}}{\chi_{\rm b}}\sin\beta}{\gamma\left[1 + V_r\sqrt{1-\left(\frac{\chi_0+\chi_{\rm b}}{\chi_{\rm b}}\sin\beta\right)^2}\right]}, \tag{3.27}$$

$$C(\beta) = \sqrt{1-\left(\frac{\chi_0+\chi_{\rm b}}{\chi_{\rm b}}\sin\beta\right)^2}\left(\frac{\chi_0+\chi_{\rm b}}{\chi_{\rm b}}\sin\beta\right), \tag{3.28}$$

the temperature difference (3.21) can be expressed as a function of β in the form

$$\Delta T_r - \Delta T = \frac{2H^3Y^3}{c^3}\left\{\frac{\Omega}{2}\left[A(\beta)B^2(\beta) - C(\beta)\right] + \frac{1+2\Omega}{3}\left[A^3(\beta) - \left(\sqrt{1-\left(\frac{\chi_0+\chi_{\rm b}}{\chi_{\rm b}}\sin\beta\right)^2}\right)^3\right]\right\} \tag{3.29}$$

The relevance of the refraction effect is illustrated by Fig. 3.4. By analysing the relation (3.29), we can show that for any value of β the influence of the refraction on the temperature fluctuations $\Delta T_r - \Delta T$ monotonically grows with V_r growing.

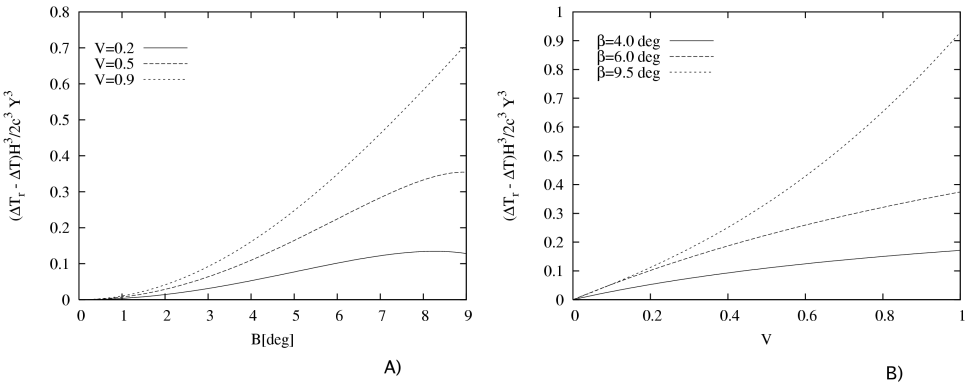

Figure 3.4: Plot A: Relevance of refraction is plotted as a function of angle β for three representative values of velocity $V = 0.2$, 0.5 and 0.9. Plot B: Relevance of refraction is plotted as a function of velocity V of MH for three representative values of angle $\beta = 4°, 6°$ and 9.5°. Both plots are drawn for $\Omega = 1$, $\chi_0 = 10$, $\chi_b = 2$ (see Fig 3.3).

3.3 The moment of leaving the vakuola

Assume that all photons coming from directions $0 \leq \beta \leq \beta_{max}(\sin\beta_{max} = k$, see Fig 3.5) are released at the same conformal time η_A and reach observer also at the same conformal time η_O. Here we neglect the time delay effects caused by passing through the SdS region. We also assume that the photons leaving vacuola under certain angle α, will reach its edge at conformal time η_D which is the same for both refracted and non-refracted trajectories(see Fig 3.5).

From the geometry of the configuration depicted on Fig.3.5 we have

$$\eta_D - \eta_A = (1 + \cos\alpha)\chi_b. \tag{3.30}$$

From definition of the conformal time, $\mathrm{d}\eta = c\mathrm{d}T/a = c\mathrm{d}a/(a\dot{a})$, one arrives to equation

$$(1 + \cos\alpha)\chi_b = c\int_{a_A}^{a_D} \frac{\mathrm{d}a}{a\dot{a}}. \tag{3.31}$$

The scale parameter a has units of length. $\dot{a}$ is defined by the Friedman equation

$$\dot{a}^2 \equiv \left(\frac{\mathrm{d}a}{\mathrm{d}T}\right)^2 = \frac{\Omega_{m0}H_0^2 a_0^3}{a} + \frac{\Lambda}{3}c^2a^2, \tag{3.32}$$

where a_0, Ω_{m0} and H_0 are today's values of scale parameter, density parameter of matter and Hubble parameter. We define dimensionless quantity x by

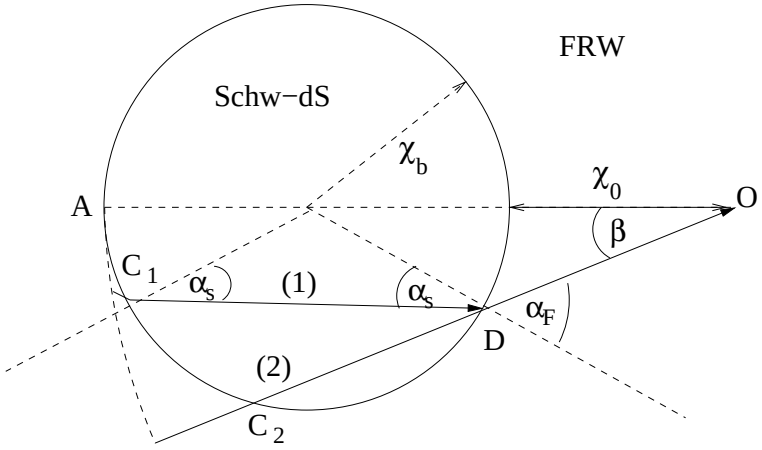

Figure 3.5: Schwarzchild-de Sitter vakuola of comoving radius χ_b immersed into Friedman-Robertson-Walker dust filled universe. Ray labeled (1) is refracted while ray labeled (2) is not. Both rays started from at conformal time η_A and arrive simultaneously to observer O at conformal time η_O. From the figure it is clear that under such assumptions they must also arrive simultaneously to D at conformal time η_D.

$$a = a_0 \cdot x. \tag{3.33}$$

The Fiedman equation and equation (3.31) then read

$$\dot{x}^2 = \Omega_{m0} H_0^2 / x + \frac{\Lambda}{3} c^2 x^2. \tag{3.34}$$

and

$$(1 + \cos\alpha)\chi_b = \frac{c}{a_0} \int_{x_A}^{x_D} \frac{\mathrm{d}x}{x\dot{x}} \;\Rightarrow\; (1 + \cos\alpha) r_{b0}/c = \int_{x_A}^{x_D} \frac{\mathrm{d}x}{x\dot{x}} \tag{3.35}$$

Inserting formula (3.34) into equation (3.35) one arrives to equation

$$(1 + \cos\alpha) r_{b0}/c = W \left[\mathrm{F}\left(cos^{-1}\frac{b}{t}, \frac{1}{1+b^2} \right) \right]_{t_A}^{t_D} \tag{3.36}$$

where

$$b = \sqrt{\frac{\sqrt{3}-3/2}{\sqrt{3}+3/2}}, \tag{3.37}$$

$$A = \Omega_{m0}H_0^2, \tag{3.38}$$

$$B = \Lambda c^2/3, \tag{3.39}$$

$$L = A/B, \tag{3.40}$$

$$t = \frac{x+(\sqrt{3}+1)^{-1}L^{1/3}}{(\sqrt{3}-1)^{-1}L^{1/3}-x}, \tag{3.41}$$

$$W = \sqrt{\frac{2}{(\sqrt{3}+3/2)(1+b^2)}}\frac{1}{A^{1/3}B^{1/6}} \tag{3.42}$$

For the input parameters x_A one can easily evaluate the value x_D of the dimensionless size of the vacuola when CMB photon leaves it. Defining the quantity

$$I = W\mathrm{F}\left(cos^{-1}\frac{b}{t_A}, \frac{1}{1+b^2}\right) \tag{3.43}$$

and the quantity $\tilde{I}$ by formula

$$\tilde{I} = (1+\cos\alpha)r_{b0}/c + I \tag{3.44}$$

the formula for the instant t_D when CMB photon leaves vakuola reads

$$t_D = \frac{b}{\mathrm{cn}[\tilde{I}/W, \frac{1}{1+b^2}]} \tag{3.45}$$

where cn is the Jacobi elliptic function. The quantity t_D is connected with x_D through equation (3.41). The quantity x is related to the redshift z by equality

$$x = \frac{1}{1+z}, \tag{3.46}$$

as folows from (3.33), the redshift, z_D, when the photon leaves the vakuola is then

$$z_D = \frac{1}{x_D} - 1. \tag{3.47}$$

3.4 WMAP Cosmological parameters applied on temperature fluctuations $\frac{\Delta T}{T}$

The cosmological parameters measured by WMAP experiment are used here to find out what scale are temperature fluctuations and how they depend on instant when CMB photon entered vakuola.

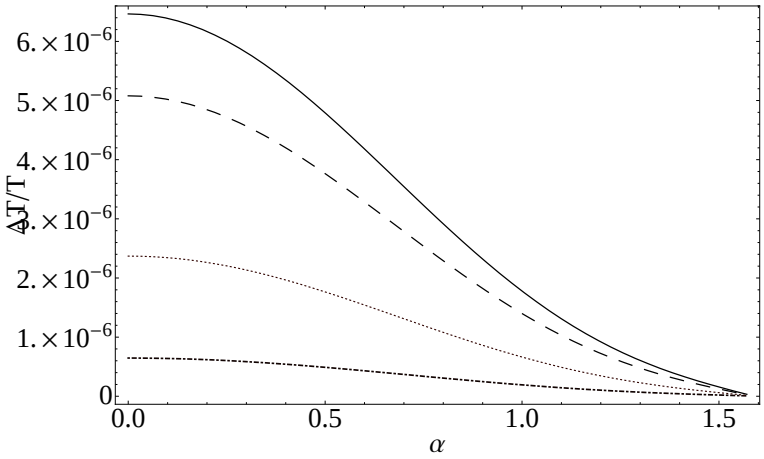

Figure 3.6: Temperature fluctuations of CMBR as a function of α for four different representative values of redshift z_A and the cosmological parameters $H_0 = 72km/s/Mpc$, $\Omega_{m0} = 0.27$, $\Lambda = 10^{-56}cm^{-2}$ and $r_{b0} = 500Mpc$. Curves: solid($z_A = 0.1$), dashed($z_A = 0.4$), dotted($z_A = 2$) and dotdashed($z_A = 10$).

From plots on figure Fig.3.6 one can see that the magnitude of temperature fluctuations caused by spherical inhomogenity of the Friedman universe are of the order 10^{-6}. With decreasing value of z_A the magnitude of the temperature fluctuations increases which is caused by the fact that physical dimensions of vakuola is bigger for smaller z_A than for higher ones.

3.5 Fourier components of temperature fluctuations profile

Here we concern on the first three componets of fourier decomposition of $\Delta T/T$. The formula for $\Delta T/T$ reads

$$\frac{\Delta T}{T} = \left(\frac{H(\eta_A)y(\eta_A)}{c}\right)^3 \frac{\cos\alpha + V(\eta_D)}{1 + V(\eta_D)\cos\alpha} \times$$

$$\left\{\frac{\Omega(\eta_A)}{2}\left(\frac{\sin\alpha}{1-V(\eta_D)\cos\alpha}\right)^2[1-V(\eta_D)^2]+ \frac{1+2\Omega(\eta_A)}{3}\left(\frac{\cos\alpha+V(\eta_D)}{1+V(\eta_D)\cos\alpha}\right)^2\right\} \tag{3.48}$$

To evaluate monopole, dipole and quadrupole anizotropies we must evaluate H, Ω, y and V in terms of redshift corresponding to conformal time η_A. From Friedman and continuity equations we arrive at

$$H^2(z) = \Omega_{m0}H_0^2(1+z)^3 + \frac{\Lambda}{3}c^2, \tag{3.49}$$

$$\Omega(z) = \frac{\Omega_{m0}H_0^2}{H^2(z)}(1+z)^3, \tag{3.50}$$

$$y(z) = a\cdot\chi_b = a_0\cdot\chi_b\cdot x = r_{b0}/(1+z), \tag{3.51}$$

$$V(z) = \sqrt{\frac{2GM}{c^2 r_{b0}}(1+z)+\frac{\Lambda r_{b0}^2}{3(1+z)^2}}. \tag{3.52}$$

We write the Fourier transformation in a following way. Setting $f(\alpha, z_A) \equiv \frac{\Delta T}{T}$ we write, for monopole, dipole and quadrupole moments, equations

$$f_0(k,z_A) = \frac{2k}{\pi}\int_0^{\pi/2} f(\alpha,z_A)\frac{\cos\alpha}{\sqrt{1-k^2\sin^2\alpha}}\mathrm{d}\alpha, \tag{3.53}$$

$$f_1(k,z_A) = \frac{2k}{\pi}\int_0^{\pi/2} f(\alpha,z_A)\cos\alpha\mathrm{d}\alpha, \tag{3.54}$$

$$f_2(k,z_A) = \frac{2k(1-2k^2)}{\pi}\int_0^{\pi/2} f(\alpha,z_A)\frac{\cos\alpha}{\sqrt{1-k^2\sin^2\alpha}}\mathrm{d}\alpha - \frac{4k^3}{\pi}\int_0^{\pi/2} f(\alpha,z_A)\frac{\cos^3\alpha}{\sqrt{1-k^2\sin^2\alpha}}\mathrm{d}\alpha, \tag{3.55}$$

where $k = \chi_b/(\chi_b = \chi_0)$ and z_A is redshift at the conformal time η_A. Because of the fact that $V = V(\alpha)$ (it follows from eqs (3.45), (3.47) and (3.41)), it is very difficult to obtain analytical expression or expression using elliptic integrals here. Therefore we decided to solve equations (3.53), (3.54) and (3.55) numerically and show on graphs the behaviour of monopole, dipole and quadrupole moments of temperature fluctuations (3.48).

Three graphs on Fig.3.8 show how the monopole, dipole and quadrupole terms depend on the redshift z, corresponding to the point A (see Fig.3.5)

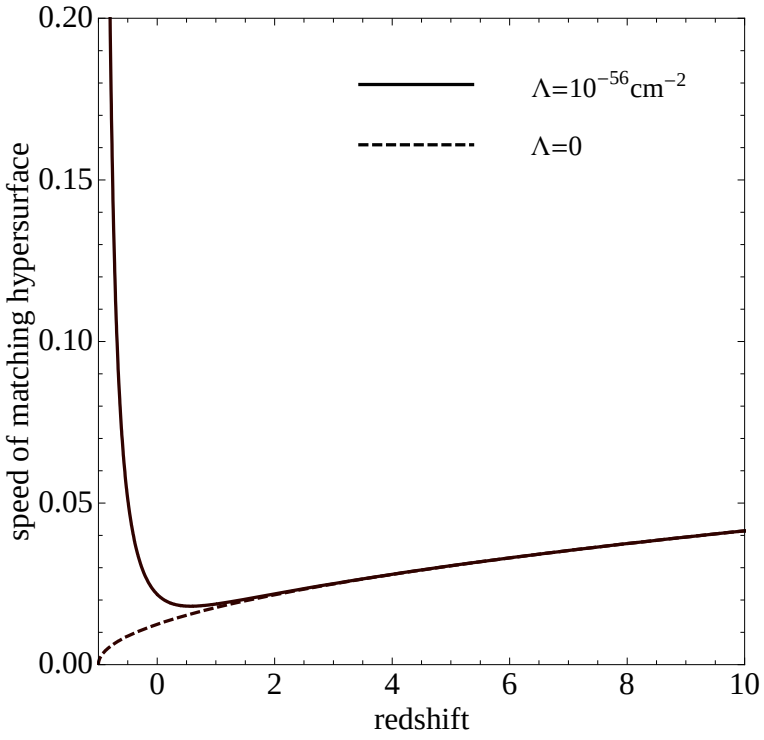

Figure 3.7: The speed of matching hypersurface relative to static SdS observers is plotted as a function of redshift parameter z for the cosmological parameters of our universe as measured by WMAP: $H_0 = 72km/s/Mpc$, $\Omega_m = 0.27$. The minimum is at $z \sim 0.5$ for the curve with $\Lambda = 10^{-56}cm^{-2}$. From this instant the universe is in the regime of accelerated expansion.

and on the fourth graph the speed parameter of vakuola as a function of redshift z corresponding to the point D (see Fig.3.5). Monopole, dipole and quadrupole moments behave in the same manner. They decrease on interval $z \in [z_{M_{min}}, \infty]$ and increase after crossing $z = z_{M_{min}}$, where M refers to monopole, dipole and quadrupole moments. Note that $z_{M_{min}}$ is different for different parameters k and it also depends on the moment itself. It is because of the fact that when gathering photons coming from different directions, each of them leave vakuola at diffent conformal time η_D. Some photons leave vakuola before the cosmological constant Λ dominates the universe and other, in the period when cosmological constant Λ dominates the universe.

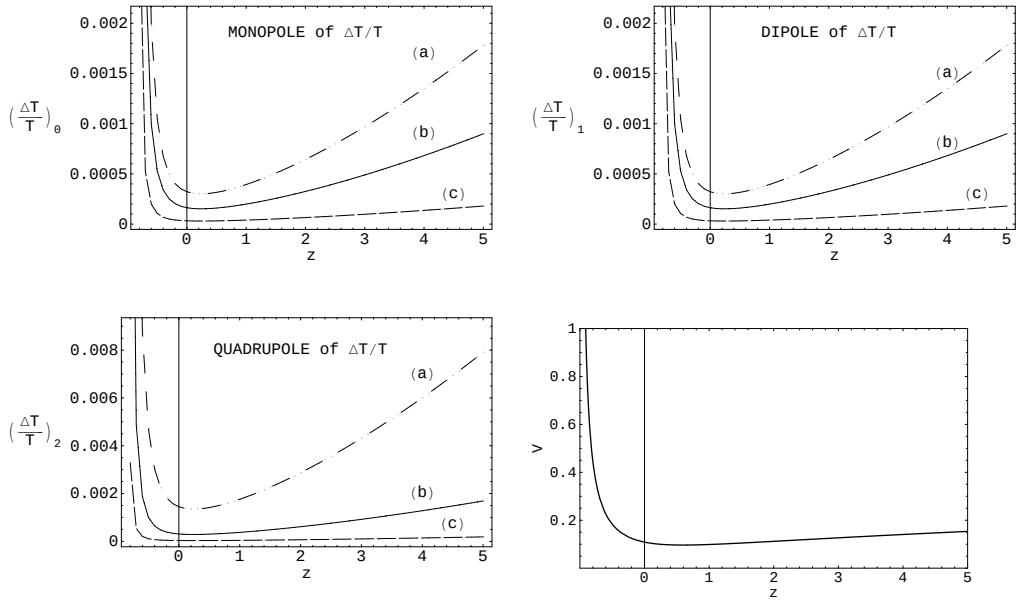

Figure 3.8: Monopole, dipole and quadrupole moments of fourier expansion of temperature fluctuations $\Delta T/T$ as a function of redshift z, are plotted here for three representative parameters k; curve (a) for $k = 0.99$, curve (b) for $k = 0.5$ and curve (c) for $k = 0.1$. The speed parameter V as a function of redshift z is plotted on the forth graph. The cosmological parameters are set to $H_0 = 72km/s/mpc$, $\Omega_{m0} = 0.27$, $\Lambda = 10^{-56}cm^{-2}$, $r_{b0} = 500Mpc$ and $c = 3 \times 10^6 km/s$.

Concluding remarks

Studying the fluctuations of CMBR in the accelerating universe with the repulsive cosmological constant, we have shown, how the influence of the refraction effect grows with the velocity of the MH, contrary to the standard Friedman models with $\Lambda = 0$, where the velocity of the MH falls in the expanding universe and the refraction effects are suppressed. In the accelerated universe, the velocity grows after MH crosses the static radius of the SdS spacetime, and the refraction effect becomes significant. Such effect could serve as another test of the presence of the cosmological constant; it could have strong observational consequences in future, when the velocity of the MH becomes to be relativistic. We conclude that there are two basic phenomena related to the importance of the refraction effect in the ESdS model explaining the temperature fluctuations of CMBR.

1. The total reflection phenomenon implies that some part of the vakuola region will not be visible to the external observer. This part will be enlarged with expansion velocity V_r growing.

2. The refraction effect on the temperature fluctuations (in the case of spatially flat universe) will fall, if the boundary of the MH $r_{\rm b}$ approaches the static radius $r_{\rm s}$ of the Schwarzschild-de Sitter region, and it starts to grow after crossing the static radius.The effect becomes to be extremely strong when $r_{\rm b}$ approaches the cosmological horizon $r_{\rm c}$ and $V_r \to 1$.

We can expect that in the accelerated universe the influence of the relict vacuum energy on the fluctuations of CMBR due to the Rees–Sciama effect could be very important, especially the refraction effect has the tendency to rise up the fluctuations. At present,we make our model more precise, and we estimate conditions under which currently observable effects could be expected.

Bibliography

[1] D. N. Spergel, L. Verde, H. V. Peiris, E. Komatsu, M. R. Nolta, C. L. Bennett, M. Halpern, G. Hinshaw, N. Jarosik, A. Kogut, M. Limon, S. S. Meyer, L. Page, G. S. Tucker, J. L. Weiland, E. Wollack, and E. L. Wright. *First Year Wilkinson Microwave Anisotropy Probe(WMAP) Observations: Determination of Cosmological Parameters.* Astrophys. J. Supp. Series, 2003, 148, Issue 1,pp. 175–194

[2] R. K. Sachs and A. M. Wolfe. Astrophys. J., 1967, 147:73

[3] G. Börner. *The Early Universe.* Springer-Verlag, Berlin-Heidelberg-New York,1993

[4] M. J. Rees and D. W. Sciama. Nature, 1968, 217:511

[5] A. Meszaros. *On the anisotropy of the cosmic microwave background* Astrophys. J, 423, 1994

[6] A. Mészáros and Z. Molnár. *On the alternative origin of the dipole anizotropy of microwave background due to the Rees–Sciama effect.* Astrophys.J., 1996, 470:49

[7] A. D. Linde. *Particle Physics and Inflationary Cosmology.* Gordon and Breach, New York, 1990

[8] Z. Stuchlík. *The motion of test particles in black-hole backgrounds with non-zero cosmological constant.* Bul. Astronom. Inst. Czechoslovakia, 1983, 34(3):129–149.

[9] Z. Stuchlík. *An Einstein–Strauss–de Sitter model of the universe.* Bul. Astronom. Inst. Czechoslovakia, 1984, 35(4):205–215.

[10] Z. Stuchlík. *The role of a repulsive cosmological constant in astrophysical processes.* Gravitation: Following the Prague Inspiration, Prague 2002

[11] Z. Stuchlik. *Influence of the relict cosmological constant on accretion discs.* Modern Physics Lett. A, 20, 2005

[12] Z. Stuchlík and S. Hledík. *Some properties of the Schwarzchild–de Sitter and Schwarzchild–anti-de Sitter spacetimes.* Phys. Rev. D, 1999, 60(4):044006(15 pages).

[13] Z. Stuchlík and S. Hledík. *Equatorial photon motion in the Kerr-Newman spacetimes with a non-zero cosmological constant*, Class. and Quant. Grav., 17, 2000. arXiv:0803.2539

[14] C. C. Dyer and R. C. Roeder. Astrophys. J., 1973, 180:L31

[15] Z. Stuchlík and J. Schee. Proceedings of RAGtime 4/5:Workshops on black holes and neutron stars, 14–16/13–15 October 2002/2003, Opava, Czech Republic, 2004, p.p. 187–203

[16] M. Sereno. *Role of* Λ *in the Cosmological Lens Equation.* Phys. Rev. Lett., 102, 2009. arXiv:0807.5123

[17] A. N. Aliev and A. E. Gümrükçüoğlu. *Charged rotating black holes on a 3-brane.* Phys. Rev. D, 71(10):104027–+, 2005.

[18] N. Arkani-Hamed, S. Dimopoulos, and G. Dvali. *The hierarchy problem and new dimensions at a millimeter.* Phys. Lett. B, 429:263–272, 1998.

[19] B. Aschenbach. *Measuring mass and angular momentum of black holes with high-frequency quasi-periodic oscillations.* Astronom. and Astrophys., 425:1075–1082, 2004.

[20] B. Aschenbach. *Measurement of mass and spin of black holes with qpos.* arXiv:0710.3454, 2007.

[21] G. Bao and Z. Stuchlík. *Accretion disk self-eclipse:x-ray light curve and emmision line.* Astrophys. J., 400:163–169, 1992.

[22] J. M. Bardeen. *Timelike and null geodesics in the kerr metric.* In Black holes (Les astres occlus), p. 215 - 239, pages 215–239, 1973.

[23] J. M. Bardeen, W. H. Press, and S. A. Teukolsky. *Rotating black holes: Locally nonrotating frames, energy extraction, and scalar synchrotron radiation.* Astrophys. J., 178:347–370, December 1972.

[24] J. Bičák and Z. Stuchlík. *On the latitudinal and radial motion in the field of a rotating black hole.* Bull. Astron. Inst. Czechosl., 27(3), 1976.

[25] A. Chamblin, H. S. Reall, H. Shinkai, and T. Shiromizu. *Charged brane-world black holes.* Phys. Rev. D, 63(6):064015, 2001.

[26] C. T. Cunningham and J. M. Bardeen. *The optical appearance of a star orbiting an extreme kerr black hole.* Astrophys. J., 183:237–264, 1973.

[27] B. Czerny, M. Mościbrodska, D.Proga, T. K. Das and A. Siemiginowska. *Low angular momentum accretion flow model of Sgr A* activity.* In Proceedings of RAGtime 8/9: Workshops on black holes and neutron stars, Opava, 15–19/19–21 September 2006/2007,p.35–44, 2007.

[28] N. Dadhich, R. Maartens, P. Papadopoulos, and V. Rezania. *Black holes on the brane.* Phys. Lett. B, 487:1, 2000.

[29] F. de Felice and M. Calvani. *Orbital and vortical motion in the Kerr metric.* Nuovo Cimento B Serie, 10:447–458, 1972.

[30] M. Dovčiak, V. Karas, G. Matt, and A. Martocchia. *Polarization of radiation from AGN accretion discs - the lamp-post model.* In S. Hledík and Z. Stuchlík, editors, *RAGtime 6/7: Workshops on black holes and neutron stars*, pages 47–54, December 2005.

[31] R. Emparan, M. Masip, and R. Rattazzi. *Cosmic rays as probes of large extra dimensions and TeV gravity.* Phys. Rev. D, 65(6):064023–+, March 2002.

[32] A. C. Fabian, M. J. Rees, L. Stella, and N. E. White. *X-ray fluorescence from the inner disc in Cygnus X-1.* MNRAS, 238:729–736, May 1989.

[33] C. Fanton, M. Calvani, F. de Felice, and A. Čadež. *Detecting accretion disks in active galactic nuclei.* Publ. Astron. Soc. Japan, (49):159–169, 1997.

[34] C. Germani and R. Maartens. *Stars in the braneworld.* Phys. Rev. D, 64:124010, 2001.

[35] A. M. Ghez. *Stellar orbits and the supermassive black hole at the center of our galaxy.* Am. Astro. Soc., 37:531, 2005.

[36] A. M. Ghez, S. Salim, N. N. Weinberg, J. R. Lu, T. Do, J. K. Dunn, K. Matthews, M. Morris, S. Yelda, E. E. Becklin, T. Kremenek, M. Miloslavljevic, and J. Naiman. *Probing the properties of the Milky Way's central supermassive black hole with stellar orbits.* IAU Symposium,248, p.52–58, 2008. arXiv:astro-ph 0808.2870

[37] V. Karas, D. Vokrouhlicky, and A. G. Polnarev. *In the vicinity of a rotating black hole - a fast numerical code for computing observational effects.* MNRAS, 259:569–575, December 1992.

[38] R. P. Kerr. *Gravitational field of a spinning mass as an example of algebraically special metrics.* Phys. Rev. Lett., (11):26, 1963.

[39] G. V. Kraniotis. *Frame dragging and bending of light in kerr and kerr (anti) de sitter spacetimes.* Class. and Quant. Grav., 22:4391–4424, 2005.

[40] G. V. Kraniotis. *Periapsis and gravitomagnetic precessions of stellar orbits in kerr and kerr-de sitter black hole spacetimes.* Class. and Quant. Grav., 24:1775–1808, 2007.

[41] A. Laor. *Line profiles from a disk around a rotating black hole.* Astrophys. J., 376:90–94, 1991.

[42] R. Maartens. *Brane-world gravity.* Living Rev. Rel., 7:7, 2004.

[43] G. Matt, A. C. Fabian, and R. R. Ross. *Iron k-alpha lines from x-ray photoionized accretion discs.* MNRAS, 262:179–186, May 1993.

[44] J. E. McClintock, R. Narayan, and R. Shafee. *Estimating the spins of stellar-mass black holes.* arXiv:0707.4492, 2007. To appear in Black Holes, eds. M. Livio and A. Koekemoer (Cambridge University Press), in press (2008).

[45] C. W. Misner, K. S. Thorne, and J. A. Wheeler. *Gravitation.* W. H. Freeman and company, San Francisco, 1973.

[46] R. Narayan, J. E. McClintock, and R. Shafee. *Estimating the spins of stellar-mass black holes by fitting their continuum spectra.* arXiv:0710.4073, October 2007.

[47] L. Randall and R. Sundrum. *An alternative to compactification.* Phys. Rev. Lett., 83(23):4690–4693, 1999.

[48] K. P. Rauch and R. D. Blandford. *Optical caustics in a kerr spacetime and the origin of rapid x-ray variability in active galactic nuclei.* Astrophys. J., (421):46–68, 1994.

[49] M. J. Reid. *Is there a supermassive black hole at the center of the Milky Way?* arXiv:0808.2624, 2008

[50] R. A. Remillard and J. E. McClintock. *X-ray properties of black-hole binaries.* Ann. Rev. of Astron. and Astrophys., 44(1):49–92, September 2006.

[51] J. Schee and Z. Stuchlík. *Spectral line profile in brany kerr spacetime.* In Proceedings of RAGtime 8/9: Workshops on black holes and neutron stars, Opava, 15–19/19–21 September 2006/2007,p.209–220, 2007.

[52] J. Schee, Z. Stuchlík, and J. Juráň. *Light escape cones and raytracing in kerr geometry.* In Proceedings of RAGtime 6/7: Workshops on black holes and neutron stars, Opava, 16–18/18–20 September 2004/2005, p.143–155, 2005.

[53] T. Shiromizu, K. Maeda, and M. Sasaki. *The einstein equations on the 3-brane world.* Phys. Rev. D, 62:024012, 2000.

[54] T. E. Strohmayer. *Raising the curtain on extreme stars.* Astronomy, 35:32–37, March 2007.

[55] Z. Stuchlík. *Null geodesics in the kerr-newman metric.* Bull. Astron. Inst. Czechosl., 32(6), 1981.

[56] Z. Stuchlík. *The radial motion of photons in kerr metric.* Bull. Astron. Inst. Czechosl., 32(1), 1981.

[57] Z. Stuchlík and G. Bao. *Radiation from hot spots orbiting an extreme Reissner-Nordstrm black hole.* General Rel. and Grav., 24(9), 1992.

[58] Z. Stuchlík, J. Bičák, and V. Balek. *The shell of incoherent charged matter falling onto a charged rotation black hole.* Class Quantum Grav., 31(53), 1999.

[59] Z. Stuchlík and S. Hledík. *Properties of the Reissner-Nordstrom spacetimes with a nonzero cosmological constant.* Acta. Phys. Slovaca, 52, 363, 2002.

[60] Z. Stuchlík and A. Kotrlová. *Orbital resonance model of qpos in braneworld kerr black hole spacetimes.* In Proceedings of RAGtime 8/9: Workshops on black holes and neutron stars, Opava, 15–19/19–21 September 2006/2007, p.323–362, 2007.

[61] G. Török. *A possible 3:2 orbital epicyclic resonance in QPO frequencies of Sgr A*.* Astron. and Astrophys., 1(440), 2005a.

[62] G. Török. *QPOs in microquasars and sgr a* measuring the black hole spin.* Astronom. Nachr., 856(326), 2005b.

[63] G. Török, M. Abramowicz, W. Kluźniak, and Z. Stuchlík. Astron. and Astrophys., 1(436), 2005.

[64] Y. C. Joshi. *Displacement of the Sun from the Galactic plane.* MNRAS, 378:768–776, June 2007. arXiv:astro-ph/0704.0950.

[65] A. F.Zakharov. *The iron K_α-line as a tool for analysis of black hole characteristics.* Publications of the Astronomical Observatory of Belgrade, 76, 147–162, 2003. arXiv: astro-ph/0411611.

[66] M. Sasaki, T. Shiromizu, and K.-I. Maeda. *Gravity, stability, and energy conservation on the Randall-Sundrum brane world.* Phys. Rev. D, 62(2):024008–+, July 2000.

[67] S. U. Viergutz. *Image generation in Kerr geometry. I. Analytical investigations on the stationary emitter-observer problem.* Astronomy and Astrophysics, 272:355–+, May 1993.

[68] A. F. Zakharov and S. V. Repin. Different types of fe k_α lines from radiating annuli near black holes. New Astr., 11:405–410, 2006.

[69] B. Czerny, M. Moscibrodzka, D. Proga, T. Das, and A. Siemiginowska. *Low angular momentum accretion flow model of Sgr A* activity.* ArXiv e-prints, 710, October 2007.

[70] R. A. Remillard. *X-ray spectral states and high-frequency qpos in black hole binaries.* Astro. Nach., 326(9), 2005.

[71] T. Strohmayer. *Understanding the nature of high inclination low mass X-ray binaries: broad-band and line spectra from A1744-361.* In Chandra Proposal, pages 2377–+, September 2007.

[72] A. M. Ghez, S. Salim, S. D. Hornstein, A. Tanner, J. R. Lu, M. Morris, E. E. Becklin, and G. Duchêne. *Stellar orbits around the galactic center black hole.* Astrophys. J., 620:744–757, 2005.

[73] J. Schee and Z. Stuchlík. *Optical effects in brany kerr spacetimes.* In Proceedings of RAGtime 8/9: Workshops on black holes and neutron stars, Opava, 15–19/19–21 September 2006/2007, 2007.

[74] Z. Stuchlík, P. Slaný and G. Török. *LNRF-velocity hump-induced oscillations of a Keplerian disc orbiting near-extreme Kerr black hole: a possible explanation of high-frequency QPOs in GRS 1915+105.* Astronomy and Astrophysics,470, 2007 arXiv:0704.1252

[75] Z. Stuchlík, P. Slaný and G. Török. *Humpy LNRF-velocity profiles in accretion discs orbiting almost extreme Kerr black holes. A possible relation to quasi-periodic oscillations.* Astronomy and Astrophysics,463, 2007

[76] Z. Stuchlík and K. Plšková. *Optical appearance of isotropically radiating sphere in the Schwarzschild-de Sitter spacetime.* RAGtime 4/5: Workshops on black holes and neutron stars, 2004, p.167–185

[77] K. S. Virbhadra and C. R. Keeton, *Time delay and magnification centroid due to gravitational lensing by black holes and naked singularities.* Phys. Rev. D, 77, 2008, arXiv:0710.2333

[78] P. Bakala, P. Čermák, S. Hledík, Z. Stuchlík and K. Truparová. *Extreme gravitational lensing in vicinity of Schwarzschild-de Sitter black holes.* Central European Journal of Physics, 5, 2007, p.599-610, arXiv:0709.4274